University of Zurich^UZH

Department of Geography

Morphologic changes and related processes of a disintegrating glacier tongue

GEO 511 Master's Thesis

Author
Oliver Hunziker
12-717-278

Supervised by
Prof. Dr. Andreas Vieli
Dr. Johann Müller

Faculty representative
Prof. Dr. Andreas Vieli

29.06.2018
Department of Geography, University of Zurich

Acknowledgement

This study would not have been feasible without the generous support of others. I am grateful to all of those with whom I have had the pleasure to work during this project.

I would like to express my sincere gratitude to my supervisors Andreas Vieli and Johann Müller for reliably supporting me throughout the learning and writing process with useful inputs and providing drone images and other existing data for me. A special thank goes to James Ferguson for his support with measurements and the acquisition of drone images during the field visit. I would like to thank Nico Mölg for letting me use his laptop for extended periods of time, without which the processing of the drone images would not have been possible. My sincere thank goes to Philip Joerg for introducing me to image processing software and allowing me to use his infrastructure.

A special thank goes to Shant Dakessian for his constant moral support and advice about workflow and time management. I particularly thank my brother, Philipp, for proofreading the entire thesis and loosening the atmosphere during its finalization. Finally, I would like to thank my parents, Franziska and Ulrich, for making my studies possible and for their ongoing generous support during all these years.

Summary

The effects of climate change on glaciers have been covered in numerous studies and continue to be a relevant topic in glaciological and geomorphological research. It is well known that most glaciers all over the globe have been retreating for years or decades, mostly due to rising air temperatures and changes in precipitation regimes. The speed and manner in which glacier tongues are disappearing, however, depend on more than just climatic factors. Glacial surface features occurring on rapidly retreating glacier tongues as well as their interactions with each other can render the tongues' disintegrations highly individual. The formation and development of individual features, such as ice cliffs and moraines, have been subject to plentiful studies, but there is a lack in literature concerning their combined impact on a glacier tongue's geometry and disintegration.

This study focuses on the disintegration of the Tiefenglacier's tongue in Uri, Switzerland, to investigate and quantify the effects of glacial features on its retreat. Data collected by students of the University of Zurich between July 2014 and July 2017 are analyzed and supplemented with additional measurements conducted in October 2017. Furthermore, orthophotos as well as digital surface models (DSMs) created using unmanned aerial vehicles (UAVs) and Structure from Motion (SfM) techniques are used to track the developments of selected glacial features and calculate vertical elevation differences in a GIS environment. The features studied include a lateral moraine, a medial moraine, a sediment hill, an ice cliff and two funnel-shaped depressions. Moreover, the effects of supraglacial debris as well as the ice flow velocity are examined in context with the tongue's evolution.

While some glacial features strongly accelerate the tongue's retreat, others preserve bodies of ice beneath thick layers of supraglacial debris, which causes a geometrically irregular disintegration. The ice cliff, for example, has experienced backwasting rates of up to 14.5 m/a, whereas the peak of the sediment hill, which recently appeared on the lower third of the tongue, shows no measurable changes in elevation. The observed differences in melt rates are mainly the result of both the insulating and melt enhancing properties of supraglacial debris, as well as the aspect and slope of the ice surface. Although the findings suggest that the glacier tongue is almost stagnant, ongoing en- and subglacial processes could be derived from non-intrusive measurements. Subglacial air-filled cavities and melt water streams destabilize the ice surface, leading to funnel-shaped depressions and collapses. Further, the formation of crevasse-fill ridges, a landform found in formerly glaciated areas, could be documented.

The combination of UAV-derived imagery and in-situ measurements presents a very economical way to analyze a glacier tongue's evolution over the span of multiple years. This study helps to understand the development of rapidly retreating glacier tongues in a warming climate and exemplifies methods to expand research in this area.

Zusammenfassung

Die Effekte vom Klimawandel auf Gletscher wurden bereits in zahlreichen Studien behandelt und bleiben ein relevantes Thema in der glaziologischen und geomorphologischen Forschung. Es ist allgemein bekannt, dass sich die meisten Gletscher weltweit seit Jahren oder Jahrzenten zurückziehen, hauptsächlich verursacht durch steigende Lufttemperaturen und veränderte Niederschlagsregimes. Die Geschwindigkeit und Art und Weise, in welcher Gletscherzungen verschwinden, hängen jedoch von mehr als nur klimatischen Faktoren ab. Glaziale Oberflächenformen, die auf schnell zurückziehenden Gletscherzungen vorzufinden sind, sowie deren Interaktionen miteinander, können den Zerfall der Zungen sehr individualisieren. Die Entstehung und Entwicklung von einzelnen Formen, wie zum Beispiel Eiskliffs und Moränen, wurden in vielen Studien untersucht, jedoch gibt es eine Lücke in der Literatur bezüglich deren kombinierten Einfluss auf die Geometrie und den Zerfall von Gletscherzungen.

Diese Studie legt den Fokus auf den Zerfall der Zunge des Tiefengletschers in Uri, Schweiz, um die Effekte besagter Oberflächenformen auf deren Rückzug zu untersuchen und quantifizieren. Datenmaterial, welches von Studenten der Universität Zürich zwischen Juli 2014 und Juli 2017 erhoben wurde, wird analysiert und ergänzt mit zusätzlichen Messungen von Oktober 2017. Des Weiteren werden Orthophotos sowie digitale Oberflächenmodelle, welche mittels unbemannten Luftfahrzeugen und Structure from Motion erstellt wurden, verwendet, um die Entwicklung ausgewählter glazialer Formen zu verfolgen und vertikale Höhenänderungen in einer GIS-Umgebung zu berechnen. Bei den untersuchten Formen handelt es sich um eine Seitenmoräne, eine Mittelmoräne, einen Schutthügel, ein Eiskliff sowie zwei trichterförmige Einsenkungen. Ausserdem werden die Auswirkungen des supraglazialen Schutts und die Fliessgeschwindigkeit des Eises im Zusammenhang mit der Entwicklung der Gletscherzunge untersucht.

Während manche glaziale Formen den Rückzug der Zunge stark beschleunigen, erhalten andere Formen Eiskörper unter dicken Schichten supraglazialen Schutts intakt, was einen geometrisch unregelmässigen Zerfall der Zunge zur Folge hat. Das Eiskliff weist beispielsweise Rückzugsraten von bis zu 14.5 m/a auf, während die Spitze des Schutthügels, welcher erst kürzlich auf dem unteren Drittel der Gletscherzunge entstanden ist, keine messbaren Höhenänderungen zeigt. Die beobachteten unterschiedlichen Schmelzraten sind hauptsächlich auf die sowohl isolierenden als auch schmelzsteigernden Eigenschaften des supraglazialen Schutts, und die Exposition und die Steigung der Eisoberfläche zurückzuführen. Obwohl die Ergebnisse darauf hindeuten, dass die Gletscherzunge beinahe stagniert, konnten fortlaufende en- und subglaziale Prozesse von den nicht intrusiven Messungen abgeleitet werden. Subglaziale, mit Luft gefüllte Hohlräume und Schmelzwasserströme destabilisieren die Eisoberfläche, was zu trichterförmigen Einsenkungen und Einstürzen führt. Zudem konnte die Entstehung von *crevasse-fill ridges*, eine Oberflächenform vorkommend in ehemals vergletscherten Gebieten, dokumentiert werden.

Die Kombination von Drohnenaufnahmen und vor Ort durchgeführten Messungen stellt eine sehr kostengünstige Weise dar, die Evolution einer Gletscherzunge über mehrere Jahre zu analysieren. Diese Studie unterstützt das Verständnis der Entwicklung schnell zurückziehender Gletscherzungen in einem sich erwärmenden Klima und veranschaulicht Methoden, um Forschung in diesem Gebiet zu vertiefen.

Content

Figures

Tables

Abbreviations

Abbreviation	Meaning
AGNES	Automated GNSS Network for Switzerland
AME	Absolute Mean Error
DEM	Digital Elevation Model
dGPS	Differential Global Positioning System
DSM	Digital Surface Model
DTM	Digital Terrain Model
GCP	Ground Control Point
GIS	Geographic Information System
GNSS	Global Navigation Satellite System
GPR	Ground Penetrating Radar
GSD	Ground Sampling Distance
MED	Mean Elevation Difference
$\mathbf{R^2}$	Coefficient of determination
SE	Standard Error
SfM	Structure from Motion
STD	Standard Error
swisstopo	Swiss Federal Office of Topography
UAV	Unmanned Aerial Vehicle

1. Introduction

1.1. Motivation

It is well known that most glaciers in the world exhibit a retreating trend (WGMS). The most important factor responsible for this behavior is ongoing climate change, more specifically rising air temperatures as well as changes in precipitation since the industrial revolution (Barry 2006, Oerlemans et al. 2009). The great variety of glaciers existing worldwide due to environmental factors such as climate and topography means that their behaviors to a warming climate can differ significantly from one another. Even on a more local scale, the retreat of glaciers has been observed to vary. In the Swiss Alps, for example, glaciers have experienced an immense downwasting in the last few decades with “highly individual and non-uniform changes in glacier geometry”, rather than a dynamic glacier response to the changing climate (Paul et al. 2004). These individual changes include the occurrence of glacial features on their tongues, such as ice cliffs, moraines or subglacial cavities. Their dynamics and melt regimes differ from intact glacier tongues and can lead to their accelerated disintegration. Supraglacial debris plays an important role in the formation of such features as it can have both insulating or melt enhancing properties (Nakawo & Rana 1999, Nicholson & Benn 2013). Thompson et al. (2016) emphasize that it is difficult to make predictions about the dynamics of debris-covered, stagnating glaciers due to their complex forms. The analysis of glacial features’ dynamics as well as their impact on a glacier tongue’s development is therefore crucial for the understanding of the behavior of rapidly retreating glaciers.

This study aims to examine the underlying causes leading to the formation of such glacial features as well as their influence on a disintegrating glacier tongue. To this end, the Tiefenglacier in the canton of Uri, Switzerland, was chosen, as it showed a rapid retreat over the last decade, coupled with the formation of a number of glacial features (Fig. 1). Further, a variety of measurements conducted on its

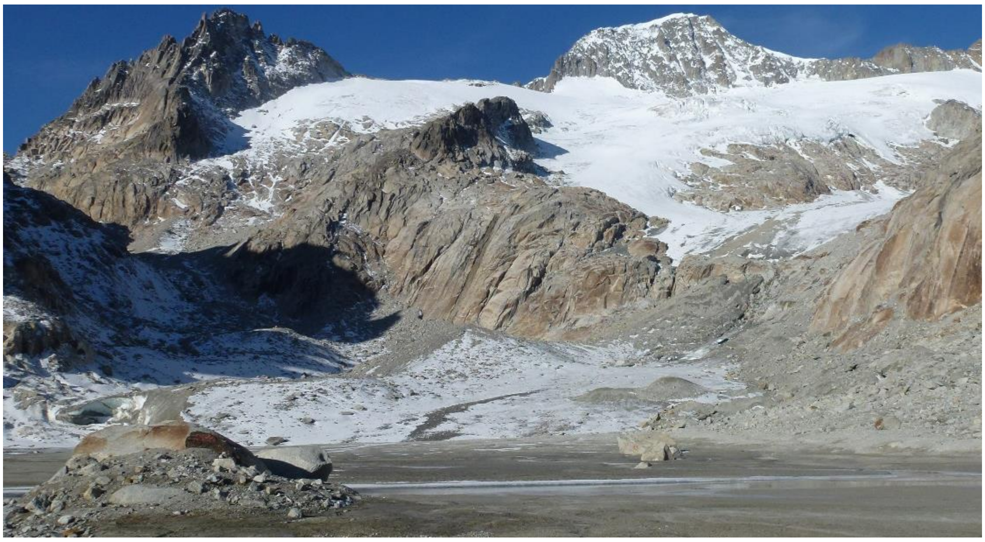

Fig. 1: The Tiefenglacier’s tongue as seen from the glacier forefield. In the background the Gross Bielenhorn and the Galenstock are visible.

tongue as well as images captured with an unmanned aerial vehicle (UAV) have been available since July 2014, which are used for the analysis of the tongue's dynamics.

In recent years, glacial processes have been increasingly studied using UAV derived Structure from Motion (SfM) photogrammetry, as it offers several advantages compared to glacial monitoring with satellite remote sensing. For example, the cost of producing a high-resolution image using satellite sensors (e.g. GeoEye) is far greater than using a UAV (Bhardwaj et al. 2016). UAVs further allow the user to acquire images on selected dates and at specific times, whereas data acquisition using space-borne platforms depends on their temporal resolution (Bhardwaj et al. 2016).

Dąbski et al. (2017) show that UAV-based photography in combination with GIS data processing is a suitable way to map and analyze periglacial landforms on King George Island in Antarctica. In combination with ground and satellite observations, UAV data has further been used for the analysis of the effects of mineral dust on snow covers, which has a significant impact on glacier retreat (Di Mauro et al. 2015). Moreover, SfM photogrammetry has already been used for the mapping and quantification of ice-cored moraine degradation on a glacier in Svalbard as well as the mapping of glacial surface features on a small Alpine glacier (Fugazza et al. 2015, Tonkin et al. 2016). However, in the literature there appears to be a lack of the temporal analysis and quantification of individual glacial surface features as they occur on rapidly retreating glacier tongues and their impact on the overall dynamics of the tongue. Glacial features can affect a shrinking glacier tongue in a way that its behavior differs substantially from the expected development without the presence of such features. It is therefore necessary to study the influence of glacial features on retreating glacier tongues to understand their behavior in a warming climate.

1.2. Objectives & research questions

The focus of this study lies on the formation and development of glacial features on a disintegrating glacier tongue and their influence on its dynamics and geometric shape between July 2014 and October 2017. Further, the evolution of said features as well as the flow velocity of the tongue are quantified and discussed in context of supraglacial debris cover. More specifically, the aim is to answer the following research questions:

1. What kinds of glacial features can be found on the glacier tongue?
2. What are the underlying processes leading to the observed glacial features?
3. In what way do the glacial features influence the development and geometric shape of the glacier tongue?
4. How do the glacial features develop in quantitative terms?

The existing data stems from field reports written by students of the University of Zurich, who conducted their own measurements on the Tiefenglacier's tongue and its surroundings in the summers between 2014 and 2017. Additionally, a field visit in October 2017 was undertaken for the investigation of the current state of the tongue as well as debris thickness measurements. Further, digital surface models (DSMs) and orthophotos of the glacier tongue generated using SfM present an essential role for the analysis of its dynamic development in a GIS environment.

The following approaches were chosen to answer the research questions:

- The surface of the glacier tongue is mapped using orthophotos and images taken on site;
- Multitemporal surface elevation changes are calculated and visualized by means of difference imaging, profile graphs and point-based elevation differences;
- Surface ablation measured with permanently installed ablation stakes is compared to surface elevation changes to study the presence of dynamic replacement;
- A more detailed distribution of supraglacial debris is mapped and its effect on surface ice ablation is examined using debris thickness and ablation stake measurements;
- Feature tracking of supraglacial rocks is used to calculate the flow velocity of the glacier tongue's ice.

2. Background

In the following chapter, the basic dynamics of glacier movement in the context of a warming climate as a theoretical background is presented. Further, the study area is introduced, including details concerning the characterization of the Tiefenglacier as well as temperature records of nearby meteo stations.

2.1. Glaciers in a warming climate

Glaciers are natural phenomena with very dynamic natures whose behaviors strongly depend on the surrounding climate. Ongoing climate change therefore directly affects their developments in various ways. In the following, the general mechanics of glacial movement as well as their behaviors in a changing climate are presented. The understanding of basic glacial dynamics is necessary to put the stagnation of the Tiefenglacier's tongue into a larger context.

2.1.1. Glacier movement

Glaciers are defined as bodies of ice which are in a continuous downhill motion. Apart from the underlying and surrounding topography, the flow velocity of the ice depends on its flow mechanisms. In intact glaciers, the ice flows from the accumulation area into the ablation area through three different types of motion: Internal deformation, basal sliding, and sliding on a deforming glacier bed (Knight 1999).

Internal deformation of the ice, or creep, is the result of the gravitational driving stress on the ice and occurs to different degrees in all bodies of ice. The ice crystals start changing their shape under the pressure which allows the ice to slowly flow towards the lowest point, similar to a metal near its melting point (Benn & Evans 2010). The thicker the overlying body of ice is, the more gravitational stress acts on the crystals, and the faster the flowing motion takes place. Similarly, higher ice temperatures promote higher flow velocities, as the ice becomes more susceptible to plastic deformation the warmer it is. Further, the flow velocity through internal deformation depends on the location within the glacier. The highest velocities are typically found on the glacier surface at the farthest distance from the margins, because the glacier bed and the surrounding rock walls slow down the ice flow through resistive stresses (Jiskoot 2011).

Basal sliding is observed exclusively on glaciers with a layer of water acting as a lubricant between their base and the glacier bed (Knight 1999). Meltwater flowing to the glacier bed reduces the friction between the ice and the bed, allowing it to slide over it. While the flow velocity through internal deformation is rather small, basal sliding can account for up to 90% of the total movement of glaciers with water at their bases (ALPECOLe 2011).

If the glacier bed consists of poorly consolidated sedimentary rocks or other soft material, it can deform under the glacier's driving stress and accelerate its flow downslope (Benn & Evans 2010). This process is more efficient when the underlying sediment is saturated with melt water, which reduces its strength and thus makes it more deformable (Knight 1999).

2.1.2. Stagnating glaciers

As described above, numerous environmental factors control a glacier's movement, such as the topography, the thermal regime as well as the composition and consistency of the bed material. To understand why the Tiefenglacier's flow velocity has been decreasing significantly over the last decades, the glacier's mass balance needs to be taken into account.

The glacier mass balance is a concept that describes the difference between the gain and loss of ice mass in a specified time period (Benn & Evans 2010). Mass gain happens in the upper part of the glacier, the accumulation zone, where snow gets compressed under its own weight first to firn and then to ice. Snow accumulation occurs in different ways: through snowfall, avalanches, re-freezing of meltwater or freezing of water vapor on the ice surface (Knight 1999). In the ablation zone, the glacier loses ice mass through melting, sublimation and, if the tip is submerged in water, calving. The replacement of this ice by the flowing motion of the glacier is called dynamic replacement and only exists on moving glaciers. While accumulation is mostly measured during the months of winter and ablation during summer, the mass balance usually refers to the *balance year*, which starts and ends when the glacier mass has reached its minimum at the end of the ablation season (Benn & Evans 2010). Advancing glaciers have a positive mass balance and gain more mass in a year than they lose and vice versa. A glacier with a mass balance of zero thus experiences the same amount of accumulation and ablation within a year and does not experience a change of mass; it is in *equilibrium*.

The glacier mass balance directly responds to the atmospheric conditions without any temporal delay (Zemp et al. 2009). The solid precipitation throughout the year acts as the main factor contributing to accumulation, whereas the mean annual air temperature has the biggest effect on the ablation. Therefore, global rising air temperatures due to climate change lead to increased ablation and longer melting periods during summer and thus affect the glaciers' behaviors. However, the reaction of glaciers to changing climatic conditions shows a temporal lag, called glacier response time. Its duration depends on several factors, such as the glacier's mass balance gradient (the change of accumulation and ablation with elevation), its mean thickness, the ablation rate at its terminus, as well as its hypsometry (mass balance distribution relative to elevation) (Benn & Evans 2010, Jóhannesson et al. 1989, Kirkbride & Winkler 2012). If a glacier's mass balance stays negative over a certain time period, the consequences can therefore be observed for much longer in the form of volumetric mass loss and the recession of its snout.

If the accumulation on a glacier does not cancel out the ablation caused by rising air temperatures, the glacier will slow down and eventually cease to move. The reason for this is the reduced amount of driving stress acting on the ice, since not enough ice flows into the ablation zone to maintain the flow velocity. Downwasting, or thinning, which describes the loss of ice thickness, results from reduced amounts of ice coming from the accumulation area coupled with high ablation rates. This process reduces the gradient of the ice surface in the ablation zone. A lower gradient will further lead to lower flow velocities because of the reduced driving stress, which starts a positive feedback between stagnation and downwasting (Benn et al. 2012).

2.2. Study area

2.2.1. Localization Tiefenglacier

The Tiefenglacier is located in the Urserental and is part of the municipality Realp in the canton of Uri, Switzerland (Fig. 2). To its West lies the Galenstock, behind which the well-known Rhoneglacier can be found in the canton of Wallis. The Tiefenstock and the Dammazwillinge form the northern boundary of the Tiefenglacier, whereas the Gletschhorn encloses it in the Northeast. To the East of the glacier, there is a U-shaped valley formed by the Tiefenglacier when it had a considerably larger extent than today. The valley is characterized by the Tiefenbach, a stream fed mostly by the Tiefenglacier's melt water, which joins the Furkareuss further downstream in the Urserental. On an elevation to the East of the Tiefenbach, there is a hut offering accommodation for tourists, called Albert-Heim-Hut. It is part of the Swiss Alpine Club SAC and was used by the students of the course GEO 411 from the University of Zurich. Both the Tiefenglacier and the Albert-Heim-Hut can be reached on foot from the restaurant Tiefenbach, located on the Furkastrasse.

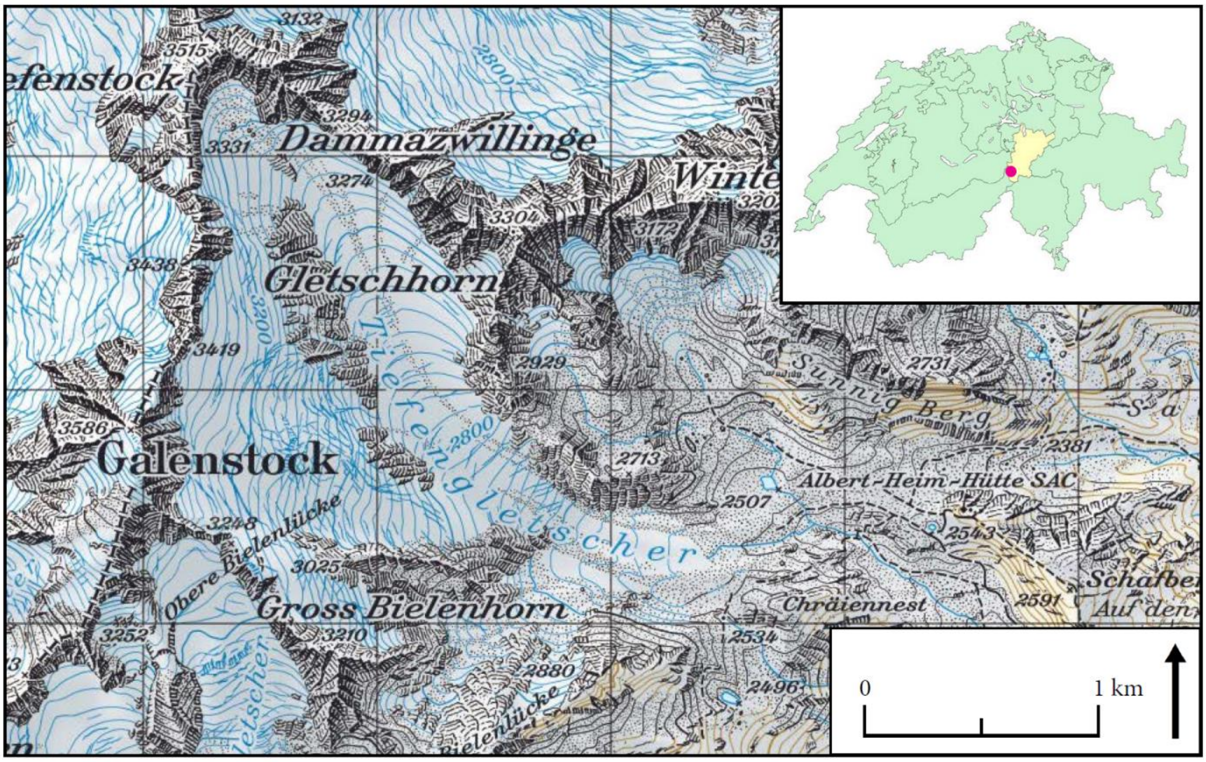

Fig. 2: Location of the Tiefenglacier in Switzerland and the canton of Uri. (Background: swisstopo National Map 1:50´000 from 2013).

2.2.2. Characterization Tiefenglacier

As of October 2017, the Tiefenglacier‘s terminus is located at an elevation of about 2505 m a.s.l., whereas its accumulation area reaches up to around 3320 m a.s.l. The direction of the glacier’s flow changes from south-southeast near the Tiefenstock and the Dammazwillinge to east at its terminus. The southern part of the accumulation area, near the Galenstock, flows towards the east as well. According to the Swiss Glacier Monitoring Network, the glacier had a length of 2.46 km in 2016 (Schweizerisches Gletschermessnetz).

The Tiefenglacier is classified as a temperate glacier, meaning its ice is throughout at its melting temperature and therefore contains liquid water (Fountain 2011). It is believed to be stagnant or almost stagnant because of the increased mass loss in recent years and no significant flowing motion has been visible. Its tongue is characterized by two prominent moraines; a lateral one on the orographically left side, and a medial one (Figs. 3–6). The medial moraine is noticeably more elevated than the lateral moraine and has deep, transverse crevasses in its upper part. The right side of the medial moraine is mostly debris covered and contains several large boulders. The ice surface between the two moraines is largely debris free with a few patches of medium to fine grain sized debris. Beginning at the terminus, there is also a long, narrow strip of debris consisting of mostly schist.

In the upper half of the tongue, there are noticeable crevasses in the shape of concentric circles surrounding two points of the ice surface. The ice surface inside these two bundles of crevasses has sunken in, forming two funnel-shaped depressions (Fig.7). The surface at the midpoint of the concentric crevasses farther upstream has collapsed, leaving a big hole in the ice. Inside the hole, the bedrock and a large stream of melt water is visible.

On the orographically left side in the lower third of the tongue, there is a tall sediment hill (Fig. 8). It is slightly U-shaped with the convex side facing downstream. Furthermore, there is a steep ice cliff on the right side of the glacier terminus leading into a small proglacial lake, which almost stretches to the left side of the terminus (Fig. 9).

The immediate glacier forefield is flat, consists mostly of till and sand and is flooded in most parts from the melt water (Fig. 10). Farther downstream the forefield is made up of inhomogeneous till with more mixed grain sizes, ranging from very fine to boulders.

In the summer of 2017, the tongue of the Tiefenglacier was separated from the upper part of the glacier because the connecting ice mass melted away completely (Oberli 2017).

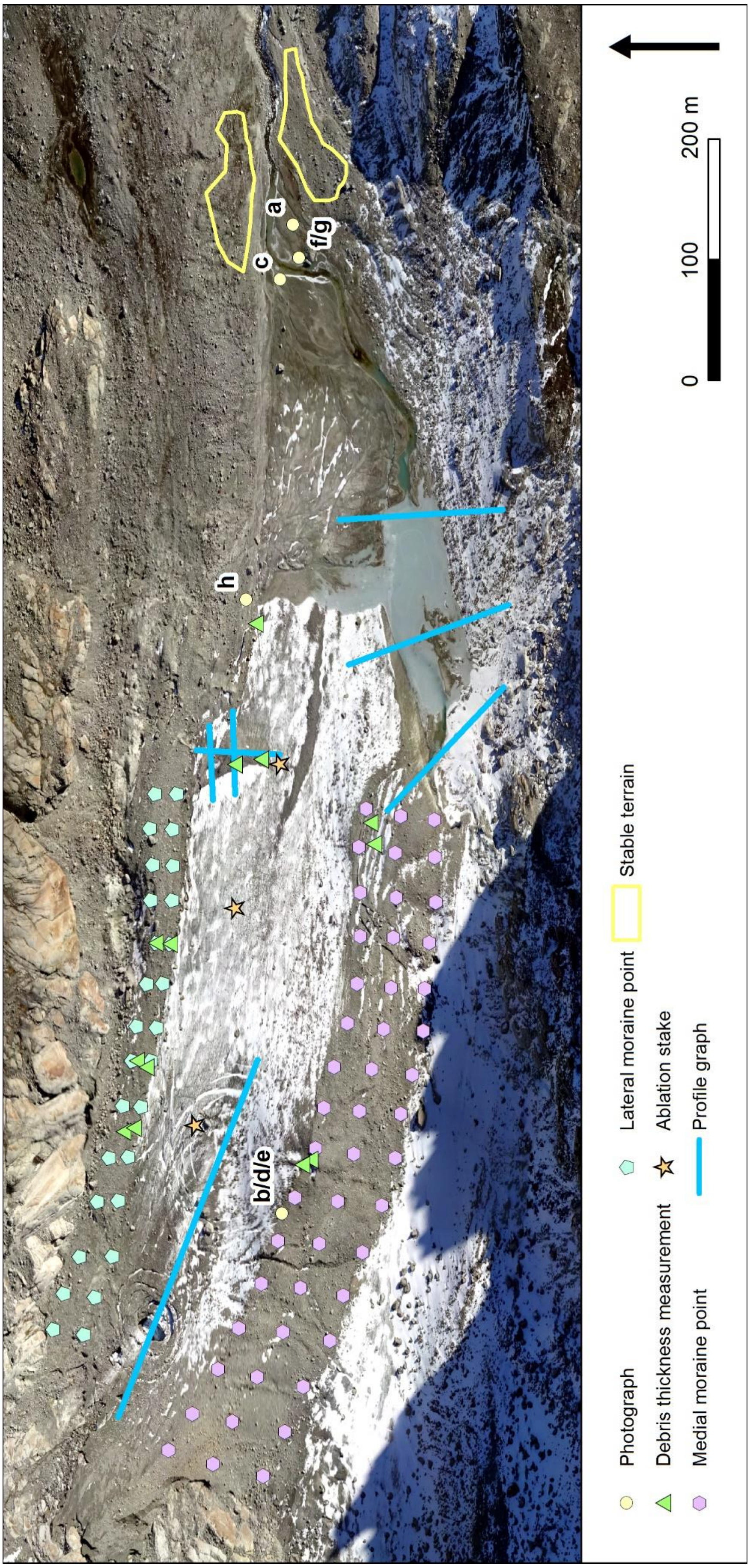

Fig. 3: Orthophoto of the Tiefenglacier's tongue and its forefield in October 2017. The yellow circles indicate where the photographs a–h were taken.

Fig. 4: (a) The Tiefenglacier's tongue as seen from the glacier forefield. In the background the Gross Bielenhorn and the Galenstock are visible.

Fig. 5: (b) The lower lateral moraine as seen from the medial moraine.

Fig. 6: (c) The upper medial moraine is noticeably more elevated than the remaining tongue.

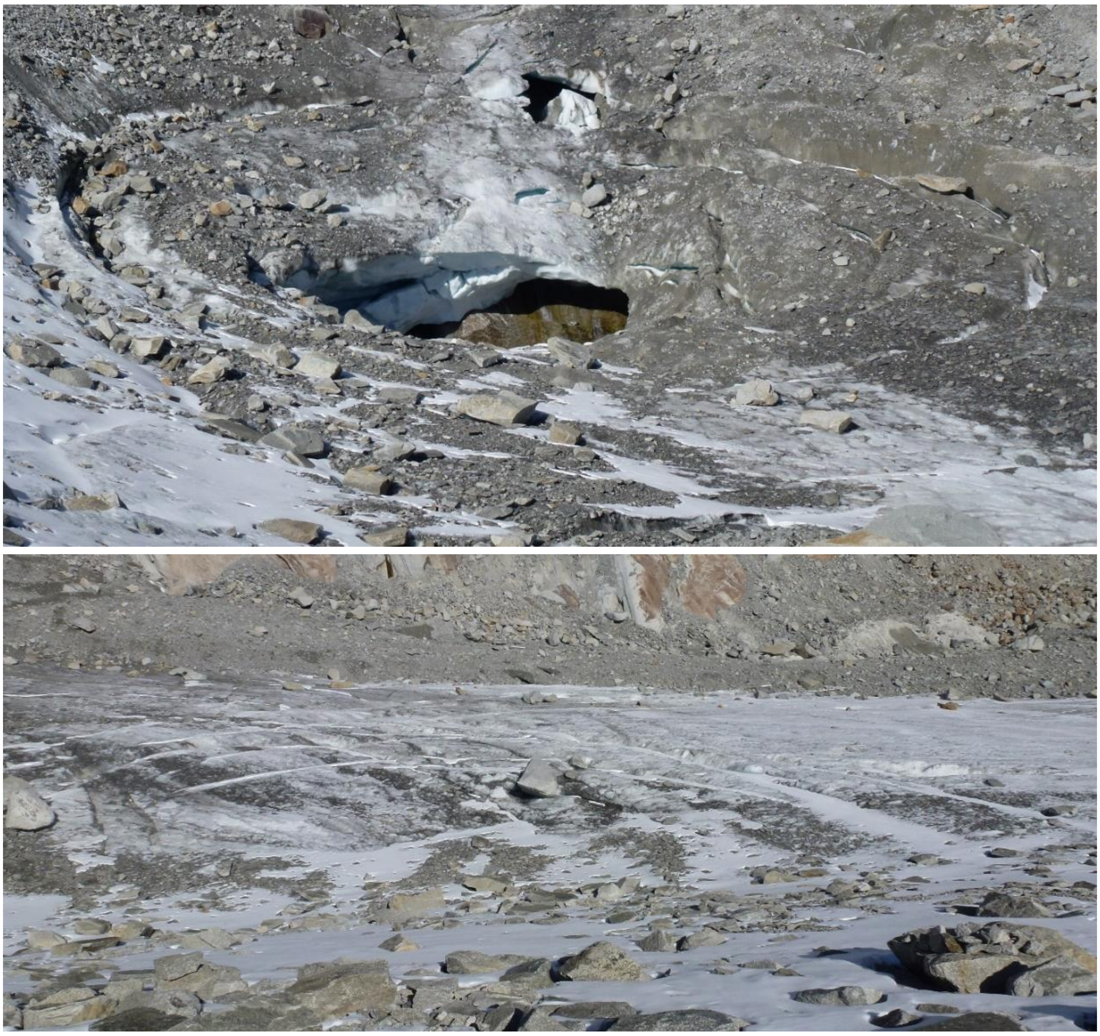

Fig. 7: (d) The funnel-shaped subsidence on the upper glacier tongue with a collapsed ice surface and (e) the lower subsidence.

Fig. 8: (f) The sediment hill on the lower glacier tongue.

Fig. 9: (g) The slightly debris-covered ice cliff reaching into the proglacial lake.

Fig. 10: (h) The immediate glacier forefield is flat, consists mostly of till and sand and is flooded in most parts from the melt water.

2.2.3. History of Tiefenglacier

Due to the glacier’s dynamic nature, its terminus has protruded and retreated many times over the course of its lifetime. Like all the other glaciers in Switzerland, the Tiefenglacier’s extent was much larger and its volume considerably bigger a few centuries ago. Numerous glacial landforms further down-valley, for example the U-shaped valley, roches moutonnées or old terminal and lateral moraines, indicate its historical extents. In the past 150 years, however, the Tiefengletscher has seen a significant loss of ice volume characterized by a retreat of the tongue coupled with thinning (Moll 2012). Since the industrial revolution, this behavior can be attributed to climate change, more specifically to rising air temperatures and the decrease of solid precipitation.

The earliest reliable representation of the glacier’s extent dates back to 1845-1865 in the form of the Dufour map, which is publicly accessible on the mapping platform of the Swiss Confederation (Fig. 11, swisstopo (a)). Around 150-170 years ago, the Tiefenglacier was connected to the Siedelenglacier through the Bühlenstock and its tongue reached further down-valley to an altitude of approx. 2380 m a.s.l. The elevated bedrock, on which the Albert Heim Hut was erected in 1918, was already free of ice at this time.

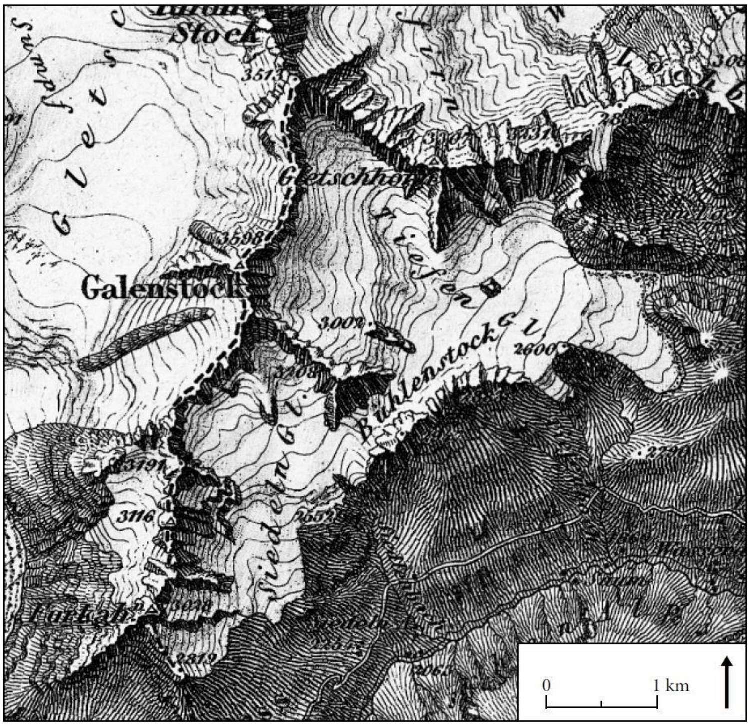

Fig. 11: The Dufour Map depicting the Tiefenglacier’s extent between 1845 and 1865.

Moll (2012) studied the development of the Tiefengletscher between this stage and 2012 with the help of historical and modern maps as well as satellite images. Figure 12 shows the glacier’s outlines between 1850 and 2011, as visualized by Moll (2012). Although there is no data available between the years of 1850 and 1922, the map shows an immense retreat of the glacier over the last 160 years. Between 1850 and 2011, the glacier’s extent decreased from 5.2 km^2 to 2.2 km^2, which is an area loss of approx. 58% (Moll 2012).

After a rather stable period of about 15 years starting in the early 1970s, the glacier seems to have been retreating at an accelerating rate up until today. Taking the ongoing climate change into account, this trend will most likely continue over the next few decades, until the glacier has disappeared.

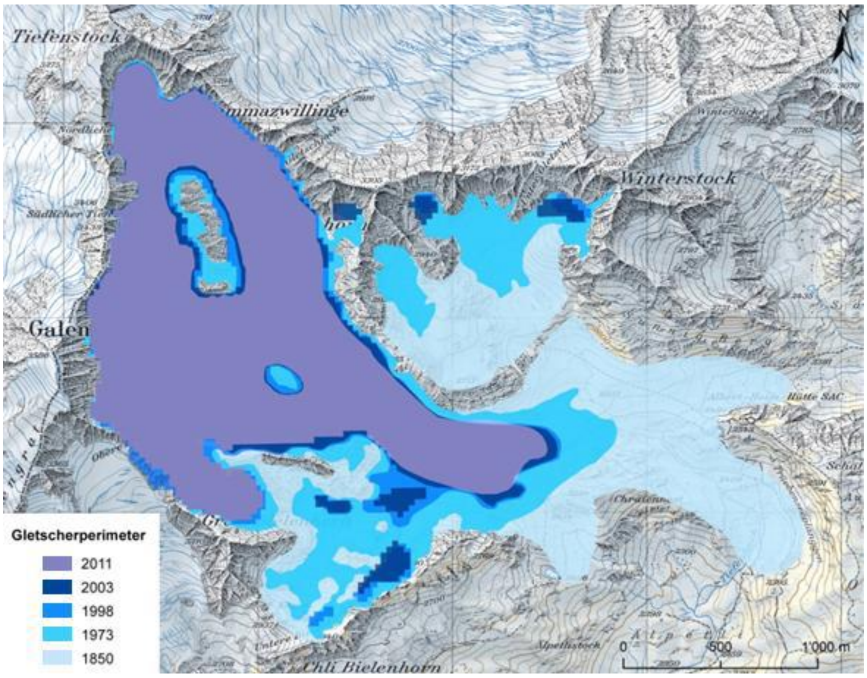

Fig. 12: The Tiefenglacier's outlines between 1850 and 2011 (Moll 2012).

2.2.4. Air temperature

Most glaciers worldwide have been observed to lose substantial amounts of ice mass over the last few decades, and this trend is likely to continue (WGMS). This phenomenon can be attributed to the ongoing climate change, mainly the increase of the average air temperature as well as changing precipitation regimes (Barry 2006, Oerlemans et al. 2009). It is therefore necessary to include these factors when attempting to explain a glacier's behavior, as its mass balance strongly depends on temperature and precipitation.

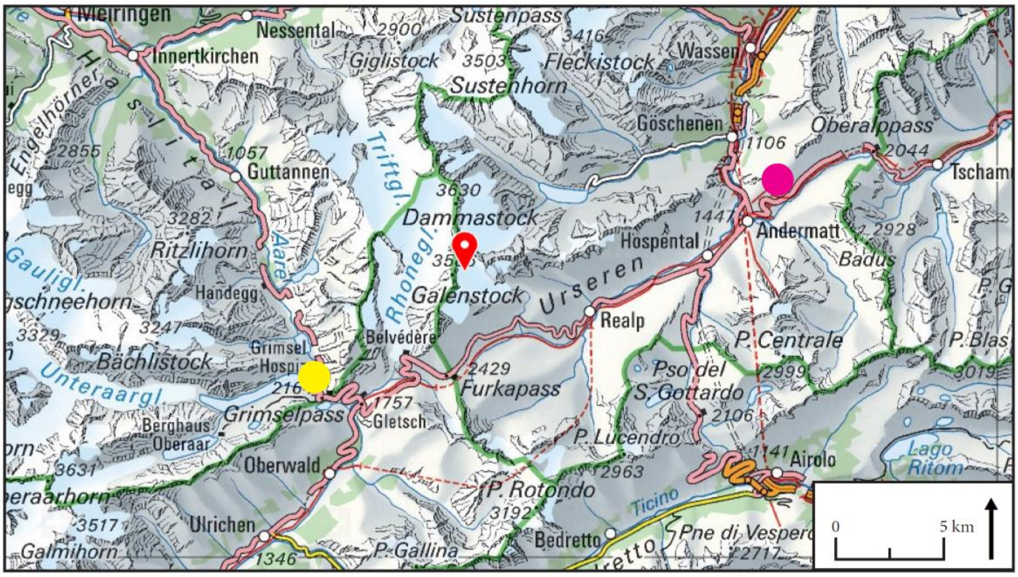

Fig. 13: The locations of the meteo stations Grimsel Hospitz (yellow) and Gütsch, Andermatt (magenta). The Tiefenglacier is marked in red. (Background: swisstopo National Map 1:500´000 from 2013)

In the following section, temperature records from two meteo stations close to the Tiefenglacier are presented. The stations, called Grimsel Hospitz and Gütsch, Andermatt, belong to the automatic monitoring network by the Federal Office of Meteorology and Climatology MeteoSwiss and the data is available upon request on their website (MeteoSwiss). Their exact locations are shown in Fig. 13. Although the meteo station Andermatt would be closer to the Tiefenglacier, Gütsch, Andermatt was chosen, since it is located at a higher elevation as opposed to the valley floor and might thereby better represent the climatological conditions near the glacier. Since both selected stations are not in the immediate vicinity of the glacier, the data needs to be interpreted with caution. Nevertheless, it is deemed sufficiently accurate for the purpose of this study.

2.2.4.1. Grimsel Hospitz

The meteo station Grimsel Hospitz is located at 1980 m a.s.l. and is in operation since December 2008. Fig. 14 shows the average monthly air temperature 2 m above the ground between January 2014 and December 2017. The summer of 2014 seems to have been the coolest within the observed period, whereas the months of July and August 2015 show exceptionally high average temperatures. Although the summer months in 2014 were cooler than the ones in the following years, the months of fall, including September, October and November, were noticeably warmer than usual. While the winter season of 2016/2017 was generally unusually warm, the month of January 2017 showed the lowest average temperatures since the beginning of 2014.

On average, the year 2015 was the warmest year (2.0°C), followed by 2014 (1.4°C), 2017 (1.3°C) and 2016 (1.2°C).

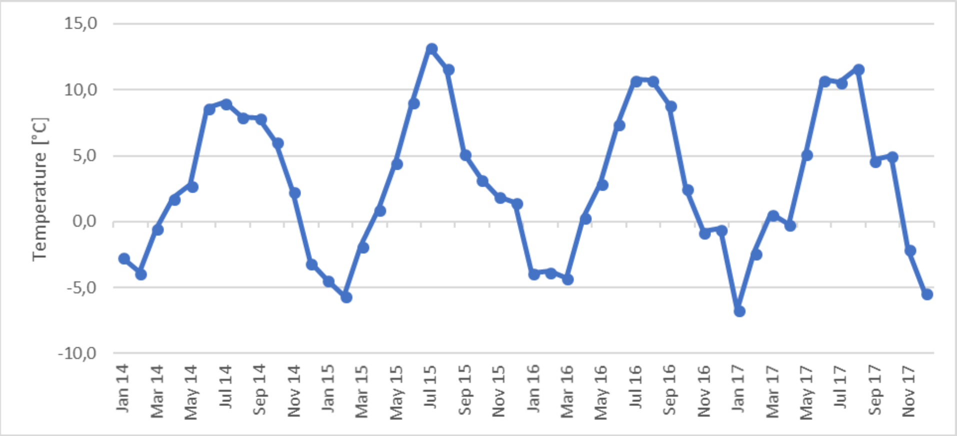

Fig. 14: Average monthly air temperature 2 m above the ground at Grimsel Hospitz from January 2014 to December 2017.

2.2.4.2. Gütsch, Andermatt

Gütsch, Andermatt lies at 2283 m a.s.l. and measures a variety of meteorological parameter since September 2005. In Fig. 15, the average monthly air temperature 2 m above the ground is shown. Fresh snow data is not available at this station. The temperature shows a development very similar to the one at Grimsel Hospitz, but on average about 1–1.5 °C cooler. Since the Tiefenglacier lies approximately in the middle of those two meteo stations, it can be assumed that the relative behavior of the temperature around the glacier tongue is similar. Due to the higher elevation of the tongue, the local temperature is presumably another 1–1.5 °C cooler than measured at Gütsch, Andermatt.

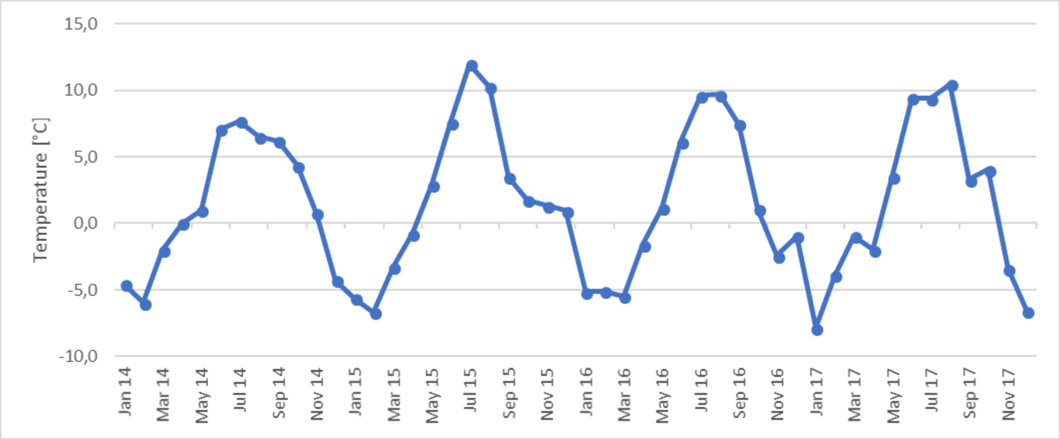

Fig. 15: Average monthly air temperature 2 m above the ground at Gütsch, Andermatt from January 2014 to December 2017.

3. Existing Data

A relatively large amount of existing data collected in the context of the field course GEO 411 from the University of Zurich allows the multi-temporal analysis of the Tiefenglacier's tongue. In the following, details concerning the UAV flights conducted between July 2014 and July 2017 are presented. Further, field reports written by students who attended the field course are presented including brief descriptions of the data extracted for this study.

3.1. UAV images July 2014 – July 2017

In order to study the glacier's development and compare its current state to previous ones, UAV images acquired over the past few years were used. These images were captured in the context of the course GEO 411 from the Department of Geography (GIUZ) at the University of Zurich, Switzerland. In mid-July of the years 2014 to 2017, participating students went under the supervision of GIUZ staff to the Albert Heim Hut near the Tiefenglacier to conduct own measurements and answer previously defined glaciologic and geomorphologic research questions. During one day of each of these excursions, a UAV equipped with a camera was flown by Dr. Johann Müller to take a series of images of the glacier tongue and its surroundings. In a next step, the collected images were then processed using the software Pix4D to create orthophotos and raster-based digital elevation models (DEMs). However, these processed images cannot be used for further calculations in this study as the horizontal and vertical offsets between them is too high. Further details about the drone used and the additional post-processing of the images can also be found in Chapters 4.1.1. and 4.3.

Orthophotos are geometrically corrected, or orthorectified, aerial photographs. Images taken from UAVs usually show variance in scale and displacement of relief due to the perspective of the sensor (Habib et al. 2007). The orthorectification of such images aims to eliminate those distortions, resulting in images which display the true geographic location of objects. Orthophotos can therefore be interpreted the same way as maps, as each point on the image is represented as being looked at from the vertical (Habib et al. 2007).

DSMs use a terrain's elevation data to construct a three-dimensional representation of the surface or terrain. The term digital elevation model (DEM) commonly refers to elevation models without specifying whether it represents the surface or the terrain. While DSMs represent the surface, including objects such as plants and humanmade structures, digital terrain models (DTMs) only refer to the bare ground without said objects (Li et al. 2005). The DSMs in this study always refer to surface models, meaning all objects present in the field which are bigger than the ground sampling distance (GSD) are visible in the model. DSMs are essential for glaciomorphologic analyses and calculations, because largescale elevation differences can be quickly computed using appropriate software.

At each visit of the Tiefenglacier, one orthophoto and one DSM were produced. The flight altitudes of the UAVs were chosen based on the extent of the area being covered. The varying flight altitudes as well as the usage of different cameras affect the GSD of the captured images.

Table 1 shows the dates of the flights, the covered areas, the GSD, the camera model, its sensor dimension and the number of images captured. For the sake of completeness, the details for the flight carried out for this study in October 2017 is shown as well.

Table 1: Details about the UAV flights undertaken over the Tiefenglacier.

Date of flight	Area covered [km2]	Average GSD [cm]	Camera model	Pixel	Sensor dimensions [mm]	Number of images
17.07.2014	0.36	5.13	Canon IXUS125HS	4608x3456	6.17 x 4.639	211
14.07.2015	0.488	11.15	Canon IXUS125HS	4608x3456	6.172 x 4.629	151
11.07.2016	1.135	11.13	SONY DSC-WX220	4896x3672	6.170 x 4.627	60
20.07.2017	0.29	2.5	DJI FC220	4000x3000	N/A	287

3.2. Field reports

During the above-mentioned field courses of GEO 411 the students formed groups to work on individual projects on the Tiefenglacier. At the end of the courses, each group handed in a project report containing research questions, data from the experiments as well as analyzed and discussed glaciological topics. Since the students were free to choose a subject to work on, there is a wide range of data available in these reports, which will be used in the context of this study.

Table 2 shows the selected reports which contain some of the data used in this study. In the following, the most relevant methods the students used to conduct measurements are presented.

Table 2: Selected field reports from the field course GEO 411, including dates of the field courses, report titles, extracted data used for this study, original authors and reference.

Field course date	Report title	Extracted data for study	Authors	Reference
13. – 18. July 2014	Investigation of the actual and former glacier bed of the Tiefenglacier	GPR	Simon Hafner Jacqueline Huber Annina Ruppli Anina Stäubli	Hafner et al. 2014
13. – 18. July 2014	The effect of supraglacial debris on surface melt and terminus evolution	Ablation GPR	Manuala Hasler Katharina Kaelin Claudia Mazenauer Martina Meyer Regula Pfister	Hasler et al. 2014
12. – 17. July 2015	Effect of glacial debris cover on glacier melt rate: A case study at the Tiefenglacier, Switzerland	Ablation	Corina Achermann Kati Böhler Madlaina Juvalta Christian Kuenz	Achermann et al. 2015
12. – 17. July 2015	Morphology and processes related to the disintegration and downwasting of the tongue of Tiefengletscher	Ablation GPR	Sandra Burkhalter Florian Denzinger Anna Holzbecher	Burkhalter et al. 2015
12. – 17. July 2015	Project Report Field Seminar Tiefengletscher	Ablation dGPS	Samuel Mösch Michael Peneder Annette Ramp Andrea Walter	Mösch et al. 2015
10. – 15. July 2016	Project Report	Ablation GPR	Rahel Aus der Au Melanie Graf Christine Schärer Stefanie Wermelinger	Aus der Au et al. 2016
16. – 21. July 2017	Subglacial Overdeepenings: Is the Bikini a Must-have for visiting the Albert Heim Hut in the Future?	GPR	Laura Büchler Caroline Gassmann Olivia Schmid Teresa Steinert Larissa Sutter	Büchler et al. 2017
10. – 15. July 2016	Effect of glacial debris cover on glacial tongue geometry and melt rates	Ablation	Martin Engeler David Hanimann Bertina Hug Oliver Hunziker	Engeler et al. 2016

3.2.1. Ground-penetrating radar (GPR)

GPR is a non-destructive geophysical technique that is used to obtain insights into the structure and extent of near-surface objects using radar pulses (Griffin & Pippett 2002, Neal 2004). It is usually applied in archaeology, ground water level mapping, sedimentology as well as glacier ice thickness measurements. It works by either carrying a GPR device or flying it over the surface of the studied ground material in a constant speed. The radar pulses, produced by a transmitter typically in the range from 10 MHz to 1.5 GHz, reflect off objects in the ground and get detected by the inbuilt receiver. The propagation velocity of the radar wave strongly depends on the ground material and its water content and thus needs to be chosen accordingly before the measurement. Table 3 shows average wave propagation velocities of different materials. Since the measurements for these project reports were exclusively conducted on the Tiefenglacier, the students chose a propagation velocity of 0.16 m/ns.

Table 3: Average wave propagation velocities of different materials at 100 MHz (v). Also included are dielectric constant (K), conductivity (σ) as well as attenuation (a). (Davis and Annan 1989)

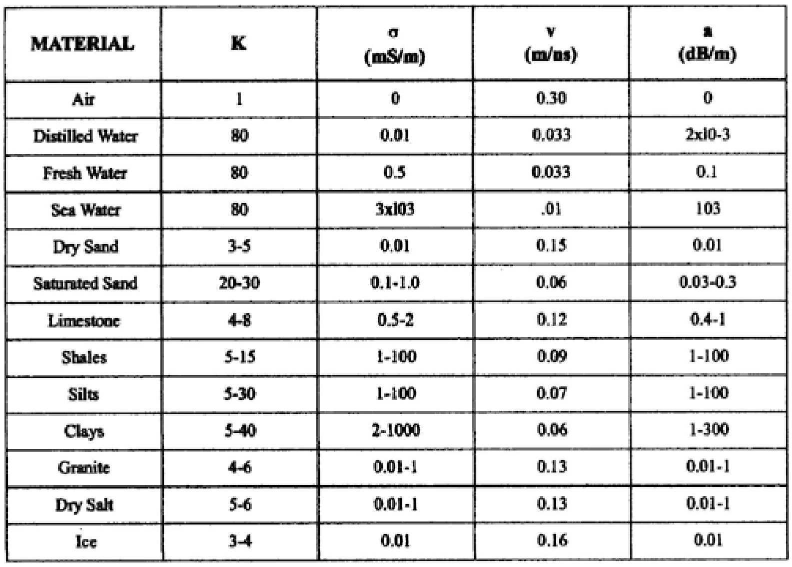

MATERIAL	K	σ (mS/m)	v (m/ns)	a (dB/m)
Air	1	0	0.30	0
Distilled Water	80	0.01	0.033	2x10-3
Fresh Water	80	0.5	0.033	0.1
Sea Water	80	3x103	.01	103
Dry Sand	3-5	0.01	0.15	0.01
Saturated Sand	20-30	0.1-1.0	0.06	0.03-0.3
Limestone	4-8	0.5-2	0.12	0.4-1
Shales	5-15	1-100	0.09	1-100
Silts	5-30	1-100	0.07	1-100
Clays	5-40	2-1000	0.06	1-300
Granite	4-6	0.01-1	0.13	0.01-1
Dry Salt	5-6	0.01-1	0.13	0.01-1
Ice	3-4	0.01	0.16	0.01

The distance from the antenna to the reflector in the ground can be calculated with the known propagation velocity of the waves and the time it takes for them to arrive at the receiver. The small variations of the return signals are represented in radargrams, which can be analyzed after the measurement to identify buried objects, features, a change in the material's properties or voids. The frequency of the waves is chosen based on the material to be studied, the planned penetration depth and resolution. While low frequencies result in high penetration depth and low resolution, high frequencies are suitable for low penetration depth and high resolution. Fig. 16 shows the basic setup of a GPR in use, including the transmitting and receiving devices. The first wave to arrive is the air wave above ground at the speed of light, followed by the ground wave which travels through the ground directly to the receiver. After that,

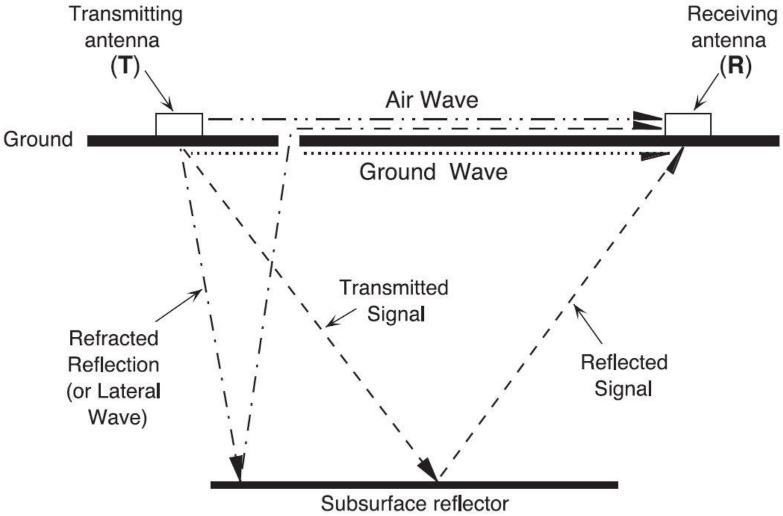

Fig. 16: Conceptual sketch of a GPR device in use, including the transmitting and receiving antennae, the air wave, the ground wave, a reflected wave as well as a lateral wave (Neal 2004).

the radar pulses reflected by reflectors in the ground are detected as radio waves by the receiver. Additionally, lateral waves might be present, which get refracted along the air-ground interface (Neal 2004).

For the projects in the context of GEO 411, the students used a rough terrain antenna (RTA) by Swedish manufacturer MALÅ Geoscience with frequencies of 25 and 50 MHz. The postprocessing of the radargrams was carried out with the ReflexW software. While GPR offers fast data acquisition and a high structural resolution of interfaces and shear horizons, the penetration depth of the radar signal is strongly diminished in conductive material, such as water (Vieli 2016). Further, metallic objects near the antenna lead to disturbing reflections, which complicates the correct interpretation of radargrams (Vieli 2016).

3.2.2. Debris thickness and ablation measurements

Most groups of students conducted debris thickness measurements at various locations on and around the Tiefenglacier as well as ablation measurements on the glacier surface. The methods used vary between the groups, so naturally a certain degree of uncertainty and error needs to be expected when working with these data. The debris thickness measurements were generally conducted using rulers and multiple measurements per site. The thickness was determined by measuring from the ice surface to the top of the debris layer.

The ablation stakes 10, 11 and 12 were installed on 09.07.2014 and kept in place until 11.07.2016, except for 12, which was kept in place until 19.10.2017 (Fig. 17). Several groups took advantage of the relatively long measurement period and included the acquired data in their reports. Further, additional stakes were installed by the students in various locations for the course of the field excursions.

Fig. 17: The location of the ablation stakes 10, 11 and 12 on the Tiefenglacier's tongue.

3.2.3. Differential Global Positioning System (dGPS)

dGPS is a method used to increase the accuracy of GPS measurements via reference stations on the ground, whose exact positions are well known. Positions on the earth's surface calculated using ordinary GPS devices (rovers) are usually accurate to a few meters. These inaccuracies are caused by a couple of factors: First, the exact orbit of the GPS satellite is not known to the receiver. Second, small variations in the signal velocities occur between the satellite and the receiver when the signal passes through the earth's atmosphere. The reference stations used for dGPS calculate their own positions using GPS satellites and compare the result with their true position. The difference between the calculated and the true position then serves as a correction factor, which is sent to nearby dGPS devices in real time if there is a working radio connection. If no radio connection is available, the correction factor can be used for post-processing of the measurements. The calculated position of the receiver typically improves from the range of meters to the range of centimeters. However, the accuracy of the correction factor strongly depends on the distance between the reference station and the rover, since the factor is calculated based on the surrounding atmospheric conditions. Therefore, the farther away the dGPS device is used from a reference station, the less accurate its calculated position is.

In Switzerland, swisstopo offers a permanent and stable network of global navigation satellite system (GNSS) stations called Automated GNSS Network for Switzerland, or AGNES (swisstopo (b)). However, no working connection could be established on the Tiefenglacier during the field courses because of the high relief surrounding it. Mösch et al. (2015), who used dGPS to track the glacier's flow velocity, thus had to post-process their position records.

4. Methods

In the following, the methods used in this study are presented. First, two flights carried out with a UAV as well as debris thickness measurements conducted during the field visit in October 2017 are described. Subsequently, the processing of all available UAV images in Agisoft PhotoScan and the post-processing in ArcMap, including an accuracy assessment of the DSMs and the difference images, are presented. Further, the mapping process of the orthophotos is explained, followed by a description of the various ways the DSMs and the difference images have been used to analyze elevation changes. Moreover, the analysis of the surface ablation as well as the supraglacial debris are outlined. In a last step, the calculation of the ice flow velocity by means of feature tracking is described.

4.1. Field visit October 2017

In order to get an overview of the Tiefenglacier's current state, a field visit was undertaken on the 19 October 2017 under the supervision of Prof. Dr. Andreas Vieli and PhD student James Ferguson. The goal of the visit was to get an impression of how the glacier tongue had evolved since the author's last trip to the glacier in July 2016. Further, debris thickness measurements at various locations on the glacier were conducted and two UAV flights were carried out to acquire new aerial images of the tongue and its surroundings. Using SfM techniques, these images were later used to create orthophotos and DSMs. The day of the visit was sunny at first, with clouds gathering in the afternoon and slightly windy from the North-East. The glacier tongue had a 5-10 cm thick discontinuous snow cover, with the moraines being mostly snow free.

4.1.1. UAV flights

The UAV flights were planned with the goal to take new aerial images of the Tiefenglacier's tongue and its surroundings. The acquired images allow to produce an orthophoto and a DSM of the current state of the glacier, which are suitable for the comparison with the existing UAV images from previous years.

The UAV used is an eBee drone by Swiss manufacturer senseFly (Fig. 18). It is equipped with an autopilot and a GPS sensor which allows the user to plan the flight routes beforehand and let it perform the flight and the landing fully autonomously. To start the flight, the drone's motors need to be turned on by shaking the drone and then thrown into the air, at which point it begins its planned route. The landing was chosen to be performed in the flat glacial forefield at a safe distance from elevated peaks since they pose a danger to the drone. Any rocks and boulders that could not be moved from the landing site and could therefore damage the drone were covered with jackets.

Fig. 18: The eBee drone by SenseFly used for the capturing of the aerial images.

The software eMotion by senseFly was used to plan and monitor the flights on site (senseFly). The flights were intentionally performed at a relatively high elevation above the ground to avoid any rock surfaces, since the goal was to capture the entire tongue and its surroundings, including the glacier forefield. This was done at the expense of the resolution of the acquired images. It was regarded as more important to capture as much of the area as possible, however, than to obtain a high-resolution image.

During the flight, an inbuilt camera took pictures from the ground in predefined intervals. The acquired images were later processed and turned into an orthophoto and a DSM using the software Agisoft PhotoScan by Agisoft. Fig. 19 shows one of the flown routes in green, including the circular ascent and descent as well as the locations the images were taken.

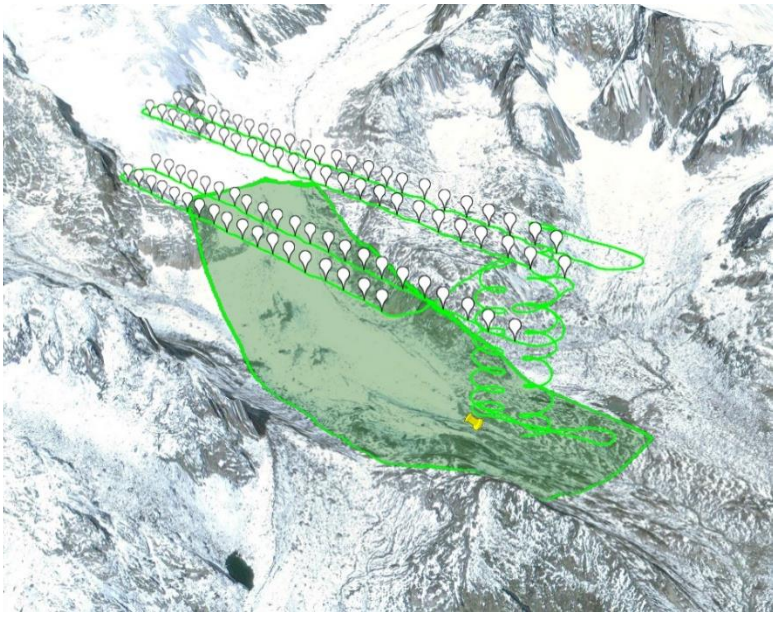

Fig. 19: The flown route and the covered area are shown in green. White pins mark the locations the pictures were taken. (Background: Google Earth. Last access 21.02.2018)

4.1.2. Debris thickness measurements

During the field visit in October 2017, a total of 13 debris thickness measurements on the glacier were conducted. They include the lower and middle lateral and medial moraines as well as the sediment hill. No measurements were conducted in the uppermost parts of the moraines, as they were too steep and featured numerous crevasses at the time. For each measurement, a hole was dug into the debris until the ice surface was visible and three measurements were taken with a folding rule. The distance between the ice surface and the top of the debris layer was measured in a 90-degree angle. The average of the three measurements was calculated and noted as the average debris thickness at the selected location.

4.2. Processing of UAV images

During the two flights, the UAV captured a total of 189 images. Each image was saved with GPS coordinates and the current elevation above ground. This information allows to construct 3D models of the studied area as well as orthophotos and DSMs using a four-step procedure in the software Agisoft PhotoScan (Agisoft user manual).

1. In the first step, a sparse point cloud and a set of camera positions are constructed. By searching for and matching common points on overlapping photographs, PhotoScan calculates the position of the camera for each image, aligns them and refines the camera calibration parameters. Additionally, the Ground control points (GCPs) are marked in the images to increase the overall accuracy of the finished products.

2. The second step consists of the construction of a dense point cloud based on the images and the estimated camera positions.

3. In the third step, PhotoScan reconstructs the geometry of the object by using the previously generated dense point cloud and building a 3D polygonal mesh. The mesh functions as a representation of the surface of the photographed object and gives the user a first look at the product.

4. The mesh can eventually be textured and used to generate orthomosaics as well as DSMs.

4.2.1. UAV flights October 2017

An overview of the selected parameters used to create the orthophoto and the DSM of the UAV flights from October 2017 is given in Table 4. If not otherwise mentioned, the default settings were used as suggested by the Agisoft PhotoScan manual (Agisoft user manual).

The resulting DSM is used as a reference for the quality assessment of the already existing DSMs from previous years. Therefore, the aim was to produce a reference DSM of the highest quality possible. Since the relative accuracy between the reference DSM and the other DSMs is of more importance than the

Table 4: Overview of the selected parameters in Agisoft PhotoScan to produce the orthophoto and DSM of October 2017.

Alignment accuracy	Highest
Generic preselection	Enabled
Reference preselection	Enabled
Key point limit	40´000
Tie point limit	10´000
Adaptive camera model fitting	Enabled
Surface type	Height field
Source data	Sparse cloud
Face count	200´000
Interpolation	Enabled
Dense cloud quality	High
Depth filtering	Mild
Surface type	Height field
Source data	Dense cloud
Face count	High
Interpolation	Enabled
Color correction	Disabled
Hole filling	Enabled

absolute accuracy, however, two versions were created with different dense point cloud quality settings. This way it is possible to choose the reference DSM that produces the smallest offset compared to the DSMs of the previous years.

For the initial alignment of the pictures, the quality setting *high* was chosen to ensure the maximum amount of overlap between the images. The dense point cloud quality was set to *high*, but not *ultra-high*, because of the very long processing time that results from higher quality settings in this step. For the depth filtering of the dense cloud, the lowest setting *mild* was chosen. This option determines to what degree the surface of the generated model is filtered, meaning that small details and complex structures are smoothed out more intensely the higher the setting is. Since the resolution of the acquired images is relatively high and individual boulders need to be recognized for certain aspects of this study, *mild* was the preferred choice.

4.2.2. UAV flights July 2014 – July 2017

The drone images captured during the field courses of 2014-2017 have already been processed once to generate orthophotos and DSMs. A quick visual evaluation of the DSMs in the software ArcMap by ESRI (Environmental Systems Research Institute) revealed, however, that the horizontal and vertical offsets relative to the produced reference DSM were far too big to be useful (see Chapter 5.2. for more details). Therefore, the original drone images were processed anew using the same software, Agisoft PhotoScan, to ensure a high accuracy of the DSMs. For each year, one DSM was produced with the dense cloud quality set to *high*. The remaining settings were, again, set to default (Table 4).

4.2.3. Ground Control Points (GCPs)

Image acquisition with UAVs always involves a certain degree of uncertainty. Factors such as the accuracy of the GPS sensor aboard the drone, the percentage of image overlap, and the quality of the individual images affect the quality of the end result significantly. However, it is important that the DSMs of July 2014–July 2017 match the horizontal and vertical extent of the reference DSM for further calculations in ArcMap. Any shifts between the DSMs would also be represented in the generated difference images, which would render them useless.

For this purpose, GCPs were implemented. GCPs are points on the earth's surface, the exact locations of which are known and can therefore serve as reference points. It is crucial that the GCPs are on stable terrain, meaning that their horizontal and vertical position does not change over time. Furthermore, they should ideally be distributed over the entire imaging area and be easily recognizable (Shahbazi et al. 2015).

For the generation of all orthophotos and DSMs in this study, SwissImage was chosen as reference for the GCPs. SwissImage is an orthophotomosaic of Switzerland's entire surface provided by the Federal Office of Topography swisstopo (SwissImage). Its resolution ranges from 25 cm to 250 cm, whereby the Alpine area, including the Tiefenglacier, has a resolution of 50 cm due to difficult flight conditions during its acquisition. SwissImage can be accessed via a web browser for free in combination with a digital elevation model (swisstopo (a)). Above 2'000 m a.s.l., swisstopo used the *Digitales Höhenmodell DHM25* as a base for the elevation data for the SwissImage orthophotomosaic. The positioning accuracy of SwissImage in combination with the DHM25 is ± 1-2 m, and in hilly terrain ± 3-5 m.

For the selection of the GCPs, stable terrain surrounding the glacier was chosen. This proved to be a challenge, because the non-glaciated area captured by the drones is rather limited, especially in the months of July 2014 and July 2017. Further, the GCPs cannot be placed on surfaces which might contain ice underneath, as the melting of the ice over time could lead to inconsistencies in the elevation. Snow covered surfaces need to be ruled out as well, as the snow also affects the elevation and makes it much more difficult to recognize the exact locations of the GCPs on different images. Ideal locations for the GCPs are therefore bedrock or large stable rocks and boulders. The glacier forefield, for example, contains several large boulders which seem to be stable and are thus used as GCPs.

To create the GCPs in Agisoft PhotoScan in the first step of the above described four-step procedure, all points were first selected in SwissImage for every acquisition date separately based on the above listed criterions. The GCPs were then manually placed in each drone image along with the coordinates and elevation extracted from SwissImage. Agisoft PhotoScan then uses the GCPs to create the dense point cloud and eventually a reconstructed 3D model of the glacier and its surroundings. Fig. 20 shows the generated orthophoto of July 2015 including the selected GCPs. The remaining orthophotos with the mapped GCPs can be found in Appendix 10.1.

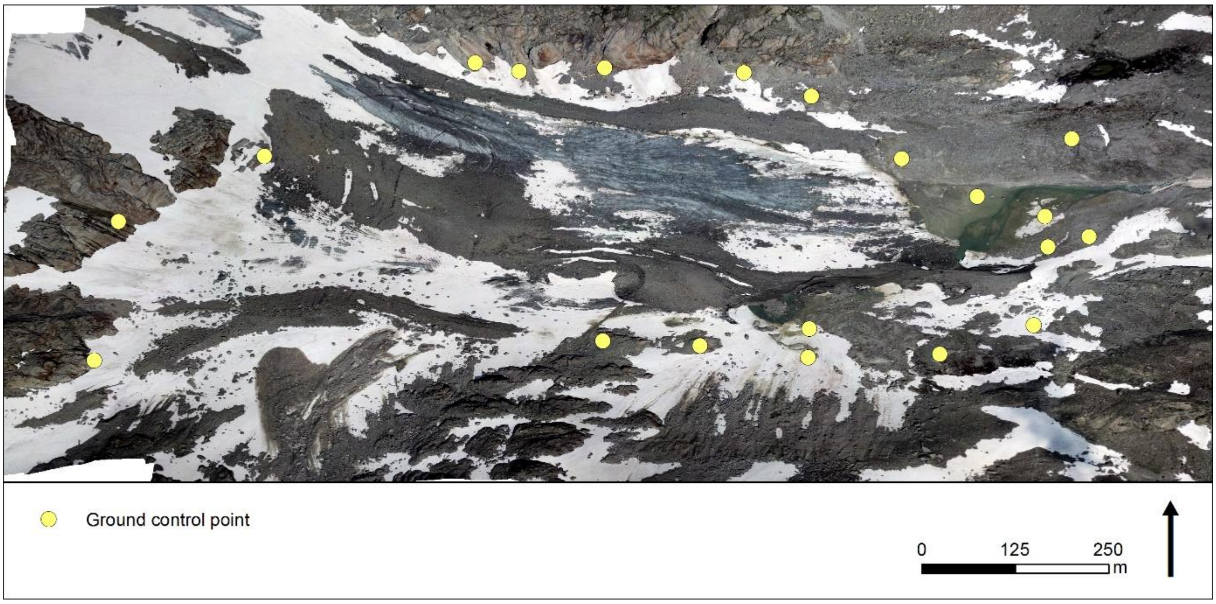

Fig. 20: Selected GCPs for the orthophoto and DSM of July 2015. The background is the orthophoto of July 2015.

4.3. Post-processing of UAV images

The following section describes the post-processing of the UAV images in ArcMap. It starts with an outline of the methods used to assess the accuracy of the DSMs and the difference images, which is necessary to determine the validity of the results. Further, the steps needed to resample the DSMs and create hillshades are explained.

4.3.1. Accuracy assessment of DSMs

Before using the generated DSMs for further calculations and analysis, it is important to determine their relative accuracies. DSMs that show horizontal or vertical shifts relative to a selected reference DSM lead to erroneous elevation values when creating difference images. For all calculations, the DSM of October 2017 was selected as the reference DSM. The following chapter describes the approach to determine systematic shifts of the DSMs using co-registration as well as the calculation of various statistical uncertainty measures referring to their vertical dimensions.

4.3.1.1. Co-registration

Despite the use of GCPs during the generation of the DSMs, they might show systematic shifts relative to each other. Since difference imaging works by overlaying two DSMs and calculating the difference in elevation, horizontal displacement of the models leads to unrealistic values. It is therefore important to determine the shifts and, if necessary, minimize them through a process called co-registration.

To determine the horizontal shifts of the DSMs relative to the reference DSM, the *Co-registration Tool* by Nuth & Kääb (2011) as well as a step-by-step tutorial written by Rastner (2015) were used. The tool is implemented in Microsoft Excel and requires the user to determine the elevation difference for each pixel over stable terrain between a DSM and the reference DSM in ArcMap. By adding the aspect and slope values of each raster cell of the reference DSM, the tool is able to compute any horizontal and vertical shift between the two DSMs. In a first step, the elevation differences of each pixel are divided by the tangent of the slope and plotted against the aspect, visualizing a characteristic relationship between those two parameters (Nuth & Kääb 2011). A cosine function then gets fitted to the plot, resulting in the vertical and horizontal shift parameters. Subsequently, the DSM then needs to be shifted according to the calculated parameters in order to align it to the reference DSM.

All shifts need to be calculated over stable terrain relative to the reference DSM of October 2017. The stable terrain is located in the glacier forefield in an area where no ice or snow is present and rockfall is minimal (Fig. 21). It proved to be a difficult task to find terrain without vertical elevation changes for the same reasons mentioned in Chapter 4.2.3. Therefore, the stable terrain has a rather small extent to prevent the inclusion of terrain showing elevation changes.

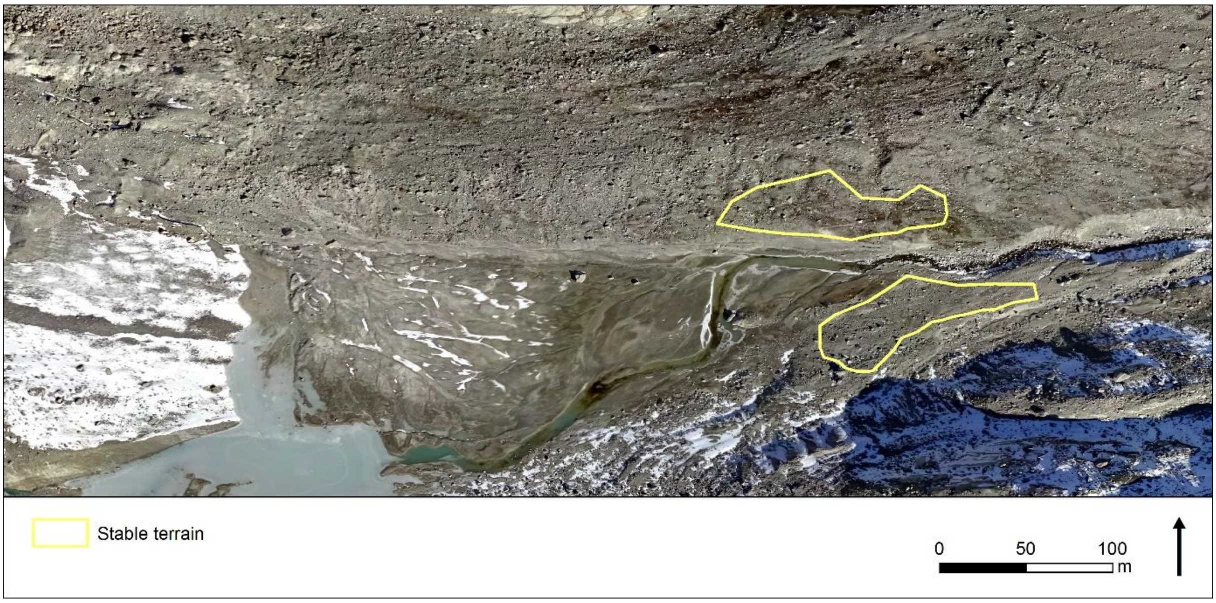

Fig. 21: Selected stable terrain in the glacier forefield.

4.3.1.2. Quantitative accuracy assessment

The vertical accuracy of every generated DSM between July 2014 and July 2017 was calculated relative to the DSM of October 2017. For the quantitative assessment of the vertical accuracy, common statistical uncertainty measures were used. The systematic uncertainty is expressed as the mean elevation difference (MED), which describes the bias of a DSM relative to the reference DSM. Since the MED includes both negative and positive values, they might cancel each other out, resulting in an underestimated bias. Therefore, the absolute mean error (AME) is added, which calculates the mean error using absolute values (Müller et al. 2014). The stochastic uncertainties are defined by the standard deviation (STD) and the standard error (SE) and stand for the random variability of the elevation values over stable terrain (Eq. 1–4, Bolch et al. 2011, Höhle & Höhle 2009). All statistical values were calculated using the *zonal* *statistics* tool in ArcMap. The calculated errors refer to the differences over a selected stable terrain relative to the reference DSM of October 2017.

$$MED = \frac{1}{n}\sum_{i=1}^{n} x_i \tag{1}$$

$$STD = \sqrt{\frac{1}{n}\sum_{i=1}^{n} (x_i - MED)^2} \tag{2}$$

$$SE = \frac{STD}{\sqrt{n}} \tag{3}$$

$$AME = \frac{1}{n}\sum_{i=1}^{n} |x_i| \tag{4}$$

n: Number of GCPs used for the creation of the respective DSMs

xi: Elevation difference of a pixel in a DSM relative to the reference DSM of October 2017

4.3.1.3. Difference images

The assessment of the differencing images' uncertainties was carried out using the same measures as for the accuracy assessment of the generated DSMs: The mean elevation difference MED, the absolute mean error AME, the standard deviation STD as well as the standard error SE. However, rather than using only the DSM of October 2017 as reference for the calculations, the measures were calculated separately for each differencing image.

4.3.2. Resampling

Due to the use of two camera models and varying UAV flight conditions, each of the produced DSMs has a different spatial resolution. When computing difference images in a GIS-environment by subtracting one DSM from another, this can lead to unwanted effects in the resulting image. Therefore, the DSMs were resampled to a uniform cell size using the *Resample* tool in ArcMap to avoid such errors. For this, the cell sizes of the DSM from October 2017 were chosen as the reference, since this model also serves as a reference DSM for the accuracy assessments. Further, this DSM has the largest GSD, and resampling to a larger pixel size is preferable in this case, as downscaling could lead to values that do not exist in the original DSM. The resampling was performed bilinearly because of the continuous nature of the data. Resampling using a cubic convolution could be considered for continuous data as well, however this technique can lead to values outside the range of the input raster (ArcGIS Pro).

4.3.3. Hillshades

For each DSM a hillshade was created using ArcMap. For the azimuth angle of the light source and the altitude angle of the light source above the horizon, the default settings of 315 and 45 degrees were chosen, respectively.

4.4. Mapping

In order to get an overview of the features and surface types of the Tiefenglacier's tongue, each produced orthophoto was mapped in ArcMap. This further allows to track the feature's developments on a 2D scale. Features and surface types mapped include the lateral and medial moraines, the sediment hill, the ice cliff, the ice surface depressions in the upper tongue and their surrounding crevasses, clean ice as well as debris-covered ice. The extent mapped ranges from the glacier terminus to the steep slope connecting the tongue with the rest of the glacier, as well as from the outer side of the lateral moraine to the outer side of the medial moraine. This ensures that all the features which are analyzed in more detail in this study are included.

Mapping each feature and surface type in a uniform style across all orthophotos allows to trace their extents over the three studied years. However, the mapping of features is not always trivial, as snow cover, clouds or debris obstruct the view in the orthophotos. In such cases, the orthophotos from the previous and following years were used as an aid to obtain plausible results. Additionally, setting the borders for some features is to a certain degree subjective, as e.g. determining where the termini of the moraines are located, since there is a smooth transition between them and the glacier forefield. To this end, the difference images resulting from the DSM of the year being mapped and the one of the previous year were used to map the extent of the moraines. Any surface lowering present in the area of the moraines' termini was subsequently interpreted as ice being present and therefore part of the moraines. Naturally, the sediment farther downstream of this area, which does not contain any ice, technically belongs to the moraines as well, but since the dynamic aspect of the moraines is of interest and the presence of ice can easily be mapped with the difference images, this strategy was chosen.

4.5. Elevation changes

In the following, four different methods used to analyze elevation changes occurring the on the Tiefenglacier's tongue using the generated DSMs and difference images are presented.

4.5.1. Difference images

Due to the rapid disintegration of the Tiefenglacier's tongue in recent years, it experiences strong elevation changes, albeit inhomogeneously distributed. Difference images produced in a GIS-environment aid to visualize and interpret these surface elevation changes. Each difference image was created by subtracting the older resampled DSM from the newer one using the *Raster Calculator* tool in ArcMap. The result is a continuous raster depicting the surface elevation difference between the two DSMs. Using all available DSMs from July 2014 to October 2017, every possible combination of two DSMs was used to produce a total of 10 difference images. For the visualization of these images, the software QGIS was used.

4.5.2. Comparison upper vs lower tongue

Surface ablation data obtained from permanently installed ablation stakes on the tongue suggests that all detected surface lowering in debris-free or slightly debris-covered areas was caused by ablation except for the area in the upper half of the tongue containing the concentric crevasses. In this zone, the ice surface experienced a larger downwasting than the ablation measurements could explain. To confirm this observation and visualize the extent of the additional surface lowering, difference images of the upper and lower halves of the tongue were produced separately for comparison. The moraines and the ice cliff were excluded from these images, as their developments are strongly influenced by other factors than surface ablation, such as thick debris covers or steep slopes leading to the break-off of ice masses. The difference images were produced the same way as described above, with all possible combinations from all DSMs.

4.5.3. Profile graphs

Difference images can be difficult to interpret because they depict elevation changes of three-dimensional objects on a two-dimensional plane. Profile graphs (hereinafter simply referred to as “Profiles”) are a helpful instrument in ArcMap to visualize the surface elevation of an object in a side view. It works by drawing a line over the surface to be studied with the *3D Analyst* tool, which generates an output showing the elevation along the drawn line. Creating multitemporal profiles allows to visualize them in the same plot. This represents a useful way to track the developments of the surface elevation of features found on the glacier tongue. Multiple profiles were generated for each feature, including the sediment hill, ice cliff, lateral and medial moraines and the surface lowering present near the concentric crevasses. The elevation data generated by the graphs was extracted and visualized in Microsoft Excel.

4.5.4. Point-based elevation differences

The shapes of the moraines suggest that they experience a reduced ablation rate compared to the remaining tongue. This phenomenon was expected and can visually be identified in the difference images, as the relatively thick debris cover on the moraines efficiently insulates the ice underneath. However, it is difficult to assess whether the ablation on the moraines is distributed equally using only the difference images. To better visualize the spatial variability of the ablation rates on the moraines, a total of 76 points were placed along the moraines using DSMs and orthophotos in ArcMap. For each point, its elevation value was extracted from the DSMs of the years 2015-2017 and saved in a separate file. The DSM of the year 2014 was not considered, since it only covers the lower half of the tongue. The elevation differences relative to the year 2015 were then calculated for each point. The points were distributed as longitudinal lines on the lateral moraine, and three longitudinal lines on the medial moraine with a distance of approx. 30 m from each other. More than one longitudinal line per moraine was chosen in order to study whether the ablation rate on one side of the moraine differs from the other side. The lines on the lateral moraine consist of 14 points each, whereas the lines on the medial moraine have 16 points each. Subsequently, a separate plot was generated for each of these lines.

4.6. Ablation

The ablation stakes 10, 11 and 12 were used to exclusively measure the surface ablation at selected locations on the tongue. However, these measurements only reveal how much surface ice melted, and do not provide any information about other factors affecting the surface elevation.

Comparing the ablation data with the surface elevation data calculated with the DSMs allows to draw conclusions about whether dynamic replacement is present or not. This was done by calculating the difference between the cumulated surface ablation and the cumulated surface elevation difference for each stake:

$$\frac{dh}{dt} - \dot{b} = -\frac{dQ}{dx} \qquad (5)$$

dh/dt = surface elevation change over time, $\dot{b}$ *= ablation, and dQ/dx = dynamic replacement*

4.7. Supraglacial debris

Supraglacial debris has a significant effect on surface ablation and therefore on the dynamics of the tongue due to its insulating and melt-enhancing properties. The following section covers the methods used to map the distribution of the supraglacial debris as well as the analysis of its influence on surface ablation.

4.7.1. Distribution

In addition to the mapping of the glacial features and the presence of supraglacial debris in Chapter 4.4., the distribution of the debris is mapped in more detail, taking the rounding and grain size into account. This was only done for the orthophoto of October 2017, since much of the mapping relied on photographs taken on site during the field visit and own measurements and observations. Although the debris cover of the tongue of previous years was described to some degree by students in their field reports, the amount of information was not enough to map the debris distribution with a reasonable degree of certainty.

The debris cover types were split into twelve separate categories, according to location, grain size and roundness. The grain size was classified according to Wentworth (1922) (Table 5). However, as the grain sizes were only roughly measured with a folding rule during the field visit and the debris strongly varies in size, the classification was limited to sand, pebbles, cobbles and boulders. The roundness of the particles was divided into four different categories: Very angular, angular, rounded and well-rounded. A brief description of each debris-cover type was added including details such as debris cover continuity or sorting.

Table 5: Grain size classification according to Wentworth (1922).

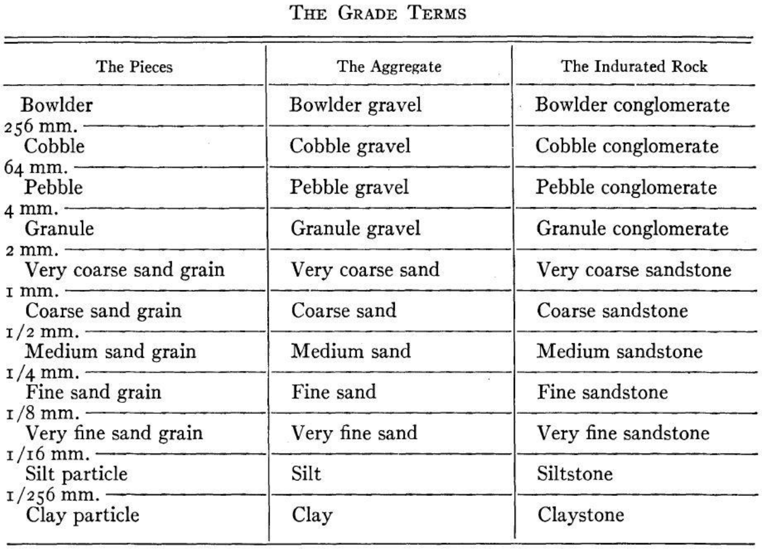

THE GRADE TERMS

The Pieces	The Aggregate	The Indurated Rock
Bowlder	Bowlder gravel	Bowlder conglomerate
256 mm.		
Cobble	Cobble gravel	Cobble conglomerate
64 mm.		
Pebble	Pebble gravel	Pebble conglomerate
4 mm.		
Granule	Granule gravel	Granule conglomerate
2 mm.		
Very coarse sand grain	Very coarse sand	Very coarse sandstone
1 mm.		
Coarse sand grain	Coarse sand	Coarse sandstone
1/2 mm.		
Medium sand grain	Medium sand	Medium sandstone
1/4 mm.		
Fine sand grain	Fine sand	Fine sandstone
1/8 mm.		
Very fine sand grain	Very fine sand	Very fine sandstone
1/16 mm.		
Silt particle	Silt	Siltstone
1/256 mm.		
Clay particle	Clay	Claystone

4.7.2. Effect on ablation

The fact that supraglacial debris can both decrease or increase the melt rate of the ice underneath is well known (Nicholson & Benn 2013). Since larger parts of the Tiefenglacier's tongue are covered with debris, it is reasonable to assume that it has a significant effect on the melt rate of the ice and thus the tongue's overall dynamics.

In order to study the effect supraglacial debris has on the ice melt, debris thickness and ablation measurement data from the field reports was collected and summarized. The debris thickness measurements conducted during the field visit in October 2017 were also added, as well as information about grain size, rounding and a brief description of the measurement site. Subsequently, plots were generated showing the relation between debris thickness and surface ice melt. These relations could only be visualized if information regarding both the debris thickness and surface melt was collected over a span of a few days at the same locations, i.e. by the same group. The data points in these plots were colored according to the location on the glacier tongue where they were measured. The colorization provides more insight into the spatial variability of the effect the debris has on the surface melt.

Since there was a small amount of data from only three groups available including both debris thickness and surface melt, additional plots featuring the relation between debris thickness and surface elevation changes were generated. The difference between surface ice melt and surface elevation change is that the former describes the melt at the surface of the glacier ice, whereas the latter refers to a change in elevation of the glacier surface, which is not necessarily caused by surface ice melt. It is further important to mention that contrary to the surface melt measurements, which were conducted within a few days at a time on the tongue itself, the surface elevation changes were calculated using the DSMs in ArcMap with at least a year between measurements. The resulting plots showing the relation between debris thickness and surface melt or debris thickness and surface elevation change can therefore not be directly compared. However, it is possible to compare the debris thickness and surface melt data collected by different groups in different years in a single plot. For this, the total surface melt measured during the excursions was first calculated into a rate of cm/d for each location. In a next step, the calculated rates are divided by the average daily melt rate at locations without any debris. The resulting plot describes the relation between the debris thickness and the ablation relative to a debris-free surface.

4.8. Ice flow velocity

The fast retreat of the Tiefenglacier is coupled with large losses of ice mass due to the change of environmental and climatic factors. Often, such drastic changes in a glacier’s volume go hand in hand with a deceleration of its ice flow and, eventually, may lead to the complete stagnation of the ice masses (Benn et al. 2012, Thompson et al. 2016).

According to Oberli 2017, the tongue of the Tiefenglacier, which was disconnected from its accumulation area in the summer of 2017, is now dead-ice, meaning its flowing motion has come to a stop. This statement can be supported with the facts that the accumulation area can no longer feed the tongue with new ice, and that the surface gradient of the tongue is rather small, which favors stagnation (Thompson et al. 2016). However, no conclusive measurements have been undertaken so far, and considering the size of the remaining tongue, the ice may still be in motion, albeit very slowly.

To determine the flow velocity of the ice during the three previous years leading up to the disconnection of the tongue, the orthophotos were used to track and quantify the movements of boulders present on the ice surface. The distance the boulders travel on the ice within a known time period allows to draw conclusions as to how fast the underlying ice is moving. A total of eleven boulders were selected under the condition that they are visible in all four orthophotos and are unambiguously identifiable. Larger rocks and boulders tend to form glacier tables and over time slide off them, causing movements which cannot be explained by the ice flow alone. Therefore, the visible surface of each tracked boulder was calculated in ArcMap and compared to its distance traveled, to determine whether the rock size affects their movements as well. Furthermore, the location of the boulders on the tongue might influence their movement velocities as well, since the termini of glaciers usually show lower flowing speeds than the remaining glacier (Benn et al. 2012). Thus, the distance from each boulder to the glacier terminus was measured and subsequently compared to its movement velocity.

5. Results

In the following, the results obtained during this study are described and illustrated. The generated DSMs and orthophotos are briefly presented, followed by the accuracy assessment to determine their usability. Four fully mapped orthophotos of the glacier tongue are shown including explanations regarding the chosen surface types. The results of the elevation changes are divided into the analyses of the difference images on the one hand and glacial features on the other hand, in which five individual features are described in more detail. Further, the calculation of the average ice flow velocity based on the tracking of supraglacial rocks is presented. A summary of relevant GPR data collected by students who attended the course GEO 411 is added as their findings are brought into the context of the tongue's disintegration in the Discussion.

5.1. UAV images

5.1.1. Digital surface models

The extents of the generated DSMs vary greatly because of the different flight paths of the UAVs. The DSM of July 2014, for example, covers quite a large part of the glacier forefield, but only about half of the Tiefenglacier's tongue. Due to its limited extent, no calculations involving the upper half of the tongue in July 2014 could be conducted.

A first visual evaluation of the DSMs concluded that all models seem to have plausible elevation values, except for the one of July 2017. Although it cannot be seen at first glance, the entire model is convex in shape, meaning that the values at the center of the tongue are too low, and the edges of the model are excessively elevated. Any difference image generated using the DSM of July 2017 and another DSM, however, clearly shows its convex shape (see Chapter 5.2.3. for more details). This flawed geometry can be attributed to the use of a different UAV in that year, which seems to have acquired images in a way that cannot be correctly processed in Agisoft PhotoScan.

An issue occurring in all DSMs is the reduced accuracy around the edges of the models. In these areas, the overlap of the images is rather small compared to the centers of the models, which leads to unrealistic elevation values. Further, the GCPs used as reference points for the processing of the images are exclusively placed around the glacier tongue in stable terrain. This might produce larger errors in the elevation values on the tongue itself, since the GCPs should ideally be distributed equally over the entire area. The accuracy assessment in Chapter 5.2. provides more insight into the quality and usability of the DSMs.

The cell sizes of all DSMs before and after the resampling are given in Table 6. All DSMs can be found in Appendix 10.2.

Table 6: Cell sizes of the DSMs before (top) and after (bottom) resampling.

	Jul 2014	**Jul 2015**	**Jul 2016**	**Jul 2017**	**Oct 2017**
X cell size [cm]	29.90	43.30	42.80	12.70	44.70
Y cell size [cm]	29.90	43.30	42.80	12.70	44.70
X cell size [cm]	44.70	44.70	44.70	44.70	44.70
Y cell size [cm]	44.70	44.70	44.70	44.70	44.70

5.1.2. Orthophotos

All generated orthophotos are generally of good quality and can be used for further analysis. Their spatial resolution spans from 2.5 x 2.5 cm (July 2017) to 11.77 x 11.77 cm (October 2017), which is high enough to recognize relevant details (Table 7). However, there are several aspects affecting their quality that need to be considered. Firstly, parts of the edges of the orthophotos are visibly blurred or distorted. This can again be attributed to the reduced number of overlapping images around the edges of the models, which leads to the generation of less accurate surfaces during the processing with Agisoft PhotoScan. Secondly, there are fragments in the centers of the images which appear to be blurred to some extent as well, despite high image overlap. The cause for this might be that some of the acquired images by the UAV are blurred in the first place, due to unstable flight paths during the acquisition. Thirdly, clouds obscuring the view are present in the orthophoto of July 2016. The orthophoto of October 2017 is shown in Fig. 22; the remaining orthophotos can be found in Appendix 10.3.

Table 7: Cell sizes of the produced orthophotos.

	Jul 2014	**Jul 2015**	**Jul 2016**	**Jul 2017**	**Oct 2017**
X cell size [cm]	5.13	11.15	11.13	2.50	11.77
Y cell size [cm]	5.13	11.15	11.13	2.50	11.77

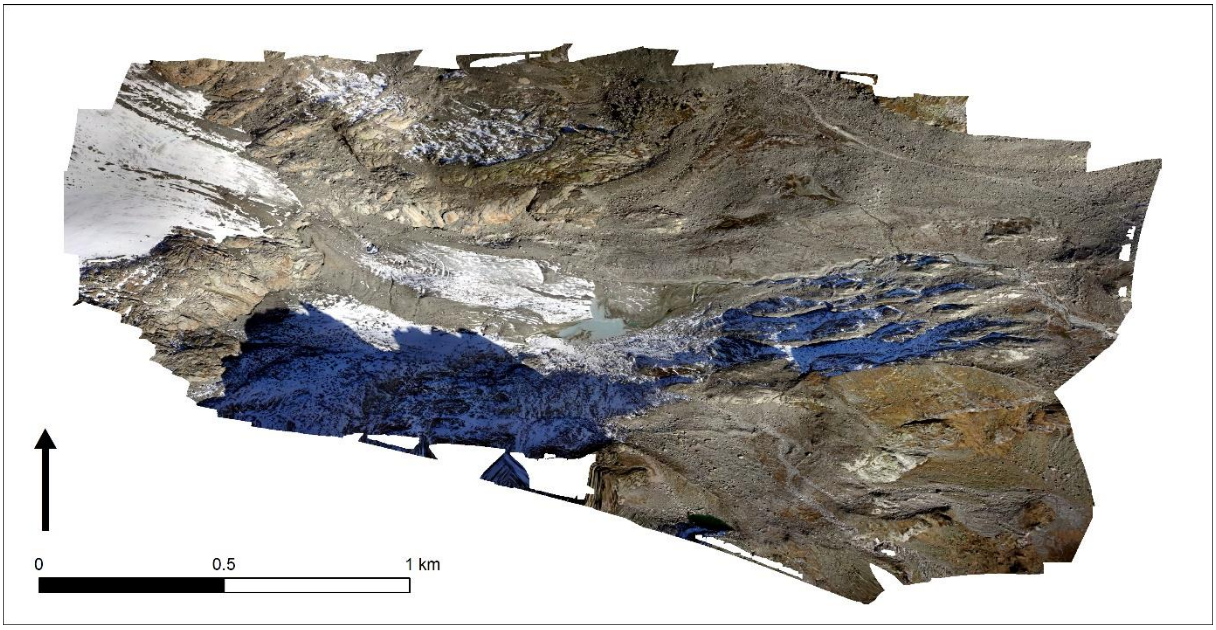

Fig. 22: The orthophoto of October 2017.

5.1.3. Hillshades

The hillshade of October 2017 is shown in Fig. 23, whereas the remaining can be found in Appendix 10.4. They are suitable for recognizing details of glacial features, as the absence of real color as well as the artificial lighting highlight their structures.

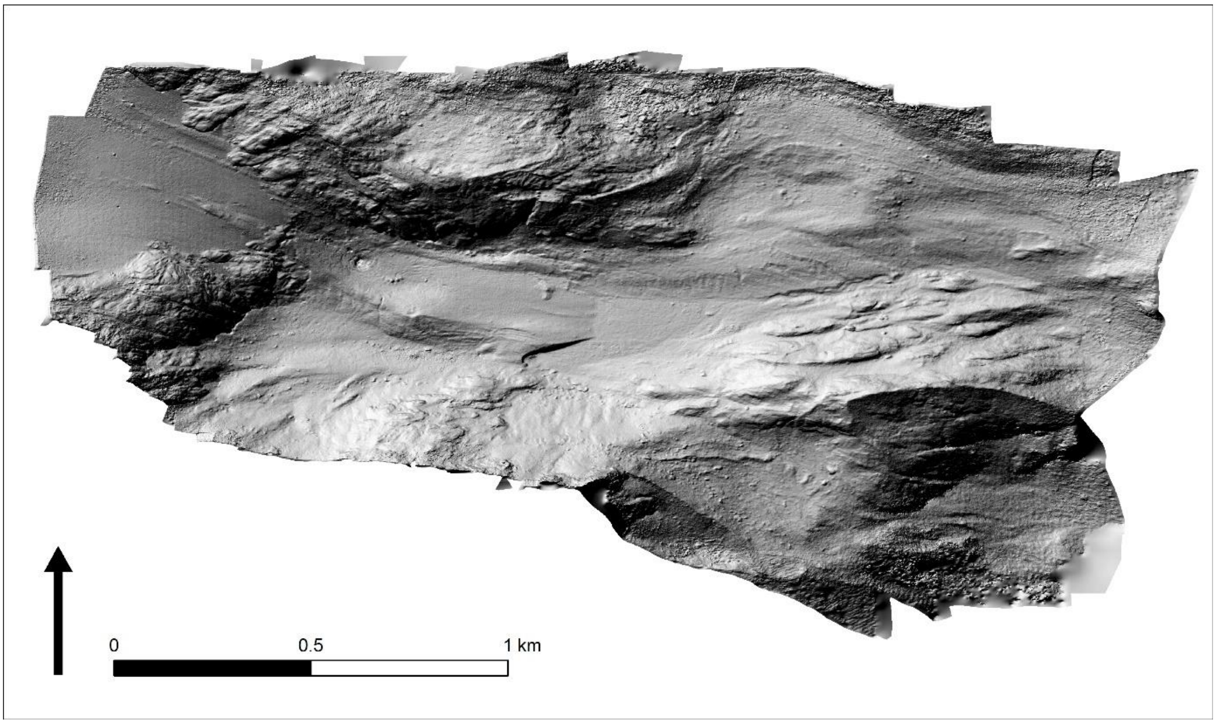

Fig. 23: Hillshade of the Tiefenglacier in October 2017.

5.2. Accuracy assessment

In the following, the results of the accuracy assessment of both the DSMs and the difference images is presented. It provides insights into the horizontal and vertical accuracies and allows to determine whether further steps to improve the accuracy are necessary.

5.2.1. Co-registration

Table 8 summarizes the calculated shifts of the DSMs between July 2014 and July 2016 relative to the reference DSM of October 2017. The shifts are expressed in the x, y and z (=dh) dimensions.

Table 8: Calculated shifts of the DSMs relative to the reference DSM of October 2017.

DSM	**x-shift [m]**	**y-shift [m]**	**z-shift [m]**
Jul 2014	0.5	-1	-0.6
Jul 2015	0.4	0	-0.3
Jul 2016	-0.3	1	-0.5

The systematic shifts range between -0.3 m (July 2016) and 0.5 m (July 2014) for the x-dimension, between 0 m (July 2015) and -1 / 1 m (July 2014, July 2016) for the y-dimension and between -0.3 m

(July 2015) and -0.6 m (July 2014) for the z-dimension. In order to correct the displacement of the individual DSMs relative to the reference DSM, they need to be shifted by the value of these parameters in the opposite direction (e.g. x = -0.5, y = 1, z = 0.6 for the DSM of July 2014). However, given that the cell sizes of the resampled DSMs are 44.7 cm, a horizontal shift of the DSMs is unnecessary, as it would not improve their relative position significantly.

5.2.2. Quantitative accuracy assessment

The level of recognizable detail describes the resolution of a DSM in which details, such as supraglacial features, can be identified with a reasonable degree of certainty. The horizontal resolutions of the DSMs are determined by the camera used for the acquisition of the images as well as the post-processing in Agisoft PhotoScan. The resampling of the DSMs between July 2014 and July 2016 to the cell size of the DSM of October 2017 ensures that all models have a horizontal resolution of 44.7 x 44.7 cm, which also describes the horizontal level of recognizable detail. In the vertical dimensions, systematic and stochastic uncertainty values are used to express the level of recognizable detail.

In the following, the accuracy is expressed as the systematic bias as well as the stochastic uncertainty between each DSM and the reference DSM of October 2017. The systematic bias is defined by the mean elevation difference MED and the absolute mean error AME, whereas the stochastic uncertainty is defined by the standard deviation STD and the standard error SE. All values are summarized in Table 9.

Table 9: Quantitative accuracy assessment of all produced DSMs including the number of GCPs, the mean elevation difference MED, the absolute mean error AME, the standard deviation STD and the standard error SE.

DSM	Number of GCPs (n)	MED [m]	AME [m]	STD [m]	SE [m]
Jul 2014	10	0.05	0.18	0.20	0.06
Jul 2015	20	-0.26	0.28	0.23	0.05
Jul 2016	10	0.31	0.32	0.18	0.06
Oct 2017	19	-	-	-	-

The MED ranges from a minimum of 0.05 m (July 2014) to a maximum of 0.31 m (July 2016). The AME, however, shows higher values, since positive and negative biases do not cancel each other out, ranging from 0.18 m (July 2014) to 0.32 m (July 2016). The stochastic uncertainty values show minimum values of 0.18 m (July 2016) and 0.05 m (July 2015), and maximum values of 0.23 m (July 2015) and 0.06 m (July 2014, July 2016) for the standard deviation and the standard error, respectively.

The uncertainty values are well below 0.5 m, which suggests that the DSMs represent the topography with a high degree of accuracy. However, the stable terrain used for the calculation of the accuracy might have experienced slight elevation changes through rockfall. Further, the terrain has a small extent and is exclusively located in the glacier forefield, as it is the only stable area visible in all DSMs. Any distortion or warping of the DSMs, which might affect their accuracies in the upper part of the glacier tongue, are not further discussed.

5.2.3. Difference images

In the following, the accuracy measures for all difference images are presented (Table 10). For each image, the lower number of GCPs from the DSMs was chosen for the calculation of the standard error.

Table 10: Accuracy measures for all difference images, including number of GCPs, MED, AME, STD and SE.

Difference image	**Number of GCPs (n)**	**MED [m]**	**AME [m]**	**STD [m]**	**SE [m]**
Jul 14 – Jul 15	10	0.30	0.39	0.37	0.12
Jul 14 – Jul 16	10	-0.26	0.31	0.28	0.09
Jul 14 – Oct 17	10	0.05	0.18	0.20	0.06
Jul 15 – Jul 16	10	-0.57	0.57	0.23	0.07
Jul 15 – Oct 17	19	-0.25	0.26	0.22	0.05
Jul 16 – Oct 17	10	0.31	0.32	0.18	0.06

The MED ranges from 0.05 m (Jul 14–Oct 17) to -0.57 m (Jul 2015–Jul 2016), whereas the AME ranges from 0.18 m (Jul 14–Oct 17) to 0.57 m (Jul 15–Jul 16). The stochastic uncertainty is expressed as the STD and the SE, which show a minimum of 0.18 m (Jul 16–Oct 17) and 0.05 m (Jul 15–Oct 17, Jul 16–Oct 17) and a maximum of 0.37 m (Jul 14–Jul 15) and 0.12 m (Jul 14–Jul 15), respectively. Similar to the values of the accuracy assessment of the DSMs, these values suggest high quality difference images with a detailed representation of the topography. It can be assumed, therefore, that details larger than approx. 0.6 m in the vertical dimension can be recognized in all images. All difference images are deemed suitable for further analysis and no additional corrections are needed.

5.3. Mapping

Figs. 24–27 show the fully mapped orthophotos of the glacier tongue from the years 2014-2017. The different shades of gray refer to varying degrees of continuity and grain sizes of the supraglacial debris. Light gray stands for thin, discontinuous debris covers with sand, gravel and small boulders, whereas the slightly darker shade of gray refers to continuous debris covers with grain sizes ranging from sand to very large boulders. Dark gray was specifically chosen for the sediment hill, as it mainly consists of a very thick debris cover with small to medium grain sizes, and therefore does not fit into the previous two categories.

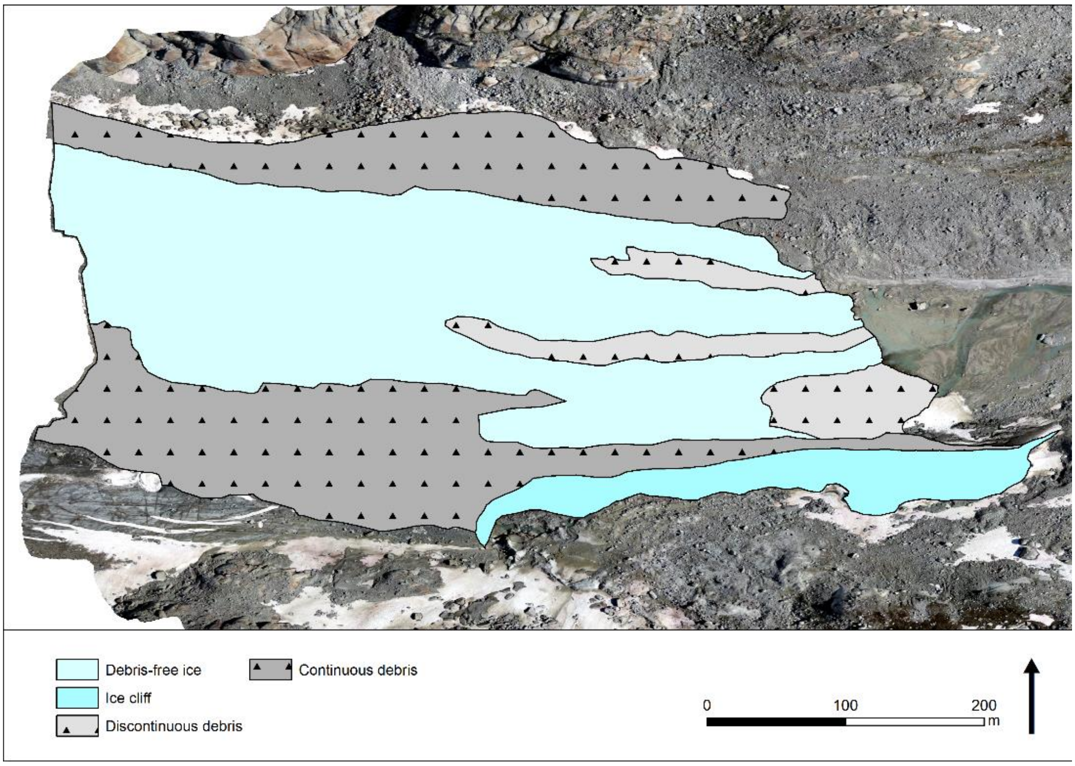

Fig. 24: Mapped orthophoto of the glacier tongue in July 2014.

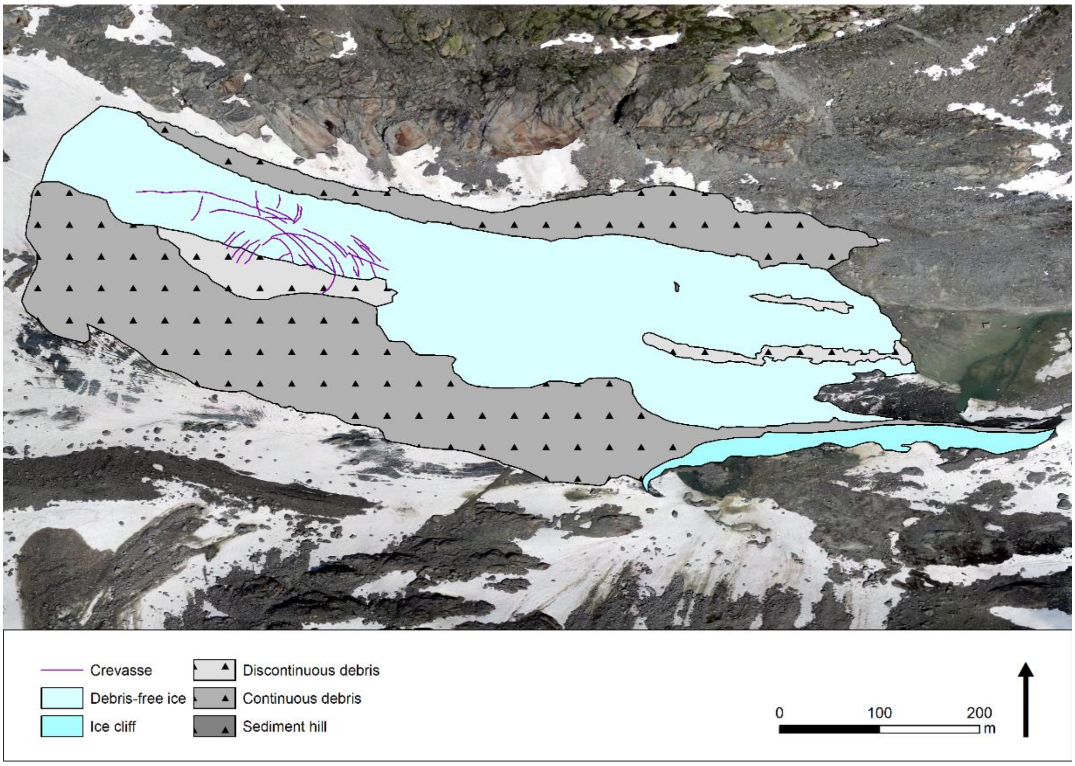

Fig. 25: Mapped orthophoto of the glacier tongue in July 2015.

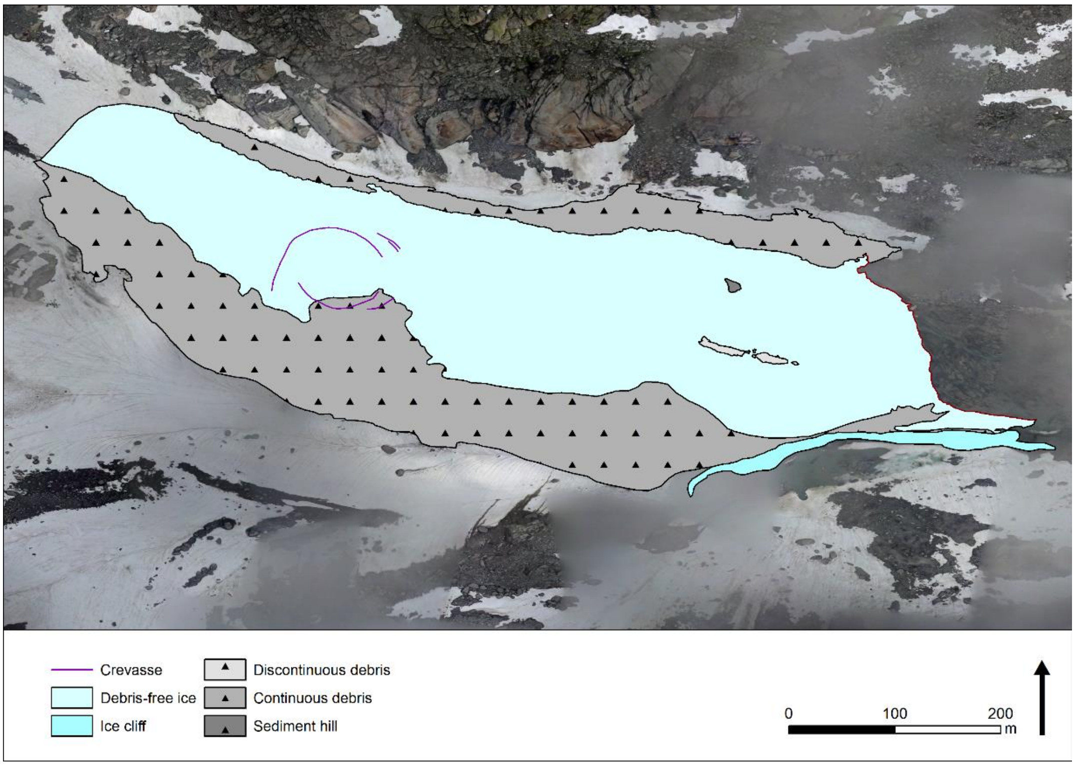

Fig. 26: Mapped orthophoto of the glacier tongue in July 2016.

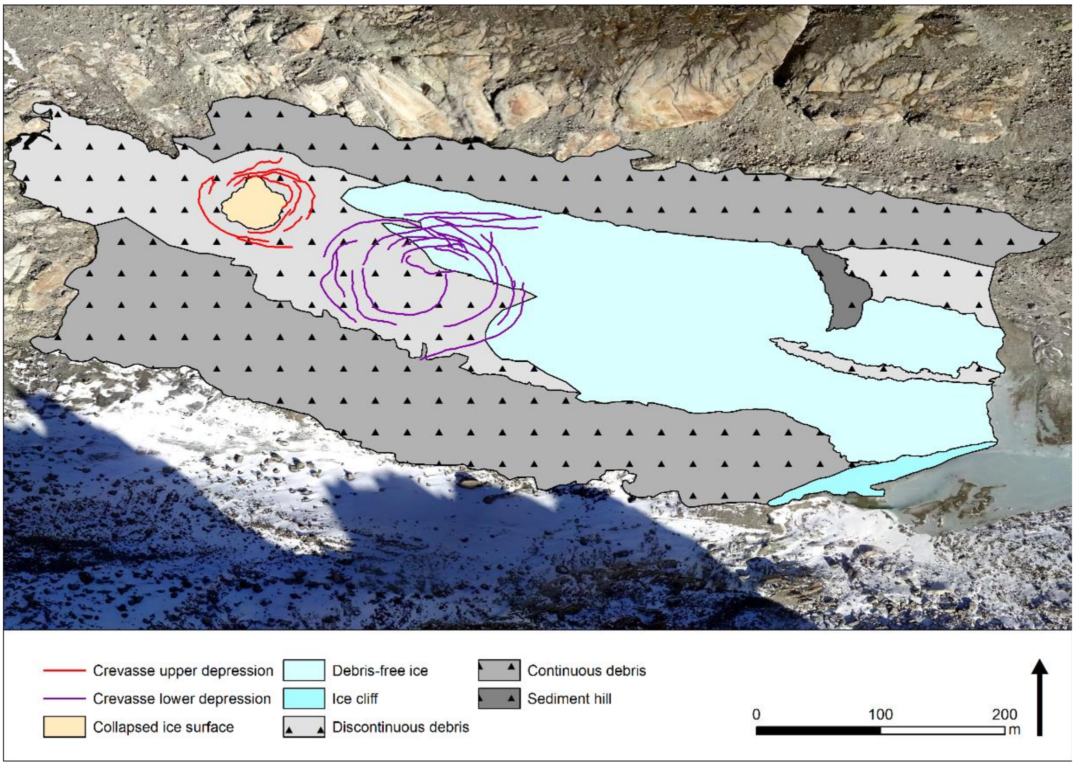

Fig. 27: Mapped orthophoto of the glacier tongue in October 2017.

The category *Ice* describes largely debris-free ice surfaces and *Ice cliff* shows the approximate extent of the ice cliff located at the lower end of the medial moraine. The presence of snow in the orthophotos of July 2015 and July 2016 made it difficult to differentiate between debris-covered and debris-free surfaces. In case of doubt, the surface type *Ice* was chosen. All visible crevasses in the orthophoto of October 2017 in the upper half of the tongue have been mapped as well in red and purple, indicating two separate depressions. It could not be determined whether the crevasses visible in the orthophotos of July 2015 and 2016 belonged to the upper or lower subsidence, as there is a snow cover obscuring the view. Lastly, the hole caused by the collapse of the glacier surface in the orthophoto of October 2017 is indicated as well.

It needs to be emphasized that these maps are meant to give a broad overview of the tongue's features and surface cover. The details should not be given too much attention, as the process of drawing the borders of glacial features is subject to a certain degree of uncertainty and subjectivity.

5.4. Elevation changes

All elevation changes of the ice surface are expressed in centimeters or meters and are not converted into water equivalent, as the focus lies on the dynamics of the ice rather than the glacier's mass balance. Further, some measurements are expressed in ranges rather than exact values, as most glacial features have fluent transitions to their surroundings and the choice of where the measurements should be conducted is rather subjective.

5.4.1. Difference images

In the following, the difference images created by subtracting different DSMs from another are presented. More specifically, two images showing the elevation difference of one summer (Jul 2014–Jul 2015, Jul 2015–Jul 2016), as well as an image featuring two summers (Jul 2016–Oct 2017) are shown and briefly discussed. Further, a difference image depicting the elevation changes between the oldest available DSM (Jul 2014) and the newest one (October 2017) is added as an overview of the development of the glacial features. Additionally, a difference image was created using the DSMs of July 2016 and July 2017 to explain and visualize in more detail why the DSM of July 2017 is not suitable for further use. Five more difference images can be found in Appendix (10.5.), which are not further discussed in this chapter.

The orthophotos used as backgrounds in the following images are the ones produced on the same date as the newer DSM. The extents of the DSMs have been clipped to focus the attention on the glacier tongue, thus the partially sharp edges. Although there are no positive values in the legends, there are small areas in every generated difference image which show increases in elevation. However, these areas only exist in very steep terrain, near the edges of the DSMs or in the glacier forefield. The latter is the result of either the deposition of fine debris transported by the melt water or the accumulation of rockfall from higher elevations. These positive elevation changes are usually in the range of a few meters. The ones occurring in steep non-glaciated terrain or near the edges of the DSMs are the results of minor horizontal offsets between the DSMs, or of Agisoft trying to calculate the elevation values with not enough overlapping images. As none of the studied glacial features show any positive elevation changes, zero was chosen to be the highest elevation change value in the images. Note that the value zero is not displayed by the color white, but by full transparency.

5.4.1.1. July 2014 – July 2015

The elevation changes between July 2014 and July 2015 seem to be roughly uniform across the lower half of the tongue at around 3-5 m, except for the ice cliff in the South-East and a few minor spots (Fig. 29). The ice cliff stands out in every difference image, as the vertical elevation change in this region is very high. This can be explained by the south-eastern exposition of the cliff, which leads to a very steep incidence angle of the sun rays, causing accelerated melting of the ice.

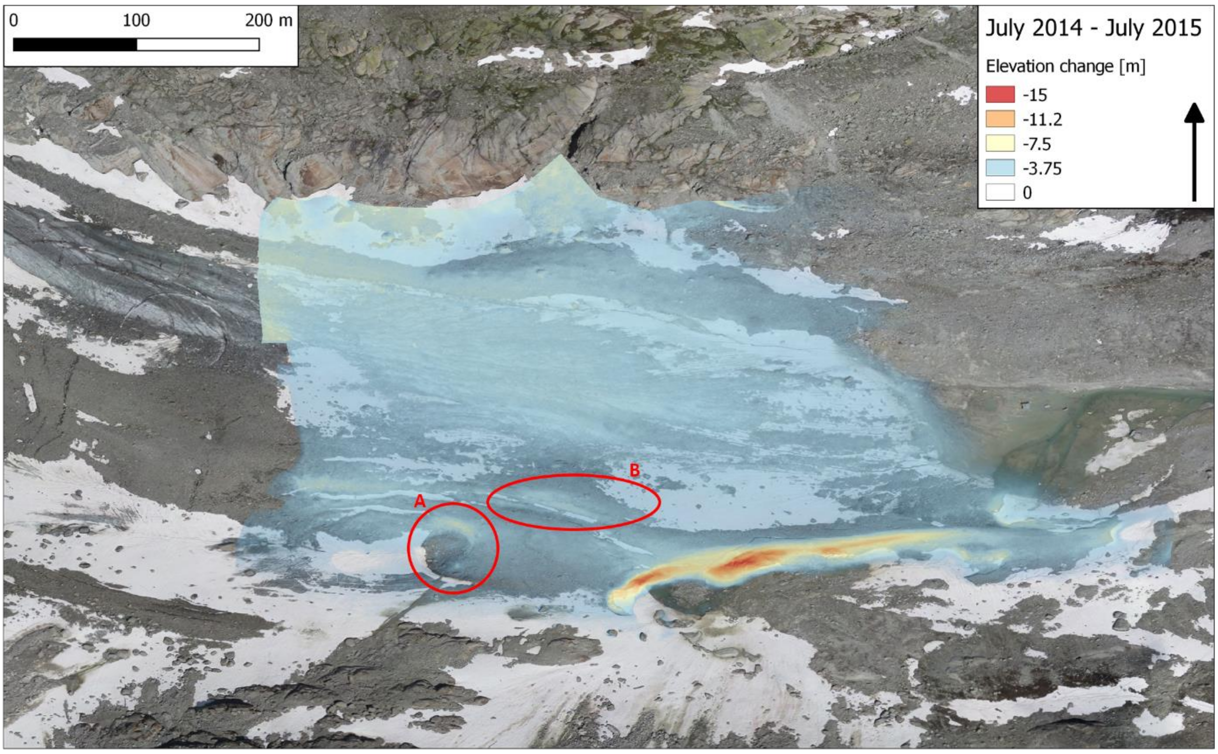

Fig. 27: Elevation differences calculated on the lower glacier tongue between July 2014 and July 2015.

About 100 m farther upstream of the large ice cliff in the middle of the medial moraine, a smaller ice cliff is present, identifiable by the slightly larger elevation change compared to its surroundings (Area A). This cliff does not show elevation changes as large as the one farther to the East, most likely because of its considerable smaller size in both the vertical and horizontal dimensions as well as its exposition towards South-West rather than South-East. Further, the smaller cliff is slightly covered by debris, indicating that it is not steep enough for debris to immediately slide off its surface.

On the lower medial moraine, there are two distinct bands of increased downwasting, visible as yellow stripes (Area B). These are the result of longitudinal crevasses forming and deepening in this area. Snow trapped in these crevasses lead to the long visible white stripes in the orthophoto.

The lower lateral moraine shows smaller elevation changes than the upper lateral moraine. The area of the upper lateral moraine near the edge of the DSM needs to be interpreted with caution, though, as the accuracy of the DSM is probably reduced near the edges. The debris-covered surfaces to the North of the medial moraine have experienced slightly less downwasting than the wide debris-free surface to the North. As these areas are very close to the moraine, it can be assumed that the debris-cover is rather thick, thereby insulating the underlying ice.

5.4.1.2. July 2015 – July 2016

This image shows well how the upper half of the tongue experienced considerably more downwasting than the lower half (Fig. 30). The largest elevation changes can be found in Areas C and D, with up to approx. -11 m. These are the areas where the concentric crevasses widen and deepen over time and eventually lead to the collapse of the glacier surface. They are already visible in the orthophoto of July 2015 but have been covered by a layer of snow in July 2016. The upper part of Area C is also the zone where the tongue loses its contact with the accumulation zone in the summer of 2017.

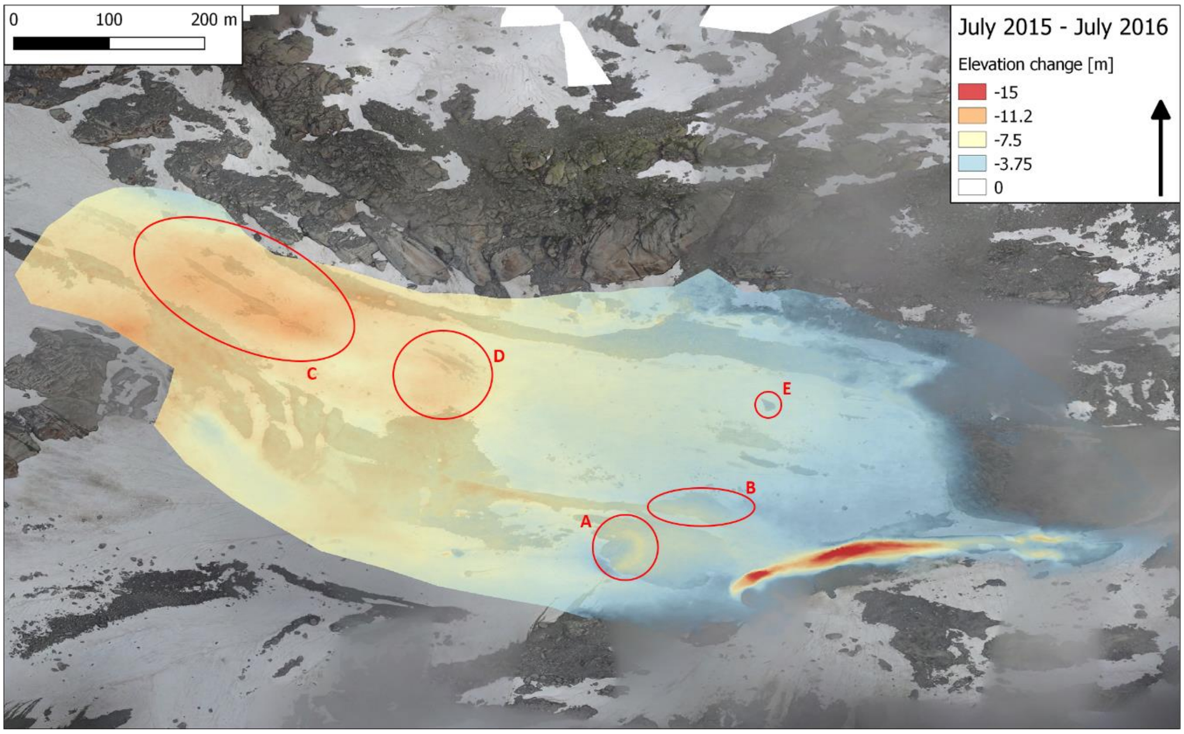

Fig. 28: Elevation differences of the glacier tongue between July 2015 and July 2016.

The ice cliff at the lower medial moraine is, again, very noticeable because of the large elevation changes. Its west-east extent appears to have been slightly reduced and the two Areas A and B show even larger elevation changes than the year before. The smaller ice cliff, which was already present in the previous year, has grown and is now in the shape of a semicircle, having ice surfaces exposed to the

South, West and North. A bit to the North there is a small patch of debris, which shows slightly less downwasting than its surroundings (Area E). This is the first sign of a sediment hill, which will gain substantial height relative to the surrounding glacier surface in the following years.

5.4.1.3. July 2016 – October 2017

It is important to note that the difference image from July 2016 to October 2017 shows the effect of two summers on the glacier tongue, instead of just one (Fig. 31).

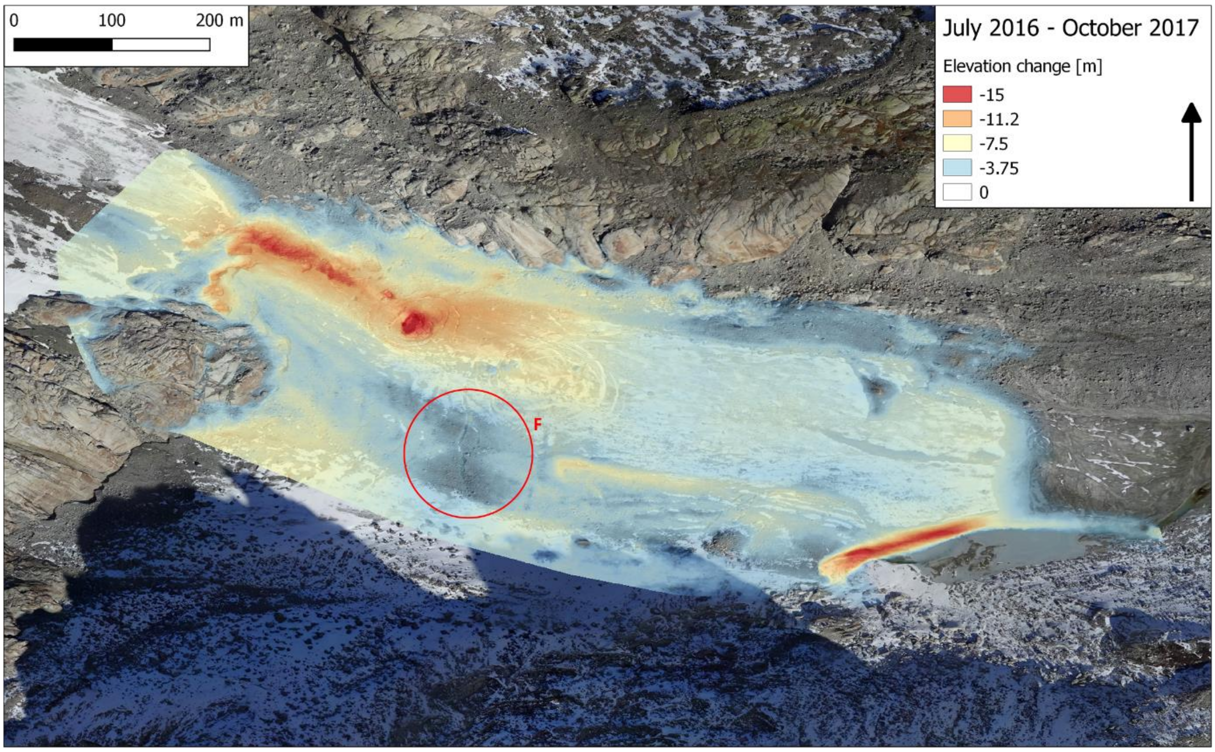

Fig. 29: Elevation differences of the glacier tongue between July 2016 and October 2017.

One of the more conspicuous developments on the tongue is the collapse of the ice surface in the center of the upper depression, visible as a red spot in the image. The collapse is accompanied by large elevation changes in its surroundings, especially where the connection to the upper part of the glacier used to be. The ice in this area has completely melted away by the time the newer DSM was acquired, which uncovered the bedrock underneath.

The medial moraine is characterized by two adjacent areas, which seem to have experienced smaller elevation changes than the rest of the moraine (Area F). Farther downstream, a longitudinal yellow stripe suggests that the crevasse, whose formation can already be observed in the previous difference image, further deepened. The smaller ice cliff on the lower medial moraine can barely be recognized anymore, as the exposed ice surfaces have probably receded to the point where they are too even for debris to slide off. The large ice cliff, however, still shows great elevation changes of up to -15.6 ± 0.18 m and has further lost some of its West-East extent. Due to the extreme melting rates on its south-eastern exposed surface, the cliff slowly moves towards North-West, as more debris from the medial moraine slides off its surface. At the bottom of the cliff, the proglacial lake, that started to develop in the previous years, has grown significantly and reaches the northern end of the glacier terminus, near the end of the lateral moraine.

The sediment hill to the South of the lower lateral moraine, which was visible as a small patch the years before, has gained considerable volume and is now easily recognizable on the orthophoto. Its peak has not experienced any elevation change, meaning that the hill is stable as the tongue surrounding it melts away.

As already observed in the difference images of the previous years, the lower lateral moraine has experienced less downwasting than the upper half. The part of the moraine close to the sediment hill even seems to be almost stable, with elevation changes close to zero. The remaining lower half of the tongue, which consists of either debris-free or slightly debris-covered ice and no other notable features, shows a roughly uniform elevation loss of around -4 to -6 m.

5.4.1.4. July 2014 – October 2017

The scale of the elevation change for this difference image has been adjusted, as it includes four summers and therefore bigger changes (Fig. 32). Some of the features discussed above are more easily identifiable, as their developments are depicted over a much longer time span. For example, the extent of the large ice cliff at the time the orthophoto was acquired is limited to the red and dark orange areas near the lower medial moraine, but just over three years before it reached far into what is now the glacier forefield.

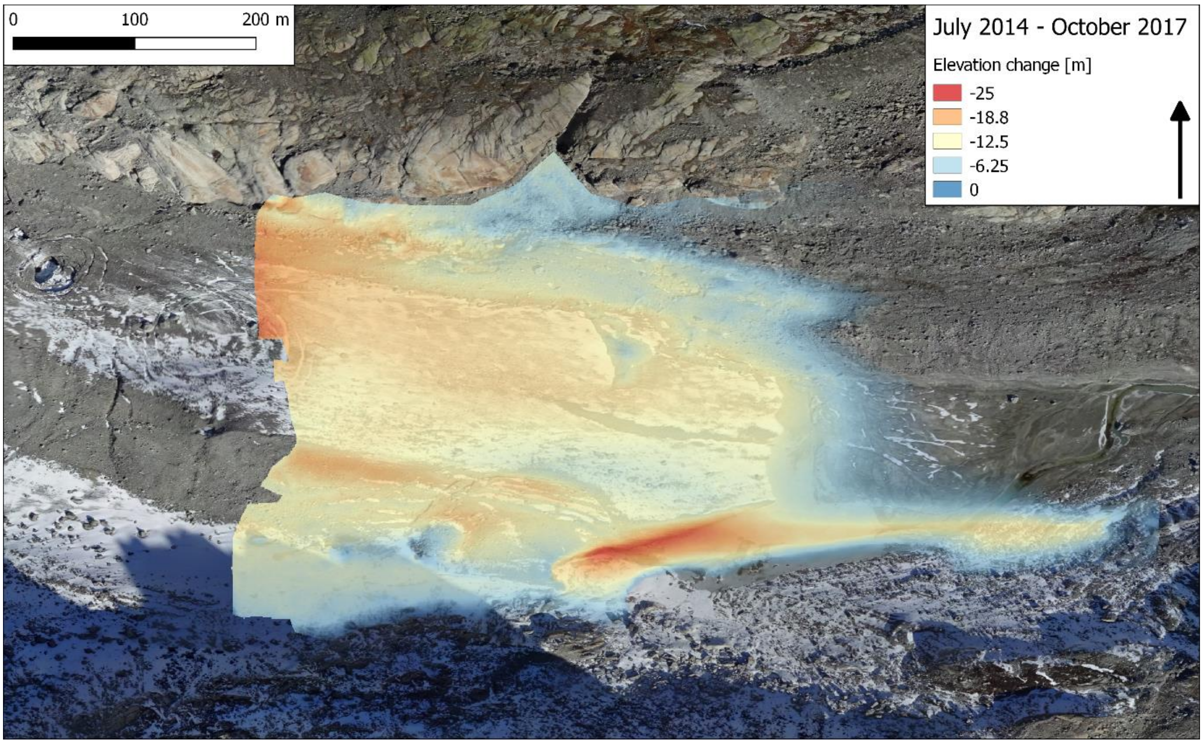

Fig. 30: Elevation differences of the glacier tongue during the entire observation period between July 2014 and October 2017.

The glacier terminus has receded approx. 90-100 m and is now enclosed by the proglacial lake. Excluding the ice cliff, the largest elevation changes can be found on the medial moraine, the upper part of the lateral moraine as well as the debris-free surface near the depressions. Noticeably low elevation changes are found in the small pit next to the smaller ice cliff, at a patch of ice North to the larger ice cliff, at the sediment hill and the entire lower end of the lateral moraine.

5.4.1.5. July 2016 – July 2017

The elevation change scale for this image was set to include positive values, as large parts of the image feature positive elevation changes (Fig. 33). According to this difference image, three quarters of the glacier tongue would have immensely gained elevation within just one year, whereas the uppermost quarter would have experienced downwasting. Clearly, these values are not plausible, as the glacier is stagnating, and such vast amounts of ice could not be transported in that time span. Further, the stable terrain surrounding the glacier tongue also features large elevation changes, which indicates that the DSM of July 2017 must have incorrect elevation values. In fact, this DSM is convex in shape, since the edges show negative values, whereas the center features positive values. Due to these unrealistic values, the DSM of July 2017 will not be used for any further analysis. The reason for this misshapen DSM is presumably the use of a different UAV for its acquisition. Apparently, Agisoft PhotoScan was not able to correctly process the images to produce a useful DSM.

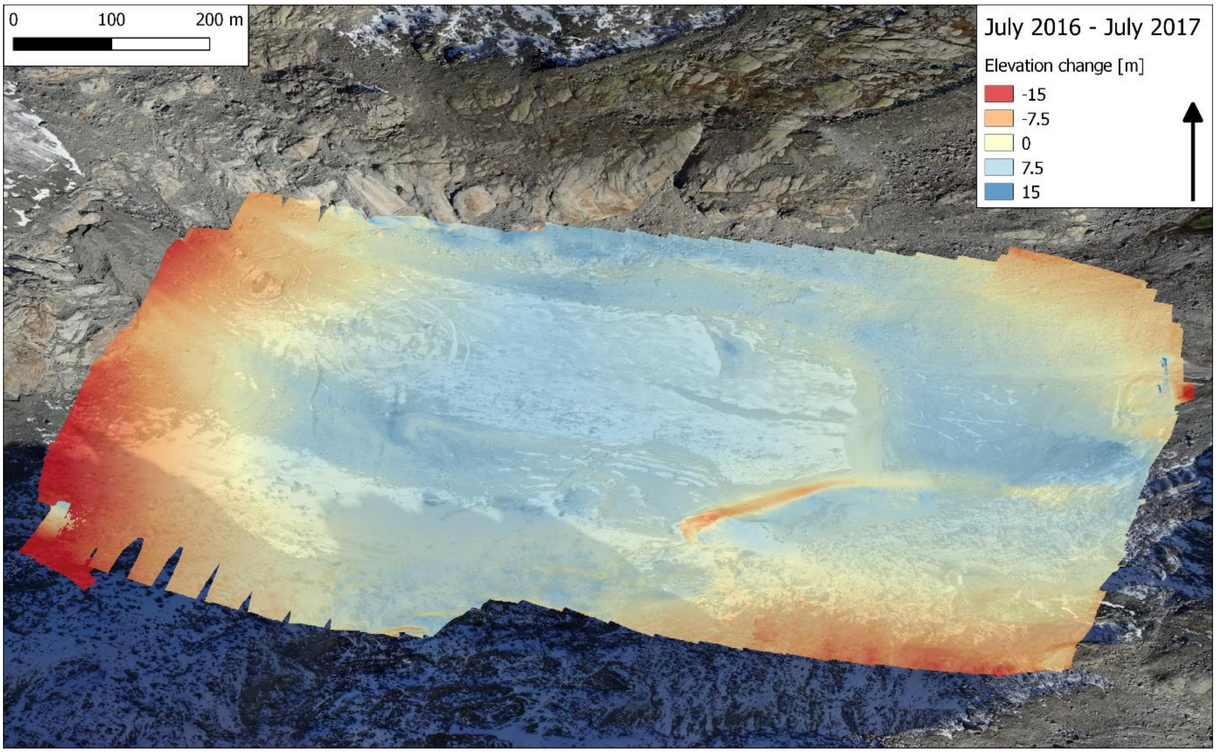

Fig. 31: Elevation differences of the glacier tongue between July 2016 and July 2017. The convex shape of the DSM of July 2017 produces unrealistic values in the difference images, even in stable terrain.

5.4.1.6. Upper/lower tongue

Fig. 34 shows the elevation change of the glacier tongue between July 2015 and October 2017 excluding the moraines and the ice cliff. The blue outlines indicate the extents of the upper and lower halves of the tongue. The fact that the upper half experienced considerably more downwasting than the lower half is easily visible and can be confirmed by the mean elevation changes in each half (Table 11). While the mean elevation change in the upper half is -16 ± 0.22 m, it is only -9.9 ± 0.22 m in the lower half. There is an even bigger difference between the minimum values, or the largest amount of elevation loss: -12.5 ± 0.22 m in the lower half and -30.3 ± 0.22 m in the upper half, which is almost 2.5 times the amount. The lower standard deviation in the lower half makes it evident that the elevation change is much more uniform than in the upper half. This can be explained by the fact that the region where the ice surface collapsed shows much higher elevation changes than the lower part of the upper half, which has similar values as the lower half of the tongue.

Table 11: Mean elevation differences, minimum values, maximum values and the standard deviations of the upper and lower glacier tongue.

Region	Min [m]	Max [m]	Range [m]	Mean [m]	STD
Upper tongue	-30.3	-10.0	20.3	-16.0	3.0
Lower tongue	-12.5	-4.3	8.2	-9.9	1.2

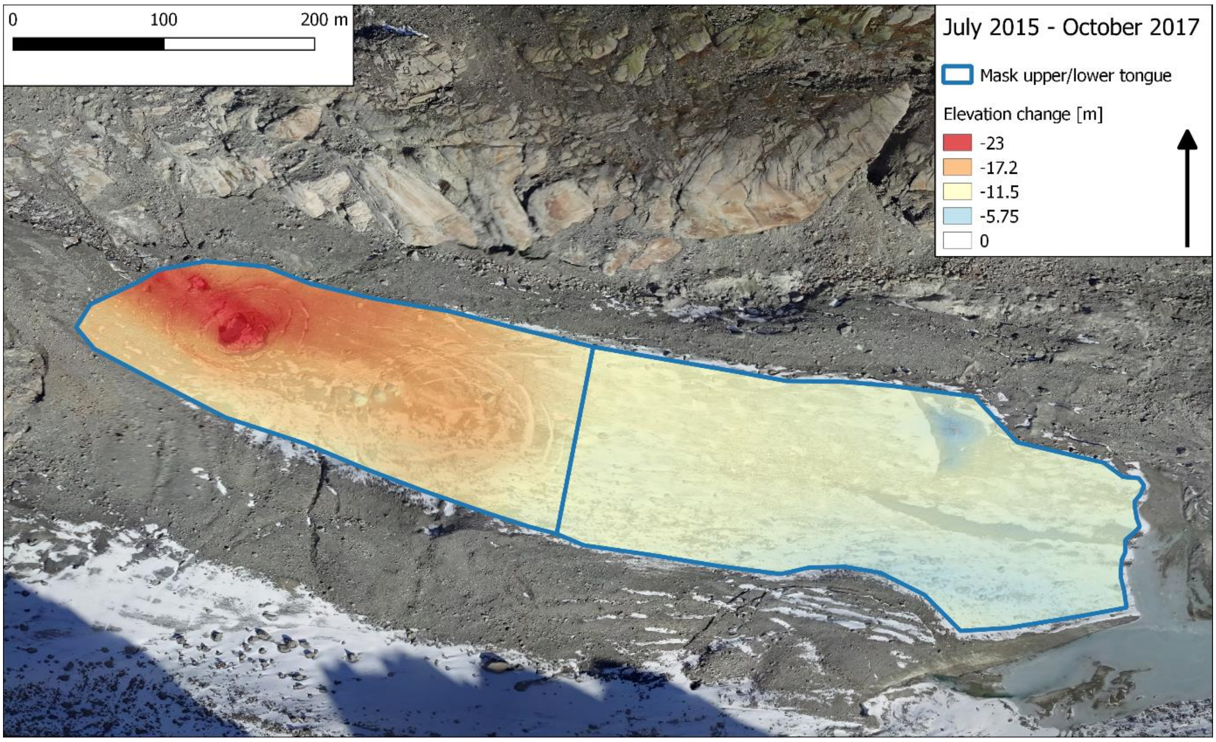

Fig. 32: Elevation differences on the upper and lower glacier tongue, excluding the moraines and the ice cliff.

5.4.2. Glacial features

In the following section, the elevation changes of individual glacial features are described in more detail. Profiles and point-based elevation differences are used to illustrate the features' temporal developments. Further, various plots as well as difference images and orthophotos are used to quantify their changes over the years.

5.4.2.1. Lateral moraine

A series of points distributed in longitudinal lines on the moraines were used to examine the variability of the elevation changes (Fig. 35). Figs. 36 and 37 show those changes for the points on the orographically right and left side, respectively. Each line stands for the elevation change of a single point, and the darker the line in the chart is, the farther downstream on the moraine it is located.

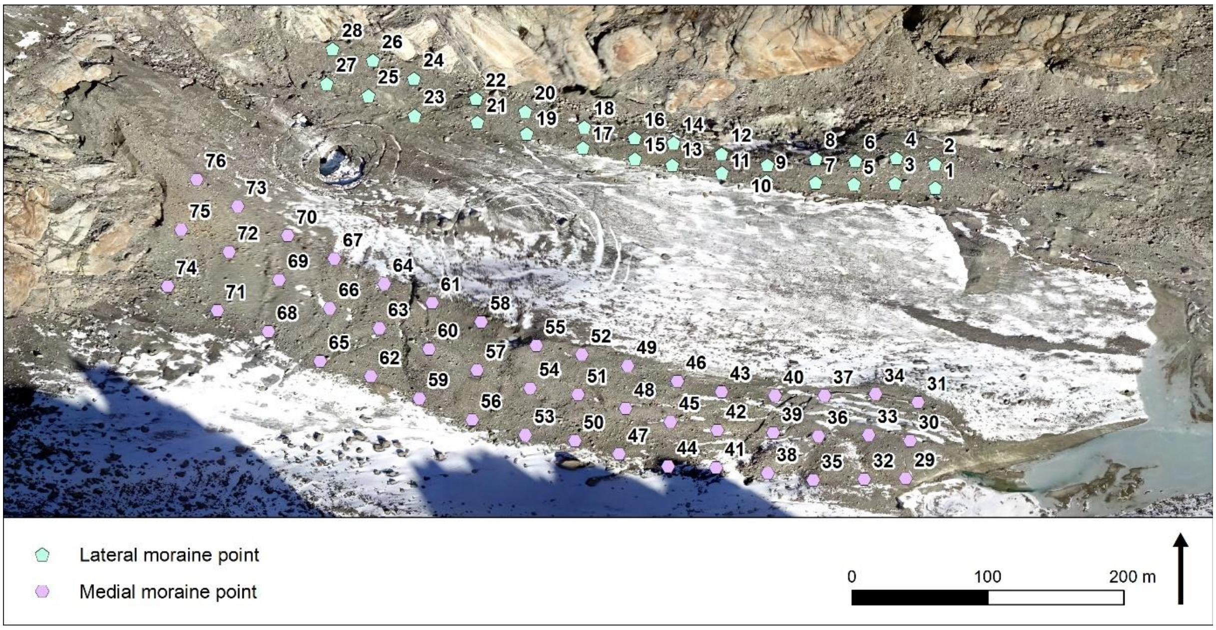

Fig. 33: Lateral and medial moraine points for the calculation of elevation differences.

It is clearly visible that the lines in both charts are almost perfectly sorted from dark to light, where the dark lines show the least amount of elevation change and the light ones show the most. This shows that the elevation change gradually increases from the lower end of the moraine to the upper end on both sides. The lowest point on the left side with the number 17 shows an elevation change of -6.7 ± 0.18 m between July 2015 and October 2017, while the highest point (43) shows a change of -15.1 ± 0.18 m. On the right side, the elevation changes range from -7.9 ± 0.18 m (point 16) to -18.5 ± 0.18 m (point 38). On average, the upper half of the moraine experienced a downwasting of -8.9 ± 0.18 m, whereas in the lower half it amounts to -15.2 ± 0.18 m. The downwasting rate seems to have slowed down between July 2016 and October 2017 for all points. However, no statements regarding the detailed development of these rates can be made, as only three data points for elevation are available for this time span.

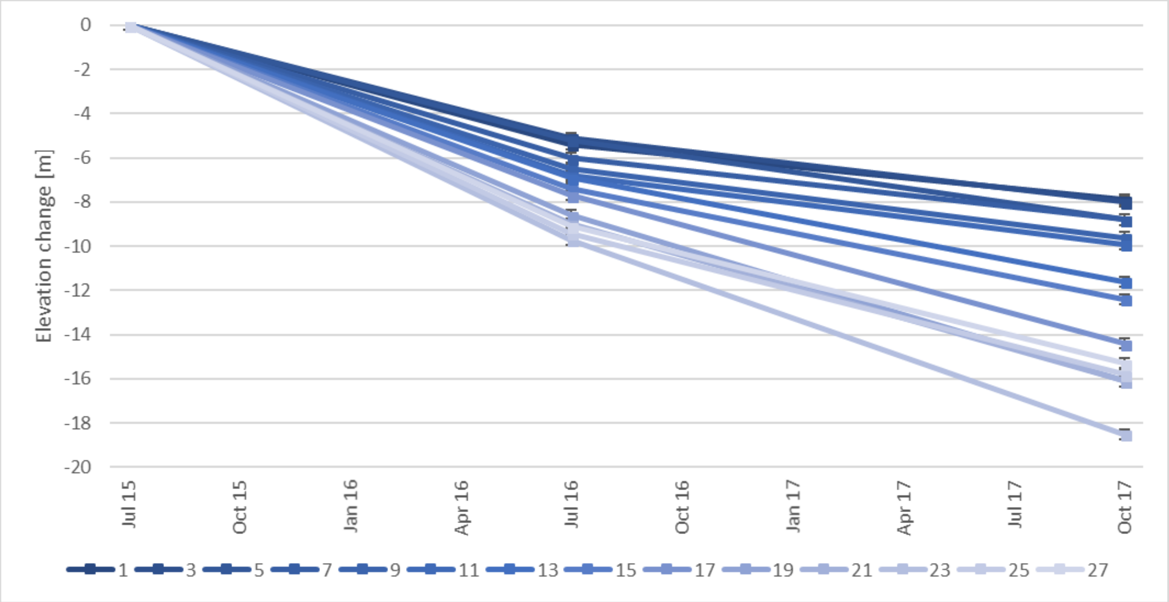

Fig. 34: Elevation changes for each point on the right side of the lateral moraine between July 2015 and October 2017.

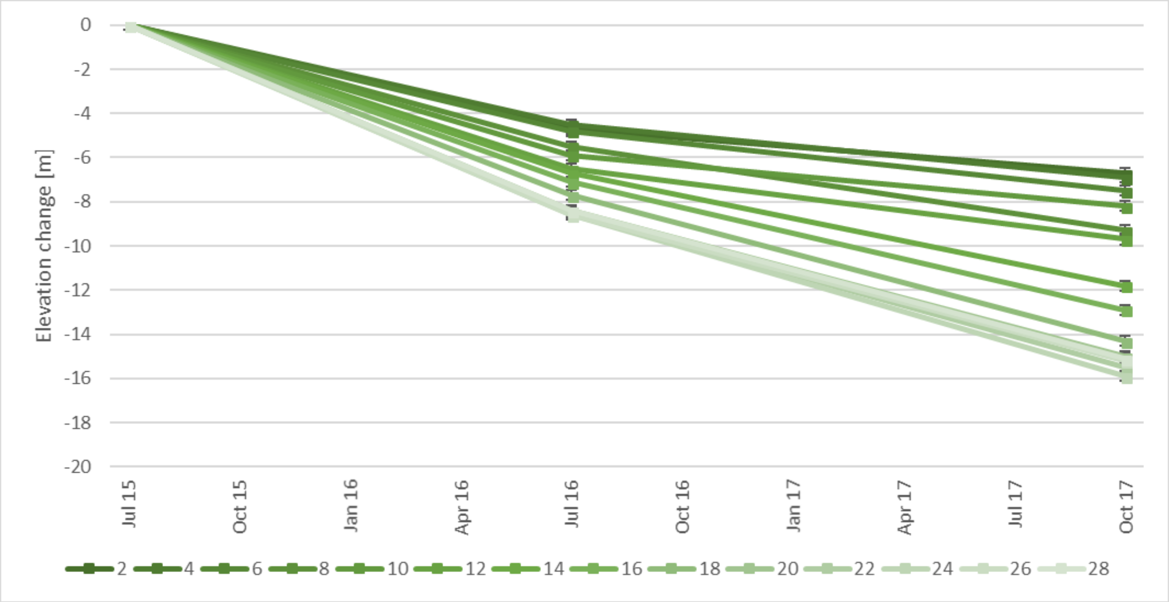

Fig. 35: Elevation changes for each point on the left side of the lateral moraine between July 2015 and October 2017.

5.4.2.2. Medial moraine

For the medial moraine, three lines consisting of individual points were created because of its wider width (Fig. 35). The results are illustrated as line charts in Figs. 38–40. On the right side of the moraine, the elevation changes gradually increase towards the upper end of the moraine as well, albeit not as clearly as on the lateral moraine. As already observed on the lateral moraine, the elevation loss slows down after July 2016. The changes range from -4.9 ± 0.18 m at point 9 to -13.6 ± 0.18 m at point 42. The only positive elevation change of 0.1 ± 0.18 m at point 9 lies within the error margin and might therefore be no elevation change at all. The lower and upper parts of the ridge of the medial moraine show smaller differences in elevation change than its right side, ranging from -9 ± 0.18 m to -13.3 ± 0.18 m. Also, the extent of the elevation change is less dependent on the location on the moraine, as shown by the poorer sorting of the shades of yellow in the chart. In quantitative terms, the upper and lower medial moraine experienced an average downwasting of -12.2 ± 0.18 m and -10.1 ± 0.18 m, respectively. The left side of the medial moraine shows the largest elevation changes, ranging from -9.2 ± 0.18 m at point 2 to -14.9 ± 0.18 m at point 47, and features the poorest sorting of the color shades. Interestingly, the poor sorting of these elevation changes mostly appeared between July 2016 and October 2017 for all three observed sides on the medial moraine. Between July 2015 and July 2016, the elevation changes still increased towards the upper part of the moraine.

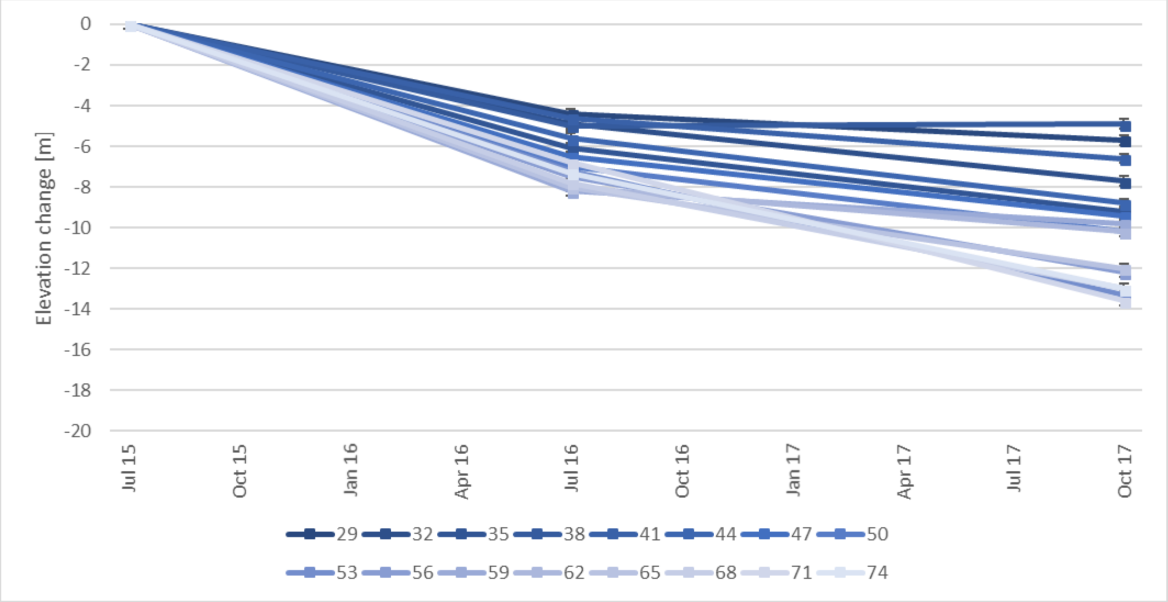

Fig. 36: Elevation changes for each point on the right side of the medial moraine between July 2015 and October 2017.

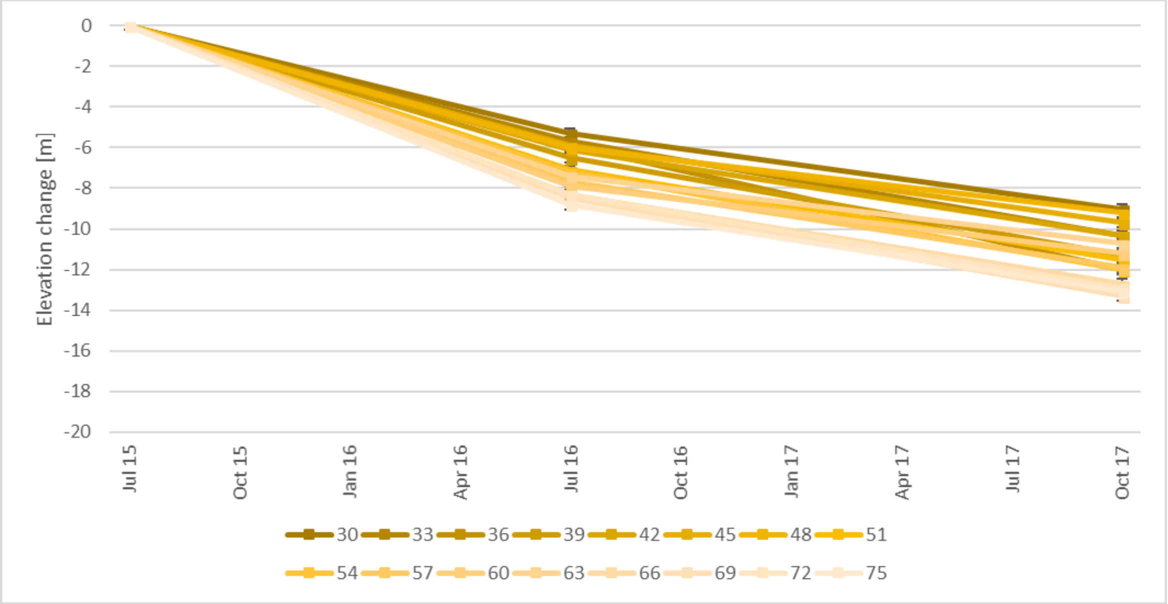

Fig. 37: Elevation changes for each point on the middle of the medial moraine between July 2015 and October 2017.

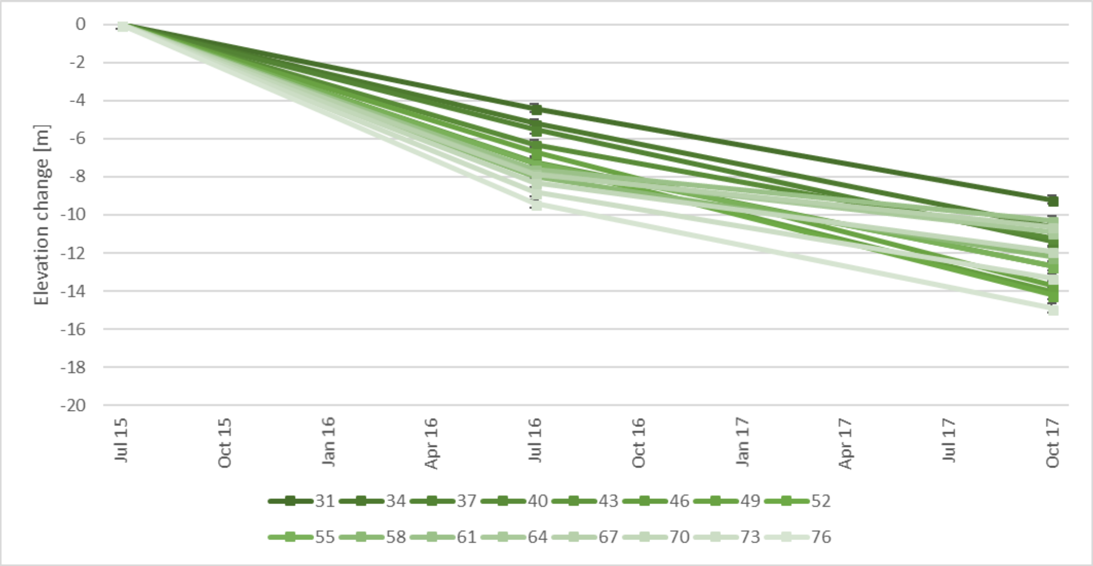

Fig. 38: Elevation changes for each point on the left side of the medial moraine between July 2015 and October 2017.

5.4.2.3. Sediment hill

A total of three profiles were drawn on the sediment hill to visualize its temporal development (Fig. 41). The markers in Fig. 41 and the line charts indicate where the beginnings of the graphs are.

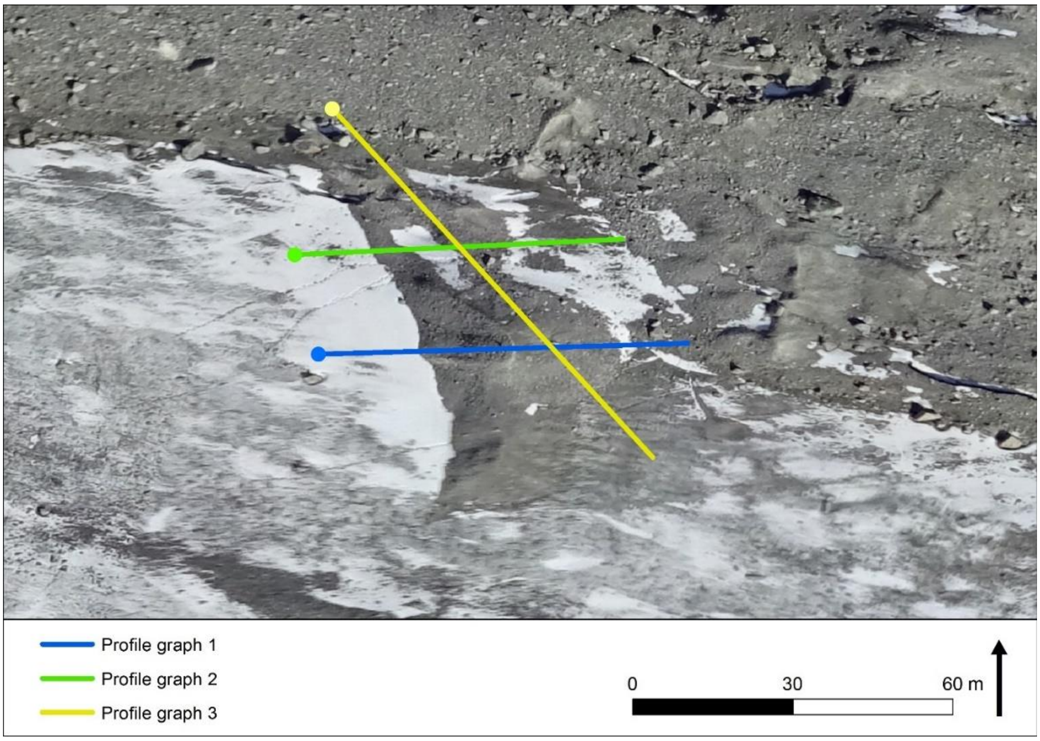

Fig. 39: Profile graphs drawn on the sediment hill. The round markers indicate where the profiles begin in the line charts.

Profile 1 in Fig. 42 was placed in flow direction over the small patch of debris that was already visible in July 2015. The first indication of the sediment hill, however, is only visible in the graph of July 2016 in the form of a small, around 1 m tall bump. By October 2017, the small patch had developed into a roughly 5 m tall and 25 m long sediment hill. The highest point of the hill remained roughly at the same elevation, but it has moved about 5 m against the flow direction farther uphill. Consequently, in October 2017, the top of the sediment hill lies 0.7 ± 0.18 m higher than the ice surface at the same location in July 2016. The ice surface surrounding the sediment hill experienced considerable downwasting within these three years. Between July 2014 and October 2017, the surface lost roughly -13.5 – -14 m of elevation, the biggest loss being between July 2015 and July 2016 with -5 – -5.5 m.

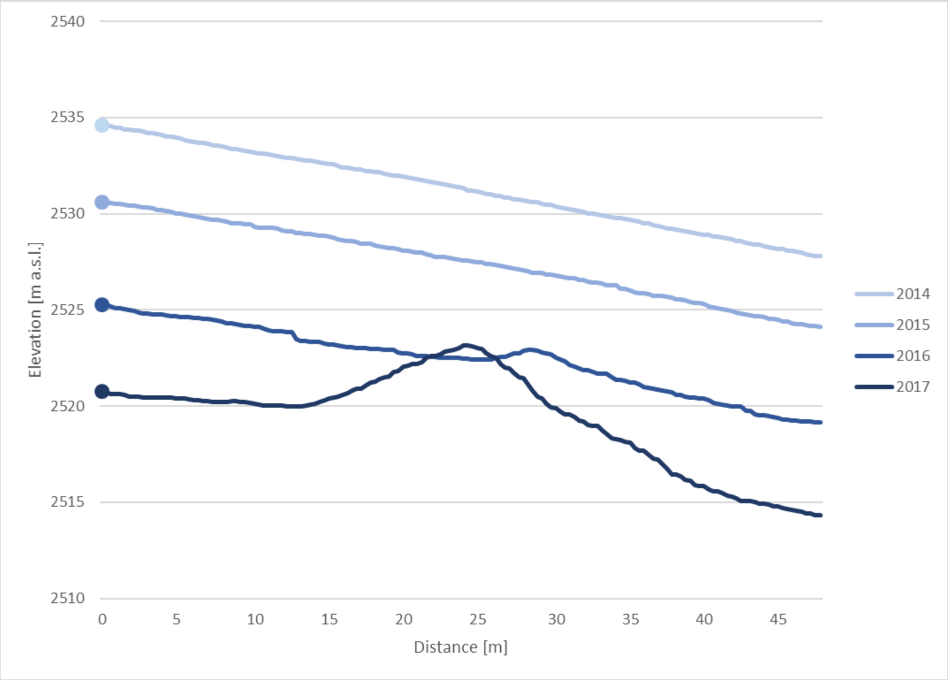

Fig. 40: Line chart showing the surface elevation along Profile graph 1 between July 2014 and October 2017.

The second profile was placed in flow direction as well, but around 20 m farther to the North, where the hill is not as tall (Fig. 43). Although the debris is clearly visible in the orthophoto of October 2017, its vertical dimensions are barely noticeable in the line chart. The debris-covered surface stretches from the 10 m mark to the 30 m mark in the chart and is slightly elevated by about 1–1.5 m. The elevation loss of the surrounding ice surface does not differ significantly from the first profile.

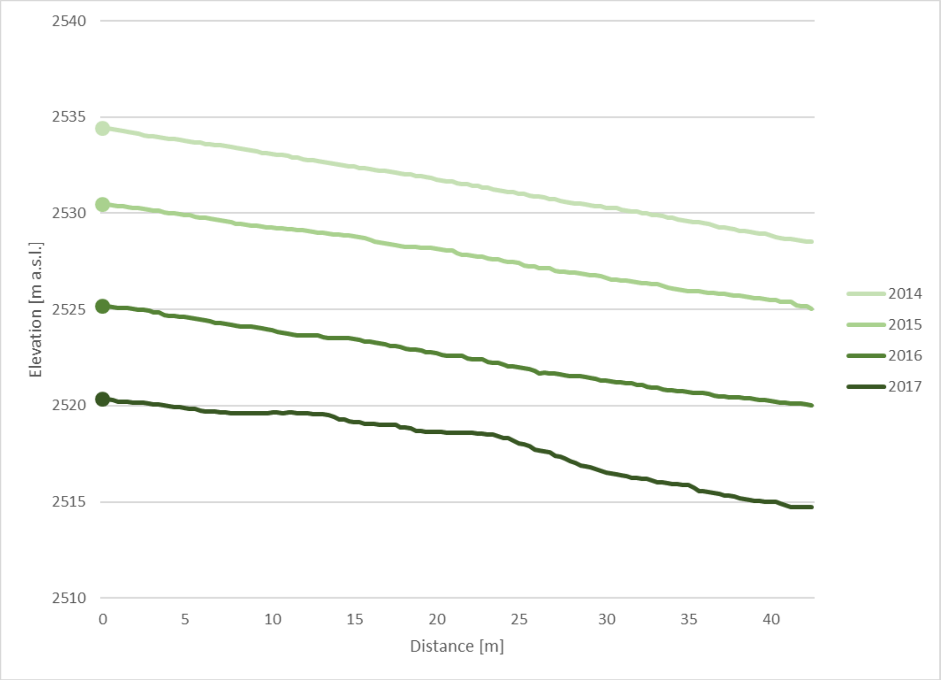

Fig. 41: Line chart showing the surface elevation along Profile graph 2 between July 2014 and October 2017.

The third profile lies perpendicular to the ice flow and crosses the highest point of the sediment hill as well as its southern extension, which is only visible in the orthophoto of October 2017 (Fig. 44). As in the line chart for Profile 2, the formation of the sediment hill is not visible until October 2017, since the profile does not cover the small patch of debris already protruding in July 2015. However, contrary to the debris-covered area to the North of the hill, the southern end of the hill shows a considerable elevation difference compared to the surrounding ice surface. Its ridge lies roughly 3 m higher than the ice surface and it stretches from the 40 m mark to the 60 m mark in the chart. As already observed in the first profile, the peak of the sediment hill lies 0.7 ± 0.18 m higher in 2017 than the ice surface did in the same location in 2016.

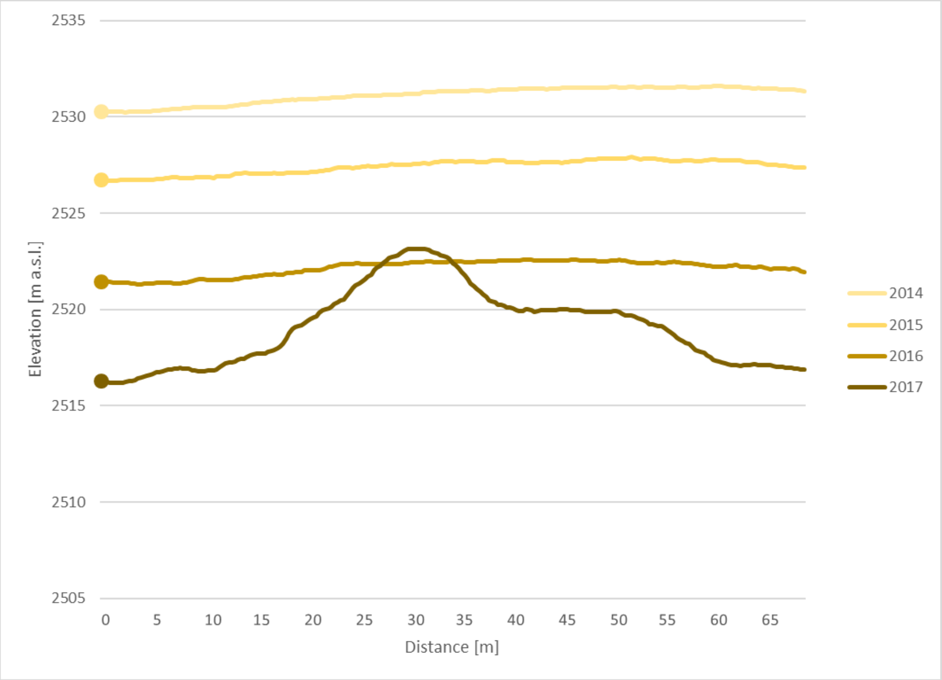

Fig. 42: Line chart showing the surface elevation along Profile graph 3 between July 2014 and October 2017.

5.4.2.4. Ice cliff

All three profiles for the ice cliff were drawn perpendicular to its movement (Fig. 45).

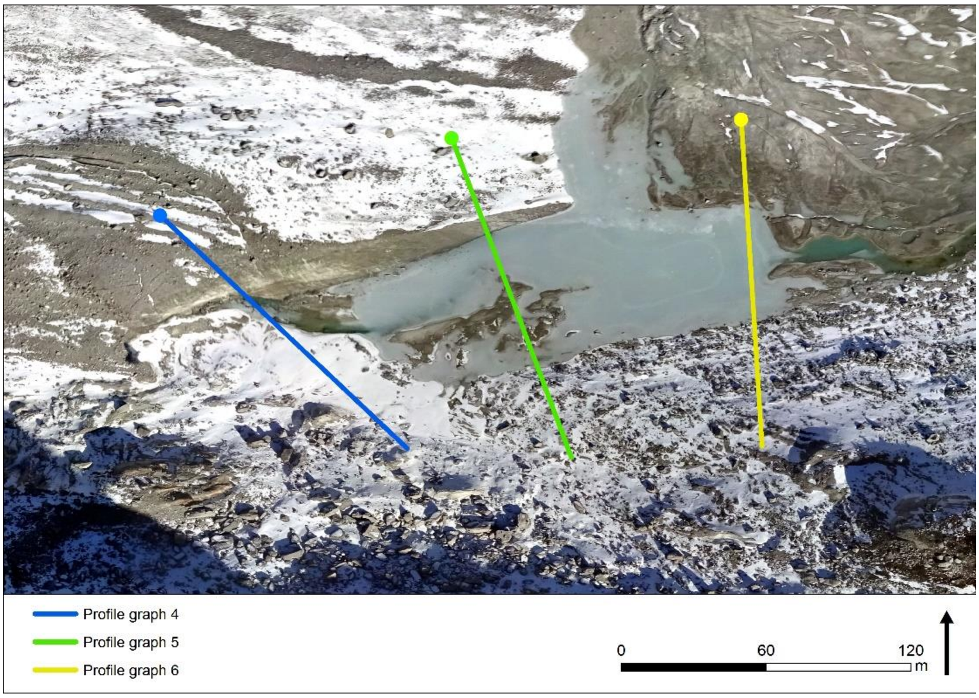

Fig. 43: Profile graphs drawn on the ice cliff. The markers indicate where the profiles begin in the line charts.

Profile 4 was drawn on its western end, stretching from the lower end of the medial moraine across the cliff onto non-glaciated surface (Fig. 46). The surface of the medial moraine at the left end of the chart shows a similar amount of elevation loss as the ice surface around the sediment hill. Between July 2014 and October 2017, a loss of -11 – -12.5 m is measured, with the biggest loss occurring again between July 2015 and July 2016 (Table 12). The elevation difference on the cliff itself is much larger due to its sideways moving nature caused by its direct exposure towards the sun. The largest difference can be found where the bottom of the cliff transitions into the melt water lake. Between July 2014 and October 2017, the surface shows a difference of 22.4 ± 0.2 m. At the same time, the front of the cliff moved between 29–35.5 m horizontally. Surprisingly, the largest horizontal movement is measured between July 2016 and October 2017 (13.5–15.5 m) and not in the year before (8.5–11.5 m), as it is the case for the vertical elevation change on the lower medial moraine. The ablation measured perpendicular to the surface of the cliff increases with time, as summarized in Table 12. On average, the perpendicular melt rate at the cliff's surface amounts to 7.7–9.2 m/a. The gradient of the cliff has slightly increased between July 2014 and July 2016 (69°, 72°, 78°, mean slope), but has decreased again in the following year (69°) (Table 13). The total height of the cliff does not change much over time. Furthermore, the surface at the lower end of the cliff lies 3.5 ± 0.2 m higher in 2017 than in the previous years. At the non-glaciated surface near the right end of the line chart, it even seems that the surface elevation continuously increased over the course of the three years.

Table 12: Horizontal movement, height change, and perpendicular backwasting observed on all three profile graphs of the ice cliff between July 2014 and October 2017.

	Horizontal movement [m]			**Cliff height change [m]**			**Perpendicular backwasting [m]**		
Time span	**Profile 4**	**Profile 5**	**Profile 6**	**Profile 4**	**Profile 5**	**Profile 6**	**Profile 4**	**Profile 5**	**Profile 6**
Jul 14–Jul 15	7–8.5	10–12.5	7.5–11	-2.7 ± 0.37	-3.2 ± 0.37	-5.2 ± 0.37	4.5–7	8–9	4.5–6.5
Jul 15–Jul 16	8.5–11.5	15–18	10.5–12.5	0.6 ± 0.23	-3.9 ± 0.23	-5.6 ± 0.23	7.5–9	13–14.5	5.5–7
Jul 16–Oct 17	13.5–15.5	14–16.5	-	-1 ± 0.18	-9.5 ± 0.18	-	13–14	12.5–13.5	2–4.5
Total	29–35.5	39–47	18–23.5	-3.1 ± 0.78	-16.6 ± 0.78	-10.8 ± 0.6	25–30	33.5–37	12–18

Table 13: Mean gradients observed on the ice cliff's surface between July 2014 and October 2017.

	Gradient (°)		
Date	**Profile 4**	**Profile 5**	**Profile 6**
Jul 14	69	66	54
Jul 15	72	67	46
Jul 16	78	76	35
Oct 17	69	52	-

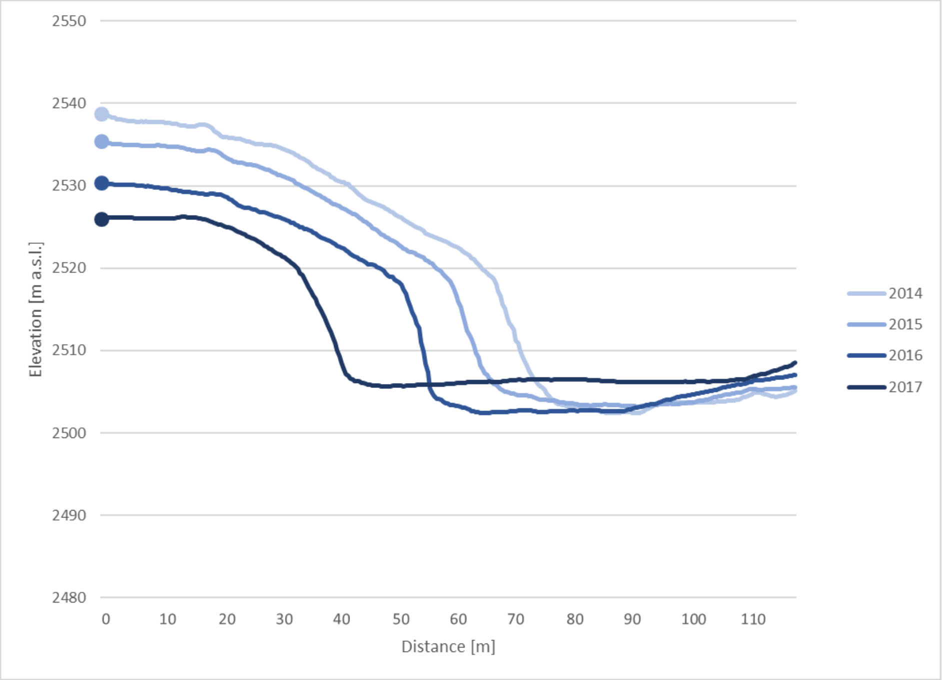

Fig. 46: Line chart showing the surface elevation along Profile graph 4 between July 2014 and October 2017.

Profile 5 stretches from the ice surface of the lower tongue over the ice cliff to the non-glaciated surface to the South of the cliff (Fig. 46). Contrary to the first profile, the largest elevation change to the North of the cliff is found between July 2016 and October 2017, with a loss of -5 – -5.5 m. The total downwasting of -10.5 – -11.5 m within the three observed years does not differ significantly from the one observed at the lower medial moraine in Profile 1. The development of the cliff's gradient is similar to the first profile as well, as it continuously increases until July 2016 (66°, 67°, 76°) and then becomes

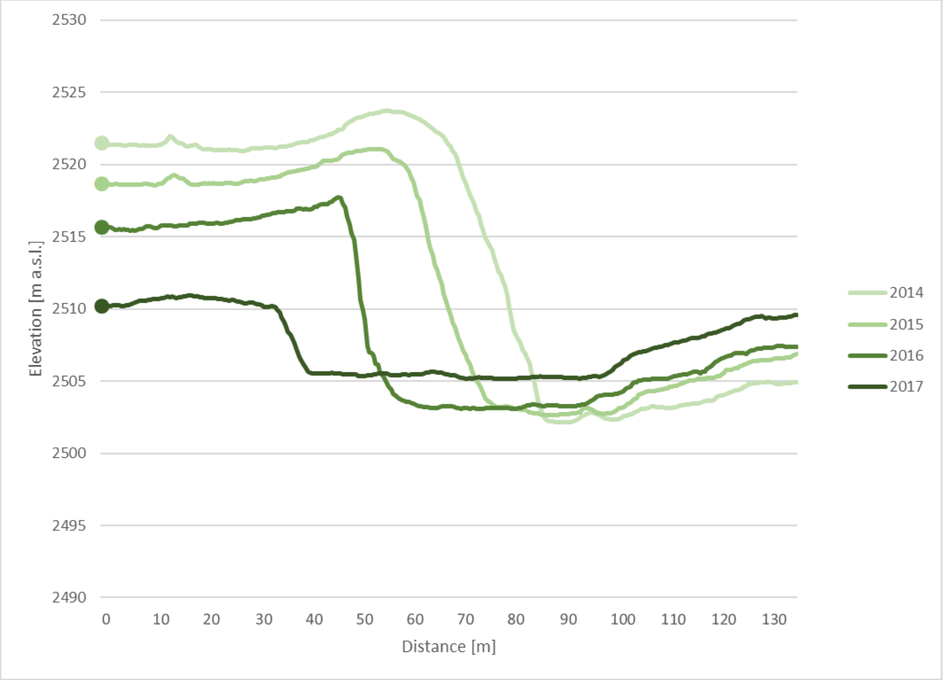

Fig.47: Line chart showing the surface elevation along Profile graph 5 between July 2014 and October 2017.

less steep again (52°). However, the height of the cliff clearly decreases over time, from 21 ± 0.2 m in July 2014 to just 4.5 ± 0.2 m in October 2017. The horizontal movement of the cliff is noticeably larger than in the first profile, with 39–47 m over the entire three years. The ablation measured perpendicular to the surface is larger as well with a total of 33.5–37 m. The surface beginning at the lower end of the ice cliff lies 2.1 ± 0.18 m higher in 2017 than in the previous years. The continuous elevation increase in the non-glaciated area is even more pronounced, with changes of up to 4.5 ± 0.18 m.

In the orthophoto of July 2014, Profile 6 reaches from the surface of the glacier tongue across the ice cliff onto non-glaciated surface. By October 2017, the tongue to the North of the cliff has entirely melted away, and the profile covers the sandy glacier forefield, the melt water lake as well as the non-glaciated area (Fig. 48). Between July 2014 and July 2016, the glacier tongue at the beginning of the profile lost 6 ± 0.28 m of elevation. However, the surface of the glacier forefield in 2017 lies 1.5 ± 0.18 m higher than the terminus of the glacier tongue did in 2016. In 2014, the cliff measured 16.3 ± 0.2 m tall, but is completely gone and thus unrecognizable in the line chart by the end of the observation period. In contrast to the previous two profiles, the gradient of the cliff's south-exposed surface gradually decreases (54°, 46°, 35°, 0°). Further, there is a decreasing gradient present on its northern side as well rather than a horizontal surface as it is the case in the other profiles. The surface of the proglacial lake is 1.5 ± 0.18 m higher in 2017 than the surface of the ice cliff the year before. Again, there is a positive elevation change in the non-glaciated area on the southern end of the profile. Between July 2014 and October 2017, this difference amounts to 3.5 ± 0.2 m.

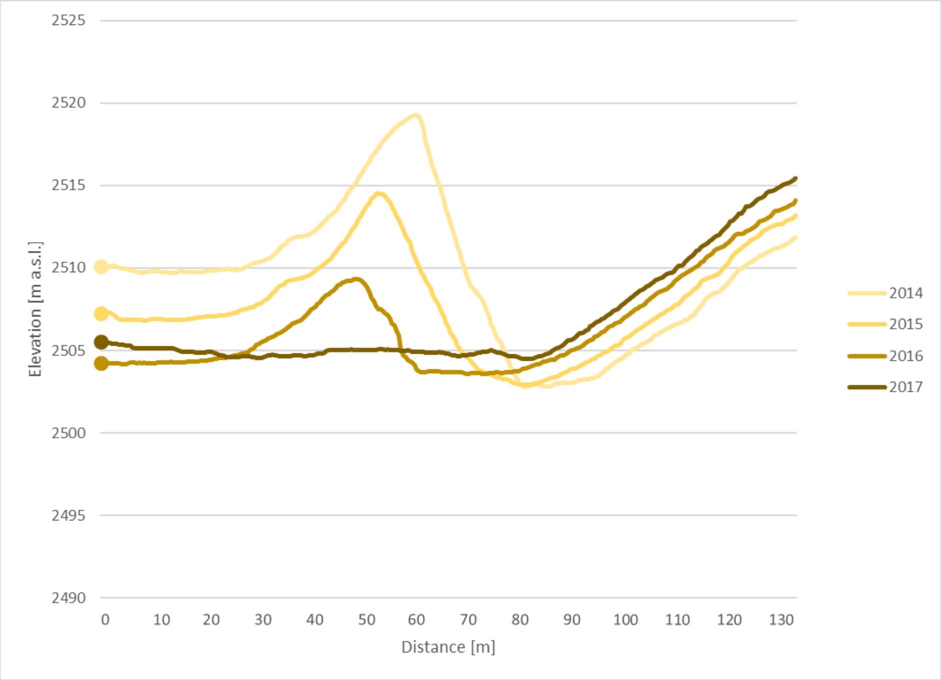

Fig. 44: Line chart showing the surface elevation along Profile graph 6 between July 2014 and October 2017.

5.4.2.5. Funnel-shaped subsidence

This profile covers the two depressions as well as the collapsed ice surface in flow direction (Fig. 49).

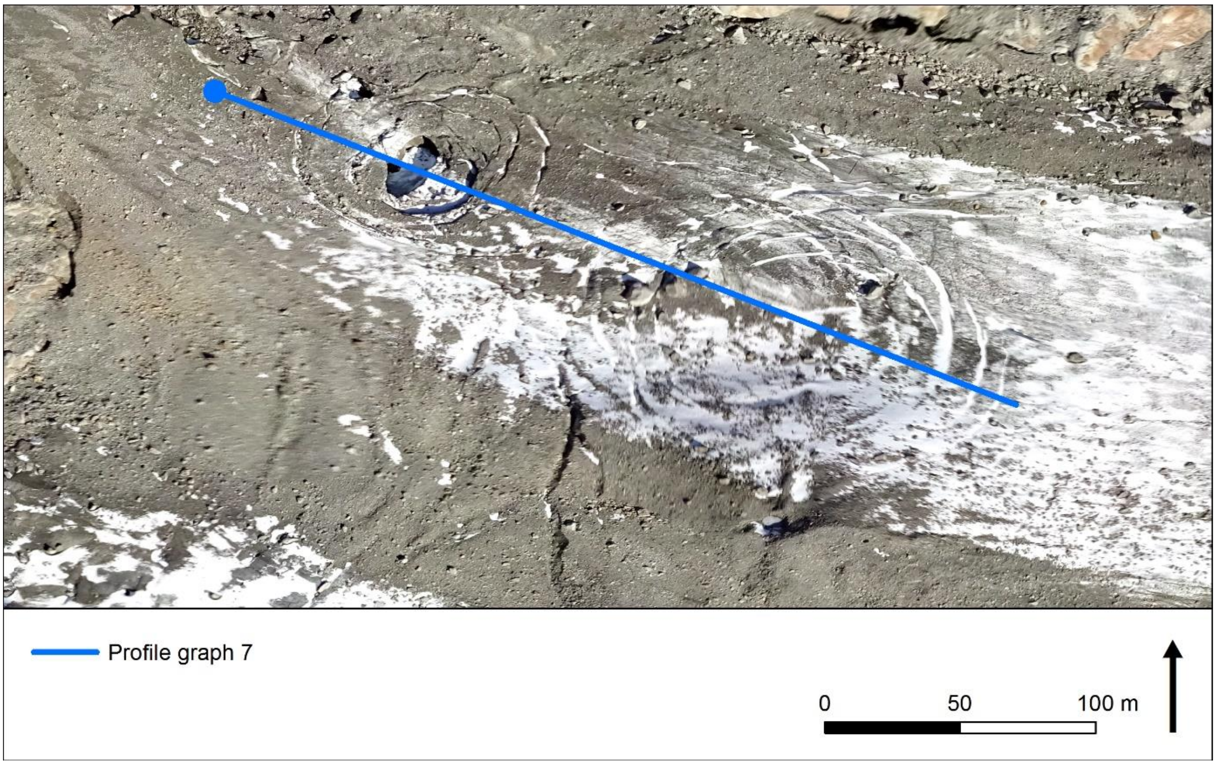

Fig. 45: Profile graph drawn on the funnel-shaped depressions. The round markers indicate where the profile begins in the line chart.

Since the DSM of July 2014 just covers the lower half of the glacier tongue, only a small part of it is included in the profile (Fig. 50). The graphs show quite a consistent elevation loss of the ice surface. Between July 2015 and October 2017, the changes are in the range of -8 – -10 m per year. The remainder of the graph for July 2014 suggests that the elevation change was smaller between July 2014 and July 2015. The spot where the ice surface collapsed in the summer of 2017 is clearly visible in the graph for the same year. It is difficult to assess how deep the hole underneath the collapsed surface is, as it was too dangerous to go near it during the field visit. Judging by the DSM, the hole is around 10 m deep at its deepest point and roughly 31 m long. The area where the hole would form in 2017 shows a slight change of the gradient in the previous two years from 27° to 16°. The same can be observed around the 165 m mark in all three graphs, where the center of the lower depression lies (6°, 4°, 2°). In July 2016 and October 2017, this area even seems to be slightly lower in elevation than the surface farther downstream. The small elevation around the 140 m mark in the graph of 2017 can be attributed to a boulder that fell onto the glacier.

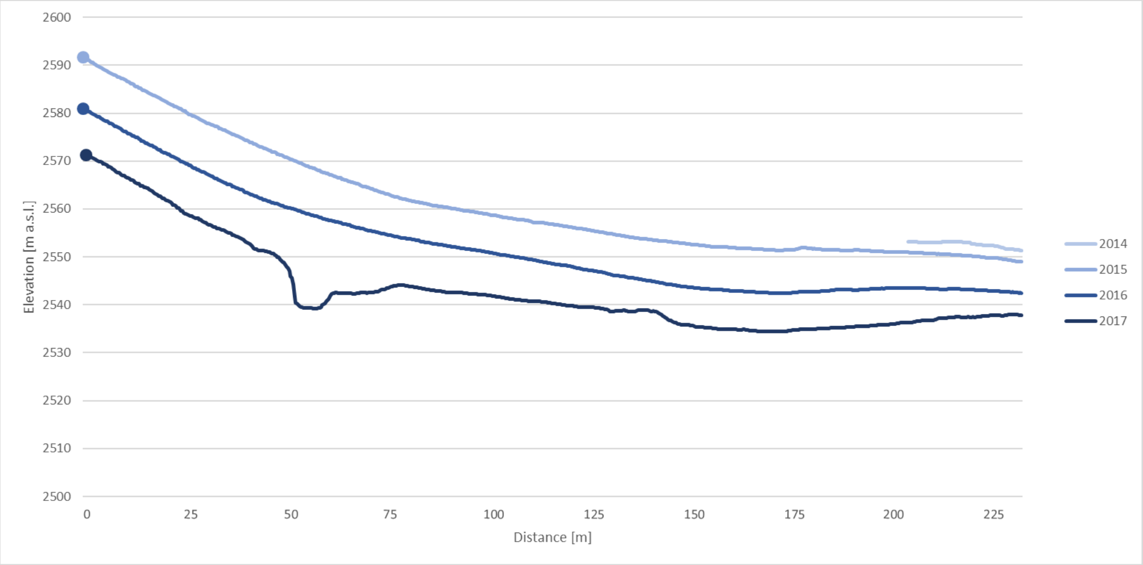

Fig. 46: Line chart showing the surface elevation along Profile graph 7 between July 2014 and October 2017.

5.5. Ablation

In the following, the ablation data acquired using three permanently installed ablation stakes will be described and compared to the elevation change data extracted from the DSMs. The ablation data collected between July 2014 and October 2017 can be found in Appendix 10.6. and is plotted in Fig. 51. The stakes 10, 11 and 12 show very similar amounts of ablation between July 2014 and July 2016, with a total of -8.48 m, -7.46 m and -7.76 m, respectively. Stake 12, which was left on the glacier until October 2017, continued to show a similar ablation trend. The final measurement, when the stake was removed from the glacier, was -15.50 m.

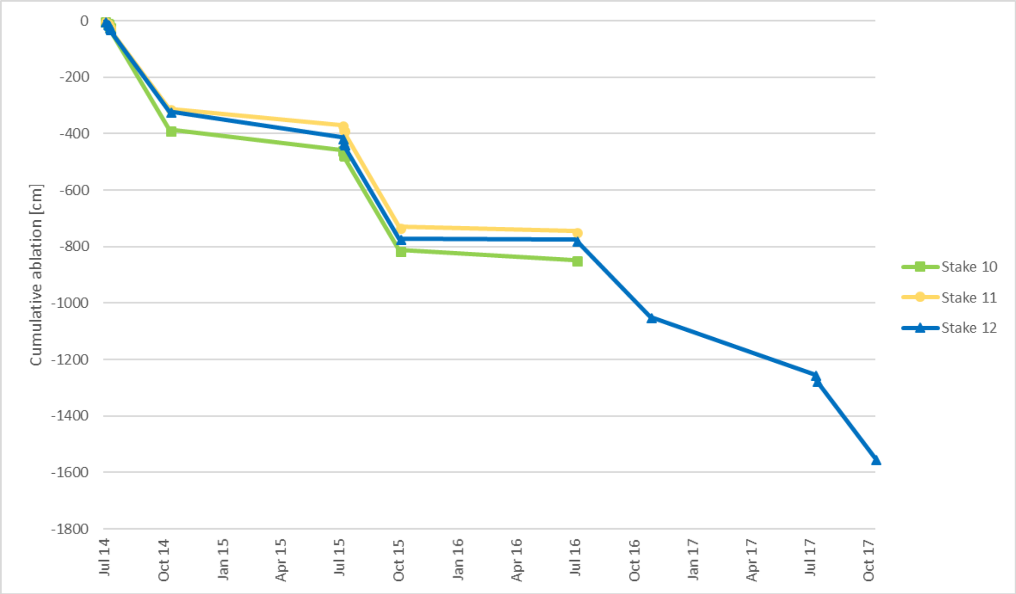

Fig. 47: Measured cumulative ablation measured at the three ablation stakes on the glacier tongue between July 2014 and October 2017.

Table 14 summarizes the measured ablation, cumulative ablation and cumulative elevation change at the locations of the stakes between July 2014 and October 2017. The ablation data differs from the one in Appendix 10.6., because the starting date of the measurements was adjusted to the one on which the first UAV flight was undertaken. This way, only the ablation measurements, which were conducted the same day the DSMs were acquired, are used, making the two data sets comparable. The elevation changes for Stake 12 were measured approx. 10 m further downstream, as the DSM of July 2014 does not reach the location where it was installed.

*Table 14: Measured ablation, cumulative ablation and cumulative elevation changes at the three ablation stakes between July 2014 and October 2017. *Extrapolated data.*

	Ablation [m]			**Cum. Ablation [m]**			**Cum. elevation change [m]**		
Time span	**Stake 10**	**Stake 11**	**Stake 12**	**Stake 10**	**Stake 11**	**Stake 12**	**Stake 10**	**Stake 11**	**Stake 12**
Jul 14–Jul 15	-4,38	-3,47	-3,89	-4,38	-3,47	-3,89	-4,03 ± 0,37	-3,89 ± 0,37	-5,15 ± 0,37
Jul 15–Jul 16	-4,27	-3,77	-3,63	-8,65	-7,24	-7,51	-9,33 ± 0,28	-10,07 ± 0,28	-13,48 ± 0,28
Jul 16–Oct 17	-7,74*	-7,74*	-7,74	-16,39	-14,98	-15,25	-14,40 ± 0,2	-15,14 ± 0,2	-20,06 ± 0,2

The cumulative elevation changes of Stakes 10 and 11 extracted from the latest DSM are very similar with -14.40 ± 0.2 m and -15.14 ± 0.2 m, respectively. Stake 12, however, shows a significantly larger change of -20.06 ± 0.2 m. This was expected, as the upper glacier tongue has experienced generally larger elevation changes than the lower part, as described in Chapter 5.2.3. Since Stakes 10 and 11 were removed in July 2016, no ablation data is available for October 2017. Because the ablation rates of all three stakes are very similar in the previous years, the ablation data for Stakes 10 and 11 have been linearly extrapolated for October 2017 using the data of Stake 12. This was done in order to gain more insight into the possible presence of dynamic replacement. Whether dynamic replacement is present or not was calculated according to Equation 5 by subtracting the cumulative ablation from the cumulative elevation change. If there is less elevation change than ablation, i.e. the values are positive, dynamic replacement exists (Fig. 52). Negative values, on the other hand, imply a greater elevation change than the ablation data can explain. All results within the error margin can be interpreted as neither dynamic replacement nor additional downwasting. In this case, the entire elevation change can be attributed to surface ice ablation.

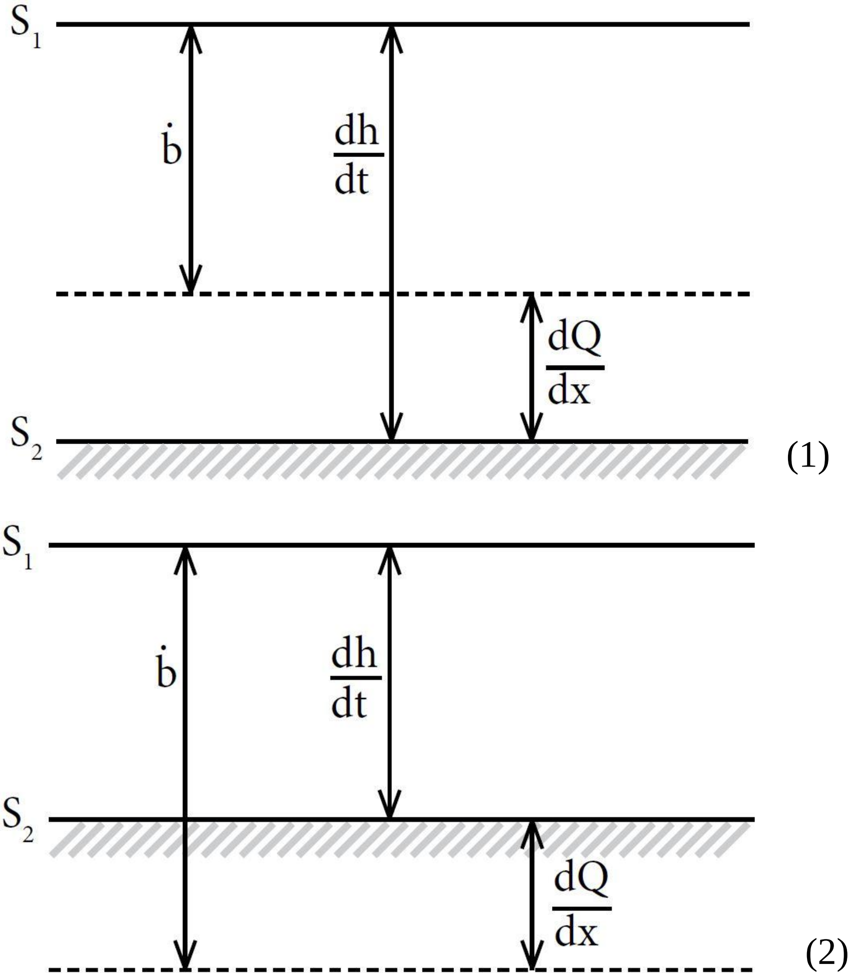

Fig. 48: Conceptual representation of dynamic replacement. (1) If there is more ablation ($\dot{b}$) than elevation change (dh/dt), dynamic replacement exists (dQ/dx). (2) Less ablation than elevation change means there is another dynamic process affecting the surface (S) elevation.

Table 15 and Fig. 53 feature the differences between the cumulative ablation and cumulative elevation changes. Between July 2014 and July 2015, most of the elevation change is explained by surface ablation, except for Stake 12, which has experienced -1.26 ± 0.37 m additional downwasting. The following year, all three stakes feature additional elevation loss not explained by ablation alone. The values in the column of October 2017 illustrate whether dynamic replacement or additional downwasting is present compared to the state the tongue was in in July 2014. Stake 12 has experienced an overall additional downwasting of -4.81 ± 0.2 m, which cannot be explained by ablation alone. The elevation change of Stake 11 mostly corresponds to the measured ablation data, as the difference only amounts to -0.16 ± 0.2 m. The ice surface at Stake 10, however, appears to have experienced a positive elevation change of 1.99 ± 0.2 m compared to the ablation data. The values for Stakes 10 and 11 in October 2017 need to be interpreted with caution, though, as they are partially based on extrapolated data, as described above. This data suggests that between July 2014 and July 2016, all three locations experienced surface lowering that is caused by something other than ablation, whereas in the following year, a sudden event of dynamic replacement lifted the surface considerably.

*Table 15: Cumulative ablation subtracted from cumulative elevation change at the three ablation stakes between July 2014 and October 2017. Positive values indicate the presence of dynamic replacement. *The ablation measurements used for the calculation of these values are extrapolated data.*

	Cum. elevation change – cum. ablation [m]		
Time span	**Stake 10**	**Stake 11**	**Stake 12**
Jul 14–Jul 15	0.36 ± 0.37	-0.42 ± 0.37	-1.26 ± 0.37
Jul 15–Jul 16	-0.68 ± 0.65	-2.83 ± 0.65	-5.97 ± 0.65*
Jul 16–Oct 17	1.99 ± 0.85	-0.16 ± 0.85	-4.81 ± 0.85*

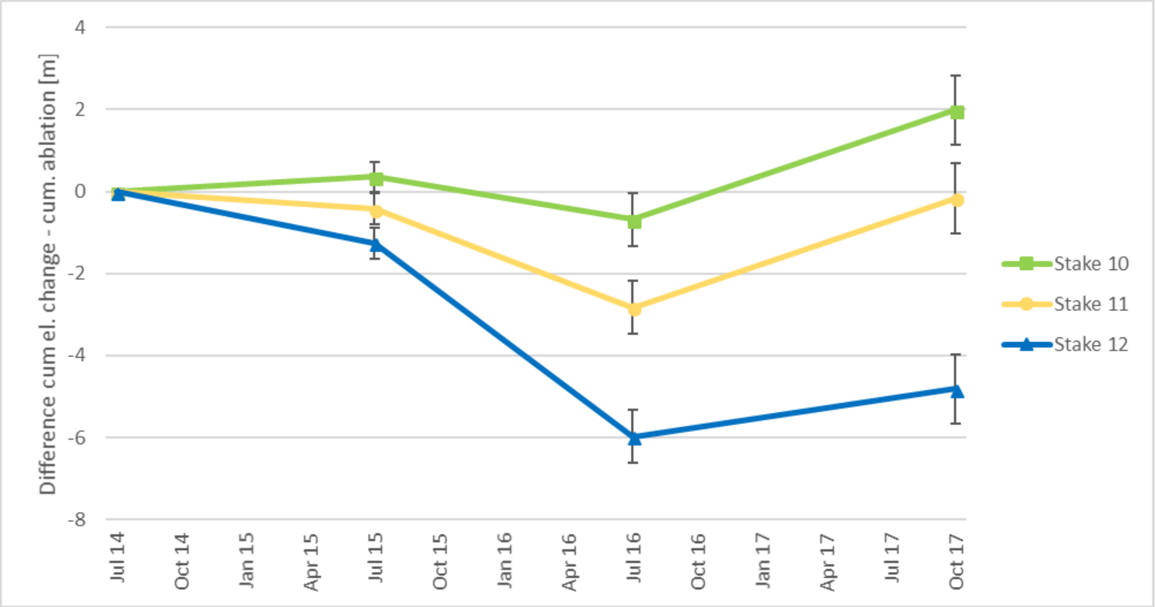

Fig. 49: Cumulative ablation subtracted from cumulative elevation change at the three ablation stakes between July 2014 and October 2017. Positive values indicate the presence of dynamic replacement.

5.6. Supraglacial debris

The distribution, thickness and composition of supraglacial debris strongly influences the magnitude of the ablation of underlying ice, which makes it necessary to include when analyzing a glacier tongue's geometry. This section covers the mapped distribution of supraglacial debris on the glacier tongue in October 2017 as well as its effect on surface ablation.

5.6.1. Distribution

The distribution of the supraglacial debris on the glacier tongue in October 2017 is shown in Fig. 54. The twelve different categories of debris, which are based on location, grain size and roundness, are summarized in Table 16 with a brief description of each category.

Category 1 consists of a thin, discontinuous layer of mostly flat, dark schist rocks mixed with small granite cobbles, a few small boulders and a layer of sand. Although the transition between Categories 1, 2 and 12 is very fluent, the former was classified as a separate category because of the presence of dark schist, which cannot be found in the latter two categories. The second category includes the very top of the glacier tongue where it used to be connected to the upper glacier. Due to the steepness of this area, only sand and gravel is present, as larger rocks and boulders would slide off the surface. Nevertheless, the sandy cover is quite continuous. The sediment hill was chosen to be classified as a separate category, as its debris shows a much higher degree of roundness than its surroundings. On top of the rather deep layer of sand and rounded gravel, some rounded as well as very angular small boulders can be found. Category 4, which is adjacent to the sediment hill, is quite similar to its composition, but the sandy layer is much thinner and considerably more of the small boulders are angular rather than rounded. The main body of the lateral moraine is a single category, although the characteristics of the debris are not entirely uniform across the moraine. However, in general it can be said that the grain size is very mixed, mostly very angular and sorted to some degree, with sand on the ice surface and very large boulders on top of the moraine. To the North of the lower lateral moraine, there is an accumulation of sand, rounded gravel and some small, angular boulders (Category 6). Category 7 is the elongated area directly to the North of the lateral moraine, which consists of very large, angular boulders, that most likely stem from the steep rock wall to its North. The composition of the thin stripe of debris beginning at the terminus in Category 9 resembles the one of Category 1 with thin plates of dark schist. In contrast to Category 1, this debris cover is continuous and fully covers the underlying ice. The lower end of the medial moraine forms Category 10, which consists of mostly small grain sizes such as sand and unrounded gravel with a few large boulders scattered across the sediment ridges. Like the lateral moraine, the most part of the medial moraine is classified as one category (Category 11). Its composition is similar to the lateral moraine as well, with a sandy layer on the ice surface, followed by unrounded gravel, cobbles and some very large boulders. The last category is a discontinuous, thin layer of sand close to the medial moraine, with a few large boulders that fell onto the glacier from the rock walls to the North.

Table 16: Details about the 12 categories of supraglacial debris, including grain size, roundness and a brief description.

Category	Grain size	Roundness	Description
1	Mixed, sand – boulders	Very angular	Thin layer of flat schist rocks, some debris-free surface
2	Mostly sand and gravel	Angular	Sand layer up to a few cm thick, no larger grain size because of steepness
3	Sand, gravel and small boulders	Rounded & some very angular boulders	Deep sandy layer with rounded cobbles on top; some very angular boulders
4	Sand, gravel and small boulders	Rounded – angular	Sandy layer with some small rounded and angular boulders
5	Sand – very large boulders	Very angular	Very mixed, but sorted debris; sandy layer on the ice surface and very large boulders on top; smaller boulders on slanted surfaces
6	Sand – small boulders	Rounded – angular	Mostly sand and rounded gravel because of steepness; some angular small boulders
7	Very large boulders	Very angular	Large boulders which probably broke off the steep rock wall
8	Sand – small boulders	Rounded – angular	Mostly sand because of steepness; some angular small boulders
9	Sand – cobbles	Very angular	Thin, but continuous layer of flat, dark schist
10	Sand – large boulders	Very angular	Mostly sand and gravel, few large boulders scattered
11	Sand – large boulders	Very angular	Very mixed, but sorted debris; sandy layer on the ice surface and very large boulders on top; smaller boulders on slanted surfaces
12	Sand and large boulders	Very angular	Discontinuous layer of sand and a few large boulders; some debris-free ice

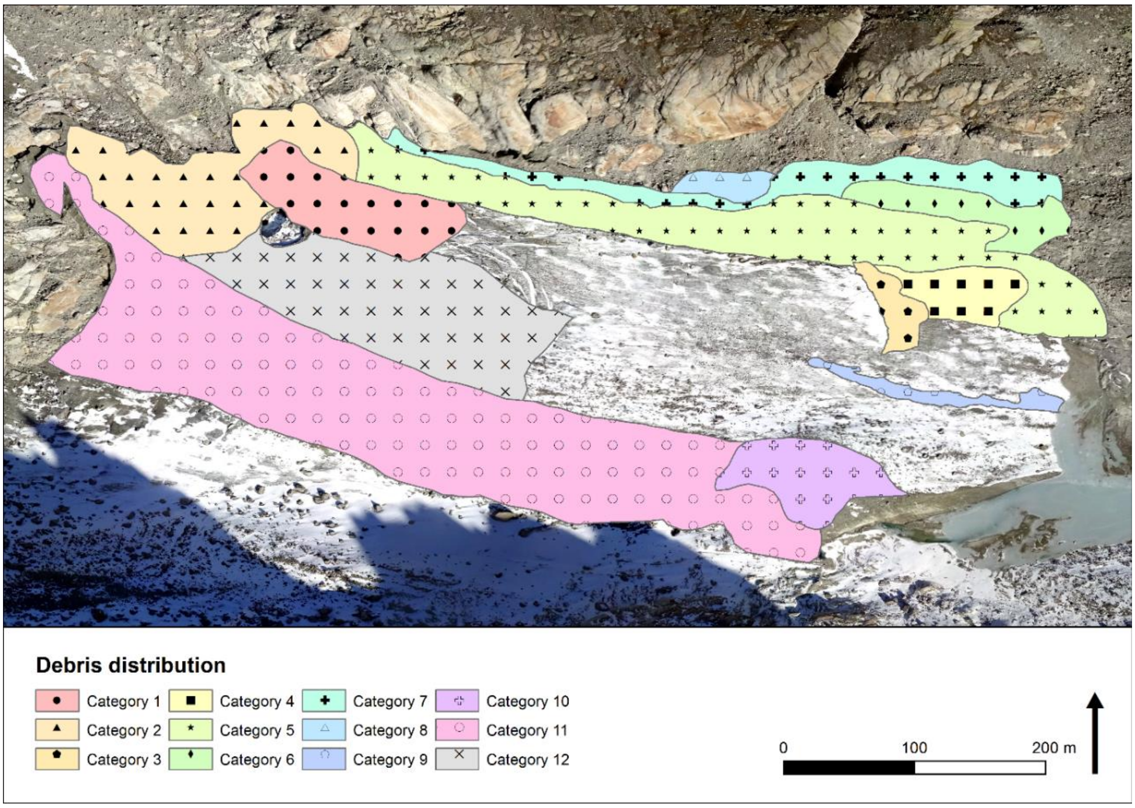

Fig. 50: Distribution of supraglacial debris divided into 12 categories on the Tiefenglacier's tongue in October 2017.

5.6.2. Effect on ablation

In the following, the effect the supraglacial debris has on the underlying ice is presented by comparing both the surface elevation changes and the surface ablation with the measured debris thicknesses. The 13 debris thickness measurements conducted during the field visit in October 2017 are summarized in Table 17, including the observed grain size, rounding, average debris thickness as well as a short description of the measurement site (Fig. 55). The elevation differences extracted from the difference images are added as well for the comparison with the debris thickness at each measurement site. All remaining debris thickness measurements by Achermann et al. (2015), Engeler et al. (2016) and Hasler et al. (2014) can be found in Appendix 10.7.

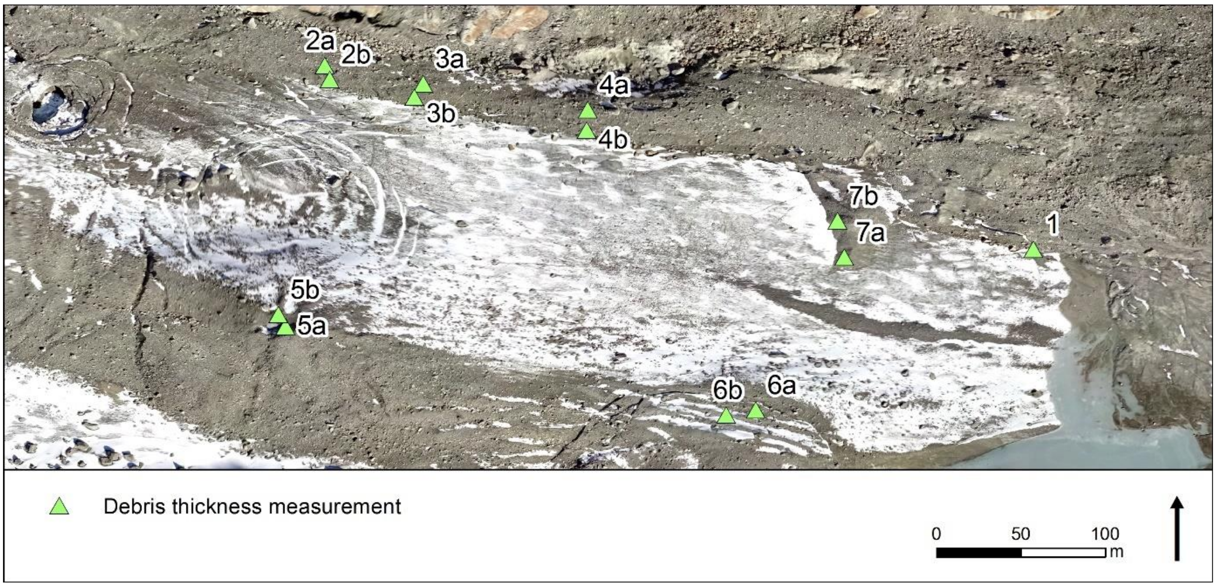

Fig. 51: Locations of the debris thickness measurements conducted in October 2017.

Table 17: Details about the 13 debris thickness measurements conducted in October 2017, including grain size, rounding, average debris thickness, a brief description of the measurement site as well as elevation changes extracted from the difference images.

					Elevation change [m]			
Measurement	**Grain size**	**Rounding**	**Av. debris thickness**	**Description**	**Jul 14 – Jul 15**	**Jul 15 – Jul 16**	**Jul 16 – Oct 17**	**Jul 14 – Oct 17**
1	Sand – small boulders	Well-rounded, some very angular boulders on top	4	Left side of glacier terminus; debris emerges from within the ice in a 15-20° angle	- 3.43 ± 0.37	- 3.83 ± 0.23	- 6 ± 0.18	- 13.26 ± 0.78
2a	Sand with boulders on top (20-30 cm)	Very angular	7	Upper lateral moraine, top, flat surface	-	- 8.23 ± 0.23	- 6.7 ± 0.18	- 14.93 ± 0.41
2b	Sand with gravel on top	Very angular	3	Upper lateral moraine, S-exposed side, slanted 30°	-	- 8.1 ± 0.23	- 6.82 ± 0.18	- 14.92 ± 0.41
3a	Sand with boulders on top (20-30 cm)	Very angular	5	Middle lateral moraine, top, flat surface	- 4.55 ± 0.37	- 7.29 ± 0.23	- 5.23 ± 0.18	- 17.07 ± 0.78
3b	Sand with gravel on top	Very angular	5	Middle lateral moraine, S-exposed side, slanted 30°	- 4.78 ± 0.37	- 7.33 ± 0.23	- 5.33 ± 0.18	- 17.44 ± 0.78
4a	Sand with boulders on top (20-30 cm)	Very angular	5	Lower lateral moraine, top, flat surface	- 3.34 ± 0.37	- 5.99 ± 0.23	- 2.25 ± 0.18	- 11.58 ± 0.78
4b	Sand with gravel on top	Very angular	3	Lower lateral moraine, S-exposed side, slanted 30°	- 3.94 ± 0.37	- 6.61 ± 0.23	- 3.05 ± 0.18	- 13.6 ± 0.78
5a	7cm layer sand, 10cm boulders on top	Very angular	17	Middle medial moraine, flat surface, slightly N-exposed, 5m away from lake	-	- 8.12 ± 0.23	- 4.54 ± 0.18	- 12.66 ± 0.41
5b	8cm layer sand, 5cm gravel and small boulders on top	Very angular	13	Middle medial moraine, slightly slanted, next to lake	-	- 7.62 ± 0.23	- 3.94 ± 0.18	- 11.56 ± 0.41
6a	Sand with gravel on top	Very angular	3	Lower medial moraine, flat surface, on a longitudinal crevasse-fill ridge, orographically farther left	- 3.6 ± 0.37	- 5.39 ± 0.23	- 5.38 ± 0.18	- 14.37 ± 0.78
6b	Sand with gravel on top	Very angular	5	Lower medial moraine, flat surface, on a longitudinal crevasse-fill ridge, orographically farther right	- 3.56 ± 0.37	- 5.61 ± 0.23	- 5.31 ± 0.18	- 14.48 ± 0.78
7a	Sand with small boulders on top	Rounded, some very angular boulders on top	13	Right side of sediment hill, W-exposed, slanted 15°	- 3.8 ± 0.37	- 5.42 ± 0.23	- 3.1 ± 0.18	- 12.32 ± 0.78
7b	Deep sand layer with small boulders on top	Rounded, some very angular boulders on top	40	Middle of sediment hill, W-exposed, slanted 20°	- 3.79 ± 0.37	- 5.45 ± 0.23	- 1.96 ± 0.18	- 11.2 ± 0.78

5.6.2.1. Surface elevation changes vs debris thickness

Fig. 56 shows the surface elevation changes between July 2016 and October 2017 plotted against the debris thicknesses measured during the field visit. In general, it can be said that the elevation change decreases with increasing debris thickness, which was to be expected due to the debris' insulating effects. The largest elevation differences are mainly found on the upper lateral moraine with up to -6.82 ± 0.18 m. Interestingly, Point 7b, which was measured approximately in the middle of the sediment hill, shows elevation changes similar to Points 4a and 4b, although the sediment layer is much thinner at the latter measurement points. Since there are only 13 measurements and none of them are less than 3 cm of debris, it is not possible to see any melt-enhancing effects by thin layers of debris. Further, the elevation change measurements were extracted from the difference images, which means that the debris layers could have changed in their extent and thickness between 2016 and 2017. Therefore, this plot serves more as a general overview of the debris' insulating effects.

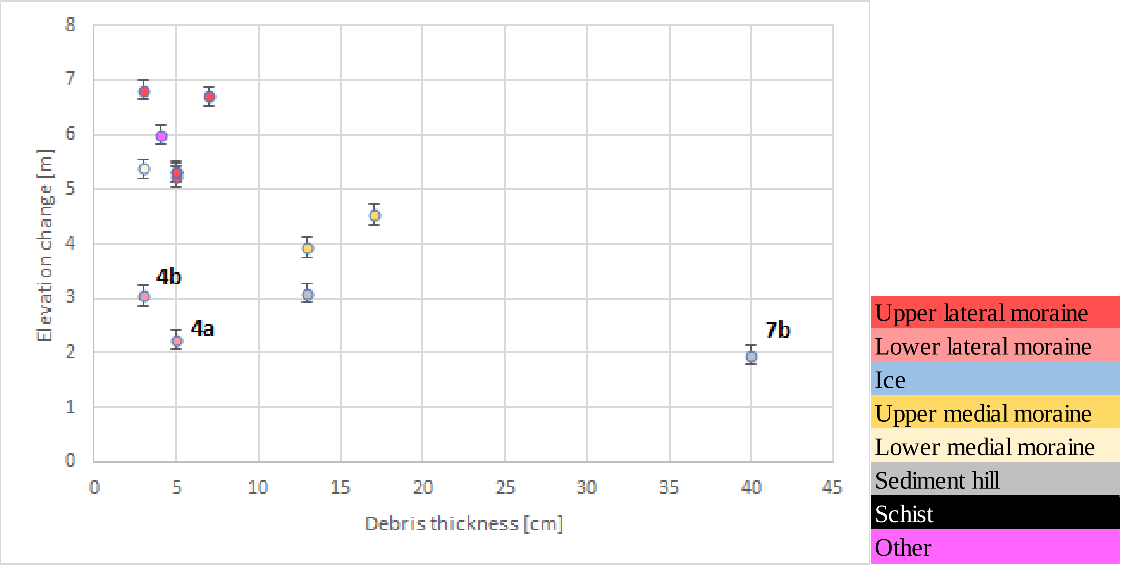

Fig. 52: Debris thickness measurements conducted in October 2017 plotted against surface elevation changes between July 2016 and October 2017. The colors indicate where the measurement was taken.

The plot in Fig. 57 represents debris thickness measurements conducted by Achermann et al. (2015) plotted against the elevation changes between July 2014 and July 2015. Again, there is a clear trend indicating that thick layers of debris decrease the melt of the ice underneath. The elevation changes observed at the five points on ice without any debris range from -1.52 ± 0.37 m to -3.92 ± 0.37 m. The elevation differences between 1 cm and 10 cm show an even greater range, from -1.64 ± 0.37 m to -4.56 ± 0.37 m. Further, the relative positions of the colors in the plot roughly match the ones of Fig. 56. These observations and the fact that the data points are clustered according to their location on the glacier tongue suggest that not only the debris thickness, but also the characteristics of the individual glacial features have a significant influence on the ice melt. Points A48 and A49, which were measured farther downstream of the glacier and are thereby classified as *other*, show that from a certain point on, additional debris thickness does not increase the insulating effect noticeably.

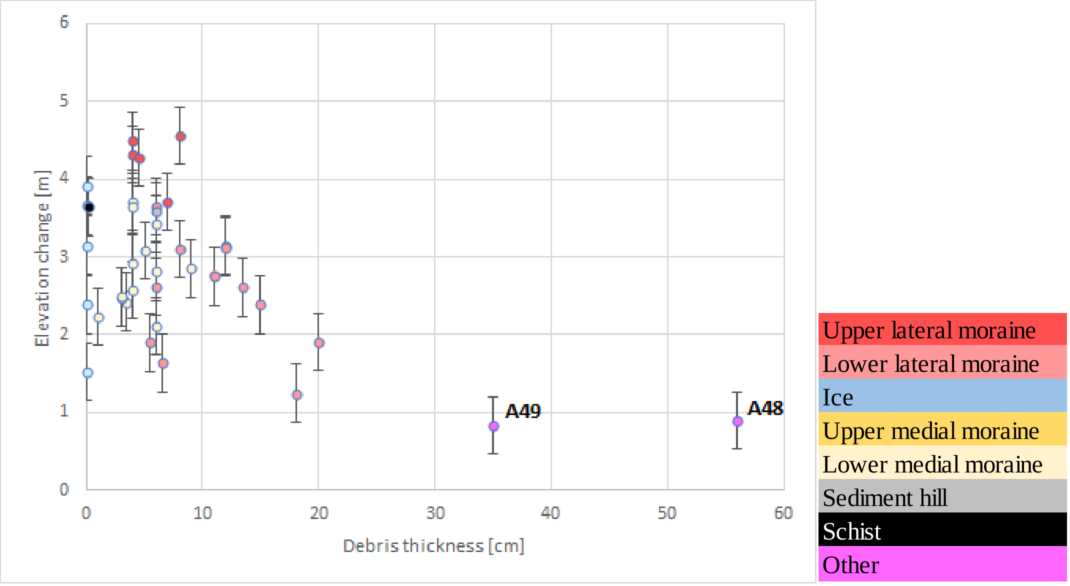

Fig. 53: Debris thickness measurements extracted from a field report from July 2015 plotted against surface elevation changes between July 2014 and July 2015. The colors indicate where the measurement was taken.

5.6.2.2. Surface ice melt vs debris thickness

In Figs. 58 through 60, the measured surface ice melt is shown plotted against the thickness of the overlying debris. Since every group conducted their measurements in different years, their data cannot be represented in a single plot due to the dynamic nature of the glacier tongue and varying meteorological circumstances. As expected, the surface melt generally decreases with increasing debris thickness. However, while the decreasing trend is already visible in the first couple of centimeters at Hasler et al. (2014) and Achermann et al.'s (2015) measurements, the decrease is much less prominent in Engler et al.'s (2016) data. Especially the layer of schist seems to produce relatively high melt rates at a thickness of both 0.2 cm in Fig. 58 and 5 cm in Fig. 59. Further, the measurements conducted by Achermann et al. (2015) and Hasler et al. (2014) at debris layers thinner than 1 cm suggest that these layers enhance the ice melt by heating up. Point H7 in Fig. 60 shows an unusually high melt rate given a debris layer of 20 cm. This is the result of the structure of the debris, which, according to Hasler et al. (2014), was a pile of small to medium sized boulders rather than a solid debris cover, allowing a steady circulation of air.

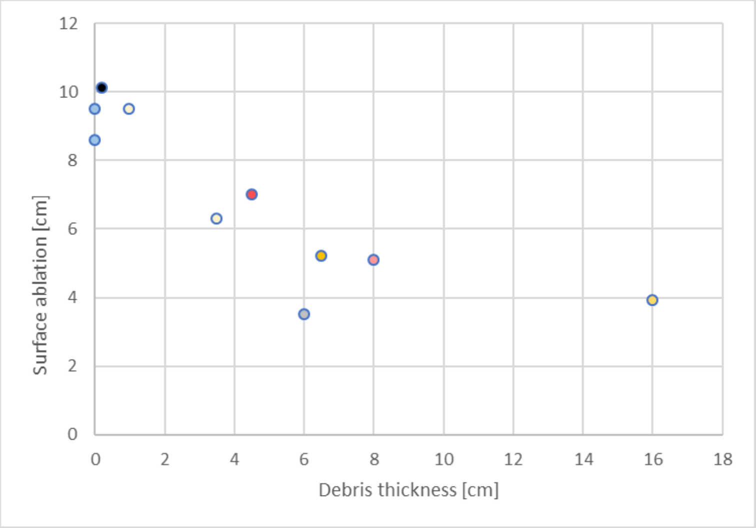

Fig. 54: Debris thickness plotted against surface ablation extracted from a field report from July 2015.

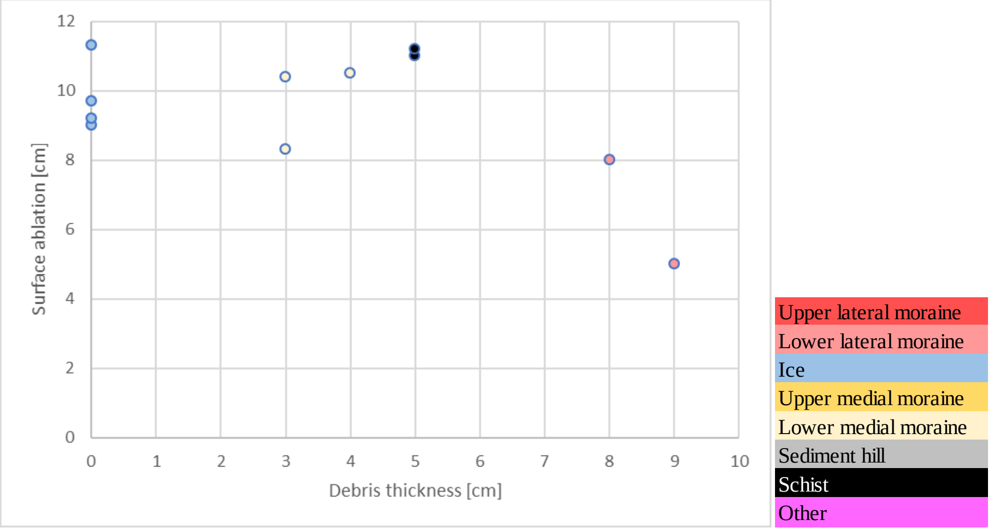

Fig. 55: Debris thickness plotted against surface ablation extracted from a field report from July 2016.

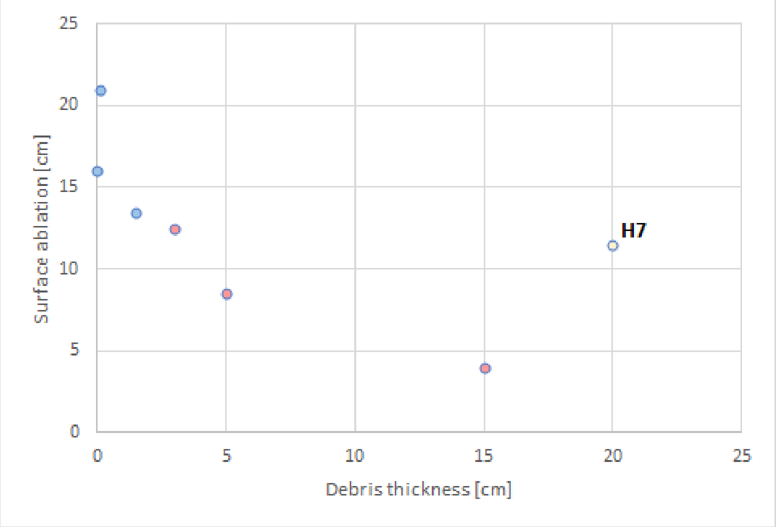

Fig. 56: Debris thickness plotted against surface ablation extracted from a field report from July 2014.

5.6.2.3. Ablation relative to no debris

The above presented data has been calculated into daily ablation rates (Appendix 10.8.) and then compared to the average daily ablation at stakes without any debris (Fig. 61). The value *1.0* on the y-axis stands for the average of all measured daily melt rates with 0 cm debris (4.46 cm/d). The measurements of Achermann et al. (2015) show generally lower ablation than the ones of Engeler et al. (2016) and Hasler et al. (2014). This can be attributed to the weather during the experiments, as they only lasted for a few days, and are therefore rather sensitive to changes in temperature, precipitation and radiation. Between 0 cm and 5 cm of debris, there are large differences in the relative ablation, ranging from 0.56 to 2.05. This suggests once more that the thickness of the supraglacial debris is not the only controlling factor for the surface ablation, but that the weather and the characteristics of the glacial features play an important role as well. Above 5 cm, however, the ablation was observed to be consistently smaller than the average at 0 cm. The outlier at 20 cm of debris shows that the presence of an air flow inside the debris can significantly affect the magnitude of the surface ablation, leading to even greater melt rates than on debris-free ice.

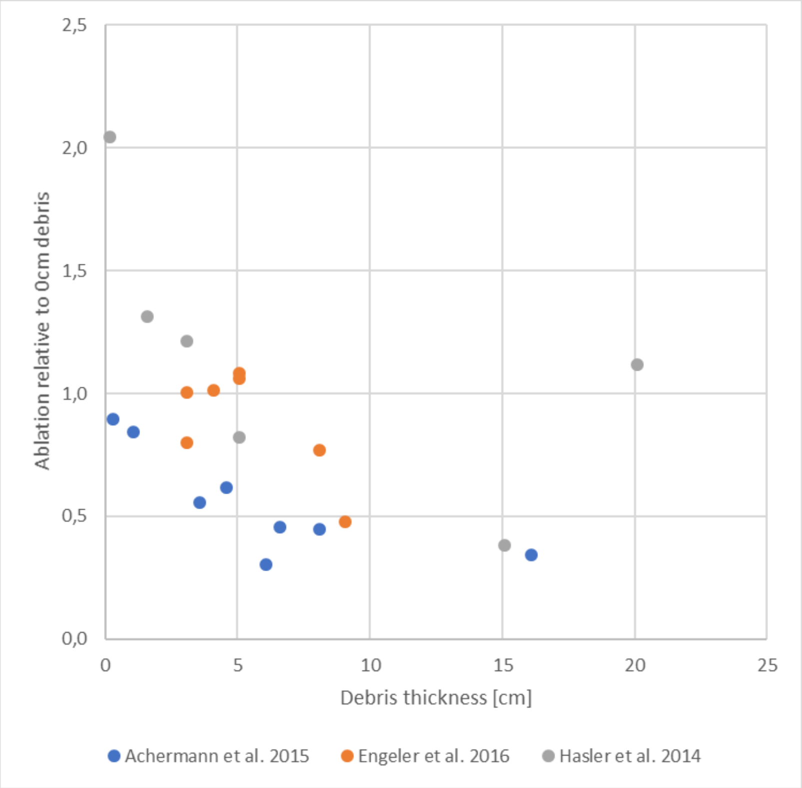

Fig. 57: Debris thickness plotted against surface ablation relative to no debris. The value 1 on the y-axis stands for the average ablation measured at locations without any supraglacial debris.

5.7. Ice flow velocity

The movements of a total of 11 rocks on the lower glacier tongue have been tracked between July 2014 and October 2017 (Fig. 62). Table 18 shows each rock's distance traveled in one-year steps, their total distance traveled, average distance per year, rock surface area and their distance to the terminus at the beginning of the measurements. The total distances traveled show big differences, ranging from 7.81 m by rock 4 to 32.49 m by Rock 5. Generally, the greatest distances by far were covered between July 2016 and October 2017, probably due to the longer observation period. Rocks 7 and 11, however, traveled roughly the same distance as the year before. Between 2015 and 2016, most rocks have been observed to cover longer distances than the year before as well. The average velocity per year ranges from 2.4 m/a at rock 4 to 10 m/a at Rock 5, which is more than four times the speed. Rocks 5 and 8, which show the highest velocities, can be viewed as outliers, though, as all the other rocks show velocities between 2.4 m/a and 5.7 m/a.

Table 18: Distances traveled by each rock as well as their average movement velocity, surface area and initial distance from the glacier terminus.

	Distance traveled [m]						
Rock	**Jul 14 – Jul 15**	**Jul 15 – Jul 16**	**Jul 16 – Oct 17**	**Total**	**Average velocity [m/a]**	**Surface area [m²]**	**Distance from terminus [m]**
1	2.88	4.09	5.92	12.89	4.0	2.53	207.9
2	0.59	2.94	5.27	8.8	2.7	1.80	254.1
3	1.29	2.9	4.99	9.18	2.8	2.01	227.4
4	1.6	2.11	4.1	7.81	2.4	3.14	253.4
5	8.93	6.48	17.08	32.49	10.0	9.57	397.6
6	1.17	6.19	10.84	18.2	5.6	6.09	329.5
7	1.81	8.41	8.27	18.49	5.7	5.42	189.7
8	2.78	5.52	15.38	23.68	7.3	10.59	155.3
9	3.39	3.47	7.58	14.44	4.4	7.38	291.7
10	2.3	3.42	8.25	13.97	4.3	4.54	348.7
11	1.57	3.24	3.62	8.43	2.6	2.30	119.1

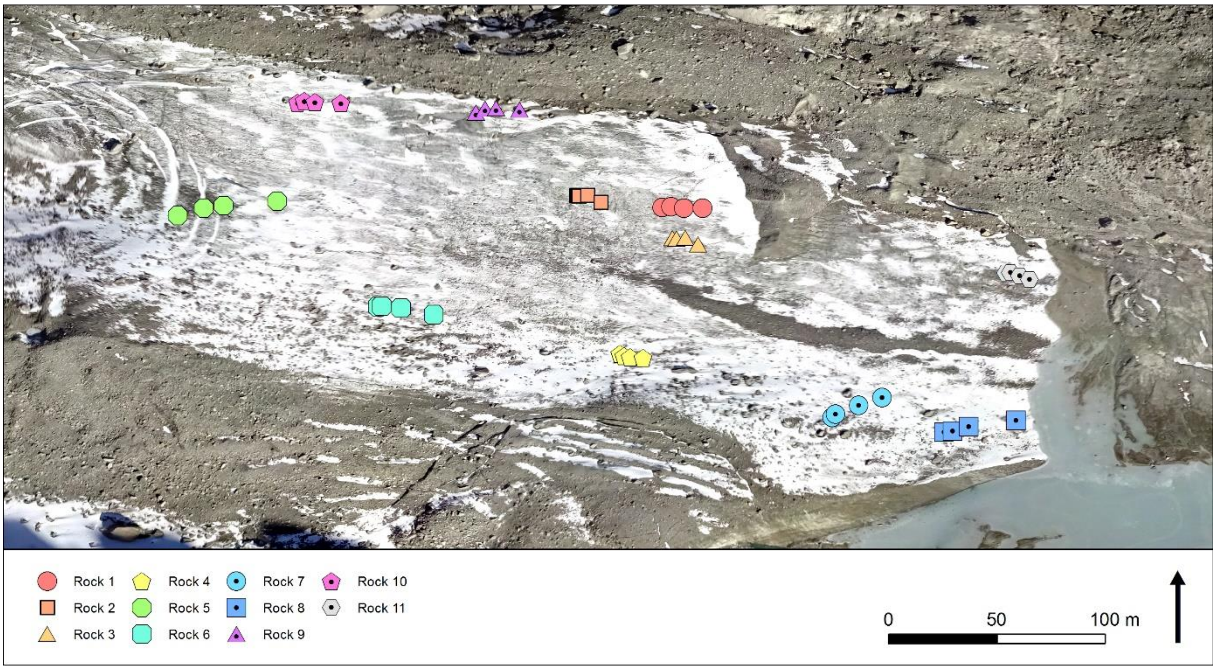

Fig. 58: Locations of 11 rocks on the tongue's surface between July 2014 and October 2017.

Most observed rocks do not travel in a straight line, but rather feature a curved travel path. Rocks 2, 3, 4, 6 and 11 initially move towards the East and later change towards South-East, whereas rocks 5, 7 and 8 tend to move to the North-East. Rocks 1, 9 and 10 travel eastwards without noticeable changes in their direction.

Figs. 63 and 64 show the relations between the rock surface area and their distance traveled as well as their distance to the terminus and their distance traveled. There appears to be a correlation between the area of the rock surface and the distance covered by the rocks in the observed time period: The larger the rock's surface is, the longer is its distance traveled. This suggests that the velocities of the rocks depend on their size and not only on the flow of the underlying ice. The rocks' distances from the terminus, on the other hand, do not seem to correlate in any way with their distances traveled.

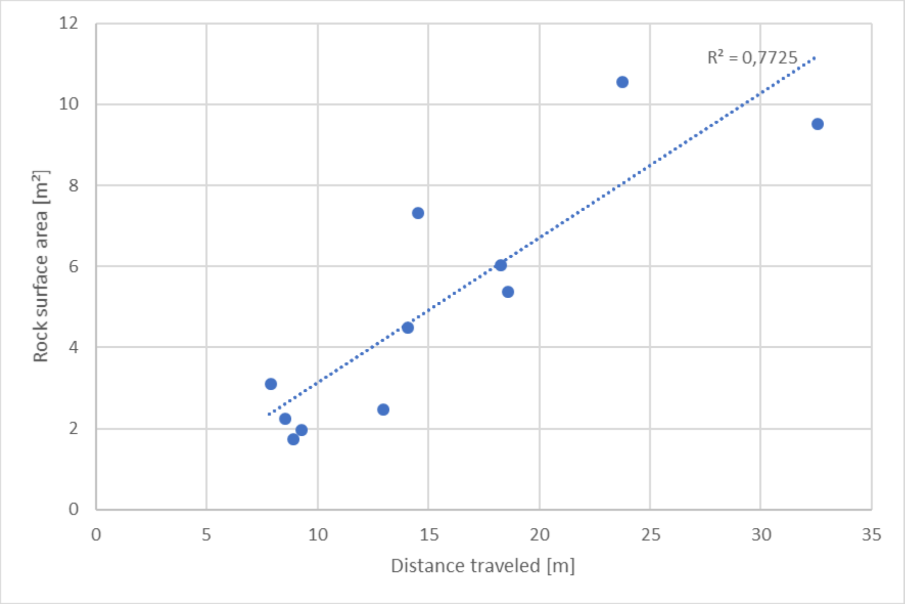

Fig. 59: Distances the rocks traveled plotted against their surface areas. The R^2 value of 0.77 suggests a correlation between the surface area and the distance traveled.

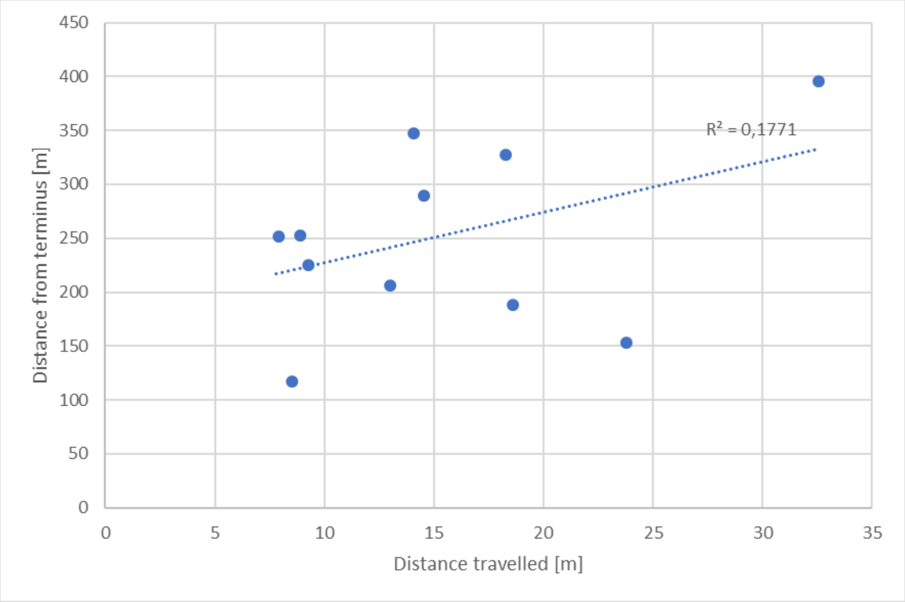

Fig. 60: Distances the rocks traveled plotted against their initial distances from the terminus. The R^2 value of 0.18 suggests no correlation.

5.8. Ground penetrating radar

Between July 2014 and July 2017, five groups of students have conducted measurements on the glacier tongue using GPR (Hafner et al. 2014, Hasler et al. 2014, Burkhalter et al. 2015, Aus der Au et al. 2016, Büchler et al. 2017). In the following, their results are briefly summarized.

The paths the students took on the glacier tongue with the GPR device are visualized in Fig. 65. The exact routes Büchler et al. (2017) measured could not be reconstructed, as there was not enough information available in the field report.

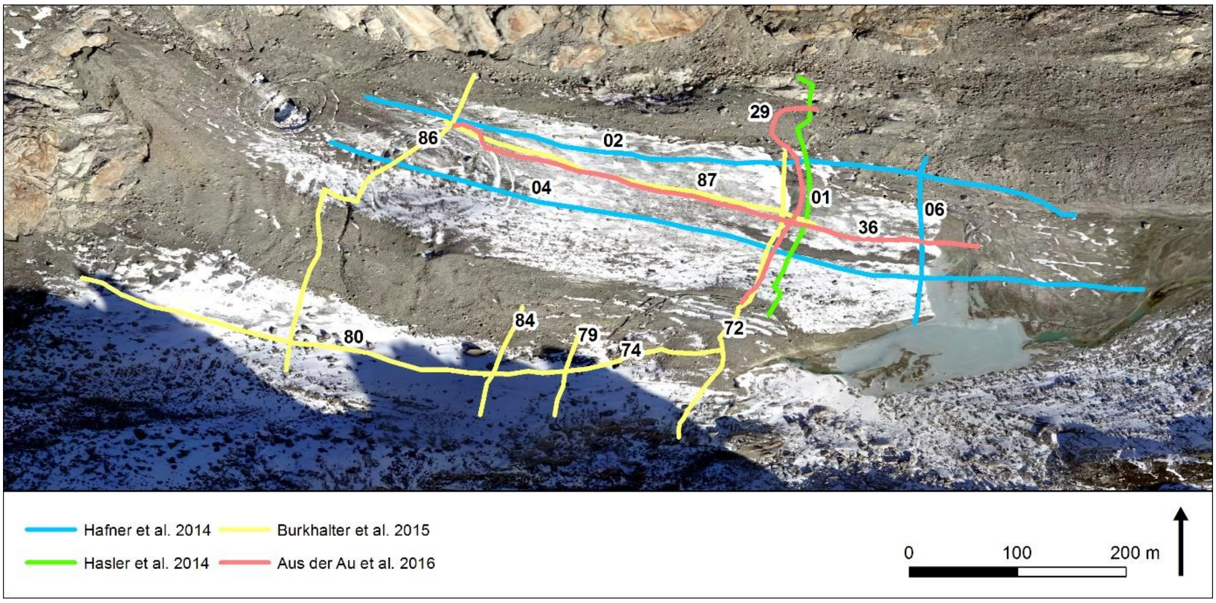

Fig. 61: Paths the students from the course GEO 411 took with the GPR device.

All groups who created at least one longitudinal profile on the lower glacier tongue concluded that the ice thickness continually increases towards the upper tongue. This can be identified in the radargrams, as the transition between glacier ice and underlying bedrock or sediment is clearly visible (Fig. 66). According to Hafner et al. (2014), the maximum thickness of the ice lies just below the area of the lower depression. This observation corresponds with the one by Burkhalter et al. (2015), who identified the thickest ice mass in the same area. Further, Hasler et al. (2014), Hafner et al. (2014) as well as Aus der Au et al. (2016) find that the medial moraine shows substantially thicker ice masses than the lateral moraine. By comparing GPR data from previous years, Aus der Au et al. (2016) further observed that the lateral moraine lost significantly more ice mass than the medial moraine.

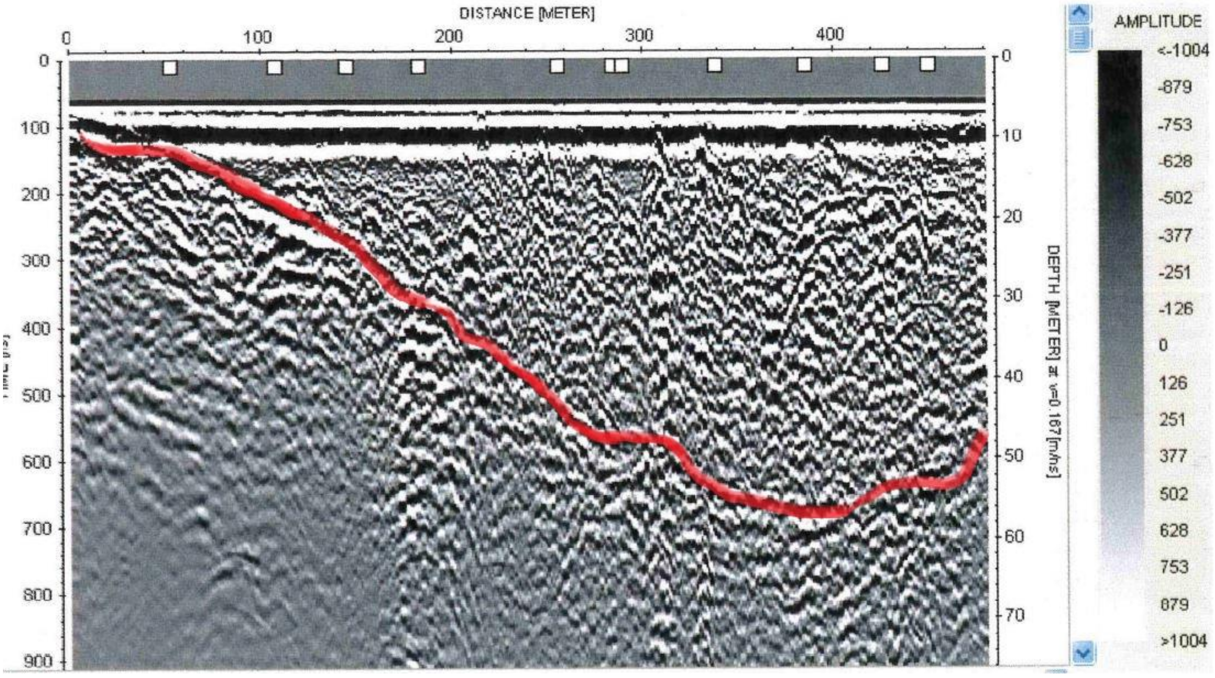

Fig. 62: Radargram of path 02 by Hafner et al. 2014. The path follows uphill and the glacier bed is marked in red.

Büchler et al. (2017) describe the presence of a layer within the ice in the lower glacier tongue at an angle of about 20–25° (Fig. 67). They identify the layer as a 10 cm thick sediment layer, which lies between the ice surface and the glacier bed. Moreover, they conclude that the diffuse radar signal in the upper part of the tongue is likely the result of an air chamber within the ice. The subsidence of the ice surface and the concentric crevasses further support this argument.

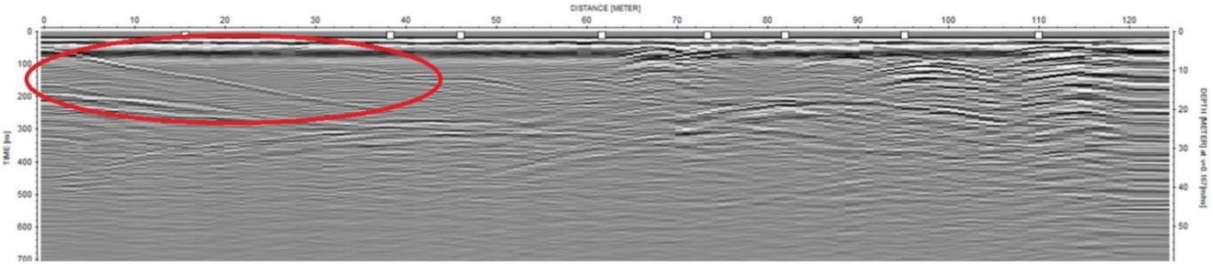

Fig. 63: Radargram of path 72 by Büchler et al. 2017. The layer within the ice is marked in red. There was not enough information in the field report to reconstruct the exact path on the orthophoto.

6. Discussion

In order to answer the previously defined research questions, the above presented findings are discussed in the following chapter. Uncertainties regarding the tracking of the supraglacial rocks are discussed and the calculated flow velocity of the tongue is compared to other glaciers in the Alps as well as calculations from the field reports. The ablation measurements are put in context with elevation changes extracted from the difference images and the possible presence of dynamic replacement is discussed. Further, five glacial features are discussed separately, including their formations, developments and influences on the glacier tongue's geometry. Rather than adding the aspect of supraglacial debris as a separate section, its influence is included throughout the discussion as it affects the majority of the studied glacial processes.

6.1. Ice flow velocity

The flow velocity of a glacier provides insights into its dynamic state and its response to climate signals (Stocker-Waldhuber et al. 2018). It is therefore a valuable parameter when assessing a glacier's development and allows to draw conclusions about the underlying processes leading to an acceleration or deceleration of the ice flow.

The results of the feature tracking showed large differences between the velocities of the observed rocks. This shows that the ice flow is not the only factor affecting the supraglacial rocks' movements. In addition to the ice flow, sliding of the rocks on the ice is responsible for their displacement, especially when they produce glacier tables. Glacier tables form when the ice under a rock melts slower than the surrounding ice surface, since the rock shields the ice from solar radiation. The result is a rock elevated on a stump of ice (Fig. 68). At some point, the glacier table becomes too instable to support the rock causing it to slide off. Schwendener (2017) found that most observed rocks in the Swiss Alps tend to slide towards the South-East. This happens due to the solar radiation, which is strongest in the morning since Alpine weather tends to be cloudy in the afternoon. Five out of eleven observed rocks on the Tiefenglacier's tongue changed their direction towards the South-East, which may have been caused by the continuous formation and sliding off glacier tables.

Fig. 64: A rock on a glacier table on the upper glacier tongue.

The movement of glacier table forming rocks also depends on their shape and size: flat rocks usually cover the underlying ice better and slide off the tables, whereas cylindric or round rocks tend to tip over (Schwendener 2017). Furthermore, Schwendener (2017) observed that only rocks with a surface larger than 40x40 cm tend to form a base of ice underneath. It can be assumed, therefore, that all observed rocks on the Tiefenglacier had the potential to form glacier tables, as they all have a surface of at least 1.8 m2.

The correlation between rock surface and distance traveled supports the idea that glacier tables are involved in the movement of the rocks, as larger rocks seem to have a higher chance of forming glacier tables. However, the surface ice melt and refreezing of melt water on the ice surface causes its texture to change continuously, possibly leading to the displacement of the rocks without glacier tables. Additionally, since the gradient of the ice surface and the ice flow are directed towards East-South-East, it cannot be determined with certainty whether the rocks’ change of direction is a direct result of glacier tables.

Rock #4 traveled the shortest distance in the observed time period. Although sliding on the ice and glacier tables might have contributed to its movement, its velocity best represents the velocity of the ice flow. With a maximum average velocity of 2.4 m/a, the tongue of the Tiefenglacier is almost, if not fully, stagnant. The fact that no correlation between the rocks’ distances to the terminus and their distances traveled could be observed suggests that the tongue moves approximately at a uniform speed, which does not depend on the location. The remaining surface velocity is probably mostly caused by basal sliding, as internal ice deformation requires pressure from an overlying ice mass, which is melting at a fast rate.

The fact that most rocks show significantly shorter travel distances between July 2014 and July 2015 might be a result of the low air temperatures during the summer of 2014. Assuming the majority of the rocks' movement is caused by glacier tables and sliding, the low air temperatures reduce their velocity, as the formation of glacier tables and the production of melt water is reduced as well.

Other glaciers in the Swiss Alps, such as the Morteratschglacier or the Rhoneglacier, show similarly slow flow velocities near the terminus, caused by the rapid mass loss in the last few decades (Nishimura et al. 2013, Zekollari et al. 2013). The thinning of the glacier ice, especially in the ablation zones, leads to smaller ice masses reaching the terminus, effectively slowing it down. Significant deceleration of the ice flow can happen within just a decade, as ice flow velocity measurements on a disintegrating glacier in the Tyrolean Alps showed (Stocker-Waldhuber et al. 2017). The rapid loss of ice mass coupled with the formation of glacial features such as supraglacial lakes and cliffs are mentioned as driving forces for the slow down.

DGPS measurements conducted by a group of students on the field course in July 2015 suggest that the surface ice on the tongue was moving at a velocity between 12.6 and 26.8 m/a (Mösch et al. 2015). These results could not be confirmed, however, as the maximum velocity of the observed rocks was 10 m/a at rock #5, which includes displacement by sliding. It is possible that the high velocities measured with the dGPS were caused by errors. Mösch et al. (2015) mention uncertainties such as the great distance to the next ground control station in Oberalp, or the fact that the velocities were calculated by extrapolating a two-day experiment conducted in summer over an entire year.

6.2. Ablation

The comparison of the surface ablation data with the surface elevation change shows that between July 2014 and July 2015, most of the observed elevation change can be attributed to surface ice melt. Solely the area around stake 12 has experienced additional downwasting, which is likely the result of the surface subsidence caused by the cavity near the stake.

The calculations show that in the following year, the surface at all three stakes has lost more elevation than the ablation data can explain. Given that the elevation loss increases towards stake 12, it can be assumed that the additional downwasting is again caused by the funnel-shaped depression farther upstream. As the cavity within the ice is expanding, its influence on the ice surface reaches farther, reducing its stability and causing it to sink in.

Surprisingly, all stakes show more ablation than elevation change between July 2016 and October 2017, suggesting an incident of dynamic replacement. However, since the tracking of the supraglacial rocks revealed that the glacier tongue has been almost stagnant for at least three years, it is rather unlikely that the lifting of the ice surface is caused by large amounts of ice flowing downstream. Instead, the apparent dynamic replacement might be the result of some other form of glacial dynamics. Due to the fact that no other indications of ice movement have been found that could explain the lifting of the ice, it is not possible to tell with certainty what the underlying cause is with the available data. It has to be noted that the ablation values for stakes 10 and 11 have been calculated by linearly extrapolating the ablation measurement at stake 12. Furthermore, the presence of snow in the DSMs of July 2015 and 2016 might lead to inaccurate elevation values, which affects the comparison with the ablation data. These data are therefore subject to an unknown degree of certainty and might not fully represent the real amount of ablation.

6.3. Glacial features

The five glacial features, on which the focus is laid on in this study, are discussed in more detail in this section with reference to the supraglacial debris cover. The discussion is structured to focus on their formations, developments and influences on the tongue's geometry, according to the research questions 2 and 3.

6.3.1. Lateral Moraine

6.3.1.1. Formation

The lateral moraine of the Tiefenglacier's tongue was formed by debris falling onto the outer rim of the glacier in the accumulation area, which then got transported along the ice flow to the tongue. The steep rock walls on the north-eastern end of the accumulation area ensure a steady flow of debris falling onto the glacier. Nowadays, the upper lateral moraine is still fed by the rock walls to its North. The lower moraine, however, is too far away from the rock walls to still receive new debris, as a small valley filled with debris separates the moraine from the walls. This small valley might be the result of years of melt water flowing through melting the ice, which would explain the sand deposits in this area as well.

The shape of the moraine is the result of the insulating properties of the overlying debris. Thin debris covers in the range of around 1 cm may enhance the melt of the ice underneath due to the warming up of the darker colored debris (Østrem 1959). The debris cover on the lateral moraine, however, is generally at least 3 cm thick and in most areas thicker. The comparison of the melt rates of debris-covered surfaces with debris-free surfaces has shown that covers above a thickness of 5 cm consistently decrease the ice melting underneath (Chapter 5.6.2.). It can therefore be expected that the debris cover on the entire lateral moraine has an insulating, rather than a melt enhancing effect. The slower surface melt caused by this insulation leads to the formation of the protruding shape of the moraine, as illustrated in Fig. 69.

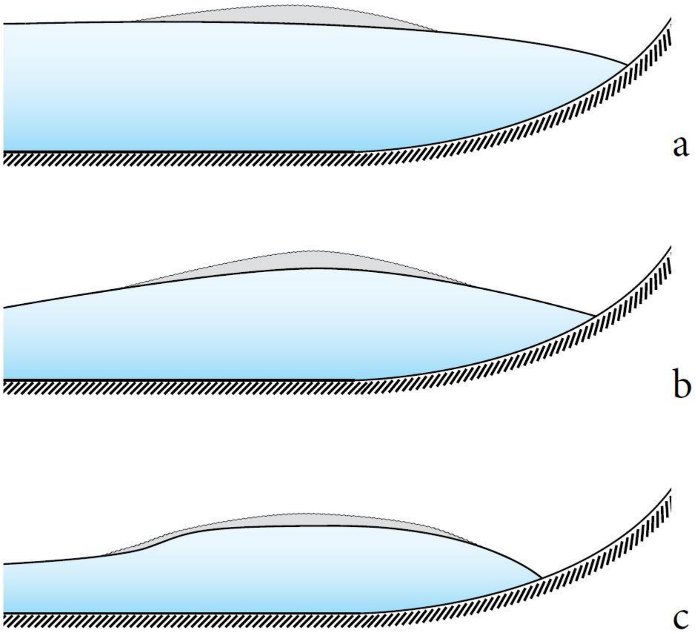

Fig. 65: Conceptual representation of the formation of the lateral moraine's shape. (a) Part of the ice is covered by debris. (b) The debris layer insulates the underlying ice, decreasing surface ablation. (c) Over time the debris-covered part of the moraine stays elevated.

6.3.1.2. Development

Fig. 70 shows the extents of the moraine between July 2014 and October 2017. The outlines of its state in July 2014 do not reach the upper end of the moraine as the orthophoto only covers the lower two thirds of the tongue. The lower end of the moraine still containing an ice core has retreated at about the same rate as the terminus. The extent of the remaining moraine does not seem to follow any particular trend. This is most likely due to the fact that the drawing of its outlines is a rather subjective task, because

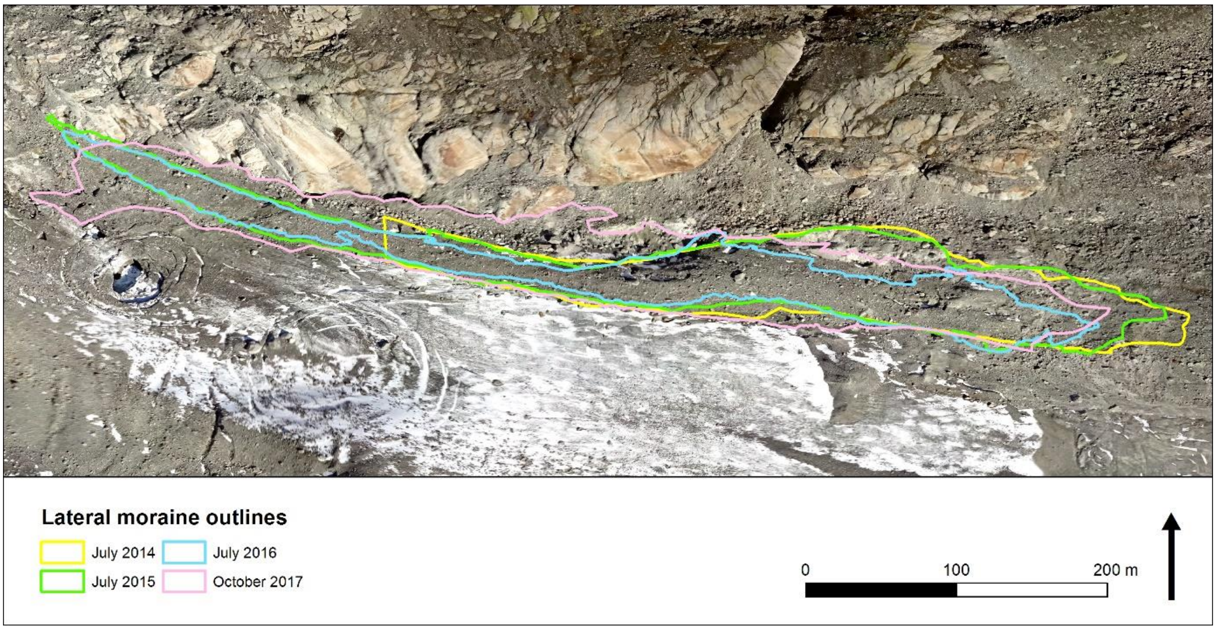

Fig. 66: Outlines of the lateral moraine's extents between July 2014 and October 2017.

moraines often have fluent transitions to the surrounding areas. Further, the presence of snow in some of the orthophotos made it more difficult to estimate the moraine’s outlines.

The upper half of the moraine experienced noticeably more downwasting than the lower half. This observation could be made using the point-based elevation differences and was confirmed by looking at the difference images. On average, the upper end of the moraine sunk in around 10 m more than the lower end, although the debris cover is roughly equally thick in both areas. A possible explanation for this is the proximity of the upper moraine to the depression of the ice surface marked by the concentric crevasses on the upper glacier tongue. The structure of these crevasses combined with the observed large elevation changes suggest the presence of an air-filled cavity beneath the ice surface, which is likely to expand due to the steady stream of melt water. The exact dimensions of the cavity remain unclear, yet it is possible that it stretches close enough to the moraine to cause it to sink in as well. Another reason for the observed difference in the elevation changes might be an enhanced surface ice melt on the upper half of the moraine, but there are not enough ablation stake measurements on the lateral moraine to confirm this. However, it is rather unlikely that this difference can be explained by varying surface melt rates alone, because, as mentioned above, the composition of the supraglacial debris is very similar on the upper and lower lateral moraine.

The lower lateral moraine shows the greatest variety of debris cover types. On the orographically left side to the lower moraine (Category 6 in the debris distribution overview), there are some rounded rocks, caused by fluvial or subglacial abrasion. Large deposits of sand suggest that melt water streams used to flow through this area, probably abrading the rocks in its path. Visible flows of water leaving the glacier near the terminus as well as fresh looking deposits of sand and silt indicate the presence of a current

Fig. 67: Silt and sand deposits at the lower end of the lateral moraine indicate the presence of an en- or subglacial stream.

sub- and/or englacial stream (Fig. 71). This melt water, probably originating from the large stream visible through the collapsed ice surface on the upper tongue, enhances the ice melt from within the moraine and thus accelerates its disintegration.

Comparing the downwasting rates of the lateral moraine with the rates of the debris-free surface of the glacier tongue, it becomes evident that the debris-cover on the moraine has an insulating effect. Between July 2015 and October 2017, the surface of the upper and lower lateral moraine sunk in by -15.2 m and -8.9 m, respectively. The debris-free surface, on the other hand, showed an elevation loss of -16 m and -9.9 m. Due to the slower downwasting rate of the lateral moraine, it can be expected that the moraine will keep growing taller relative to the debris-free ice surface until it reaches the bedrock.

6.3.1.3. Influence on glacier geometry

Since the lateral moraine lies on the northern edge of the tongue next to the steep rock walls and shows little dynamic changes in its lower half, its influence on the remaining glacier tongue is limited. The debris cover on the uppermost part of the moraine might stabilize the ice surface underneath: While the cavity within the ice presumably keeps growing, the debris on top shields the ice from heat and radiation, thus delaying a possible collapse of the surface near the moraine.

It is possible that parts of the moraine will be the last remainder of the glacier tongue due to its insulating debris cover once the rest has melted away. The medial moraine will probably exist for a while longer as well, but because of its great number of crevasses and partly hollow structure, parts of it might eventually collapse (see Chapter 6.3.2.).

6.3.2. Medial moraine

6.3.2.1. Formation

Medial moraines are typically formed when two glaciers meet, and two lateral moraines are pushed together, leaving a band of debris in the middle of the newly formed glacier. Ice flowing from the Dammazwillinge and from the Galenstock, which is separated by protruding bedrock, meets just above the Tiefenglacier’s tongue. The supraglacial debris originating from the bedrock then forms its medial moraine (Fig. 72). Its protruding shape can again be explained by the insulating effect of the supraglacial debris, which prevents the ice from melting at the same rate as debris-free ice.

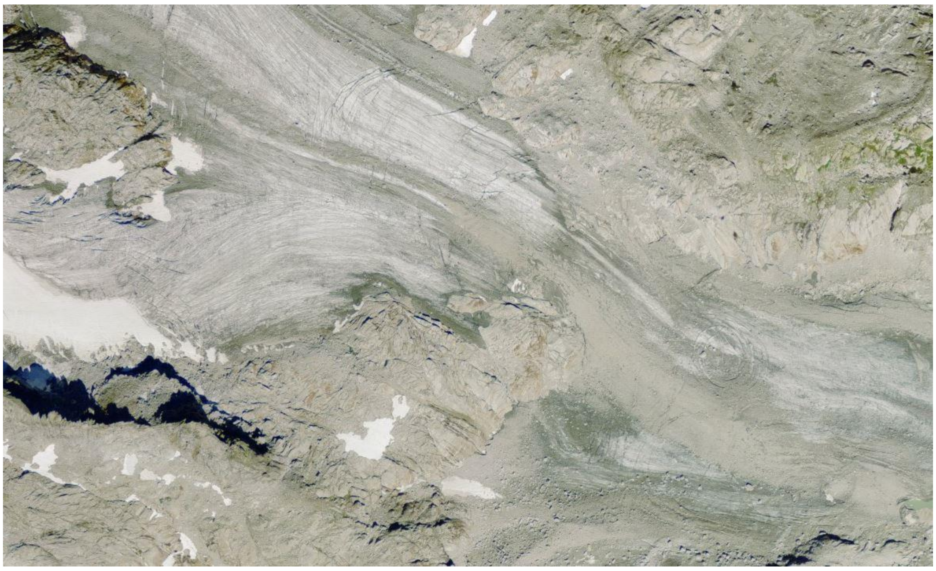

Fig. 68: Two ice streams joining together form the medial moraine. (Background: SWISSIMAGE, swisstopo)

6.3.2.2. Development

The most prominent visible changes of the medial moraine in the observed time span occurred in its lower end (Fig. 73). Its “panhandle”, which measured a few hundred meters in July 2014, became gradually shorter and disappeared completely by October 2017. This happened because of the extreme melt rates observed on the ice cliff, which used to stretch along the southern side of the moraine’s thin extension. As the cliff lost large amounts of ice mass due to its direct exposure to the sun, it gradually moved towards North-East, reducing the moraine’s surface until the cliff reached the main body of the tongue.

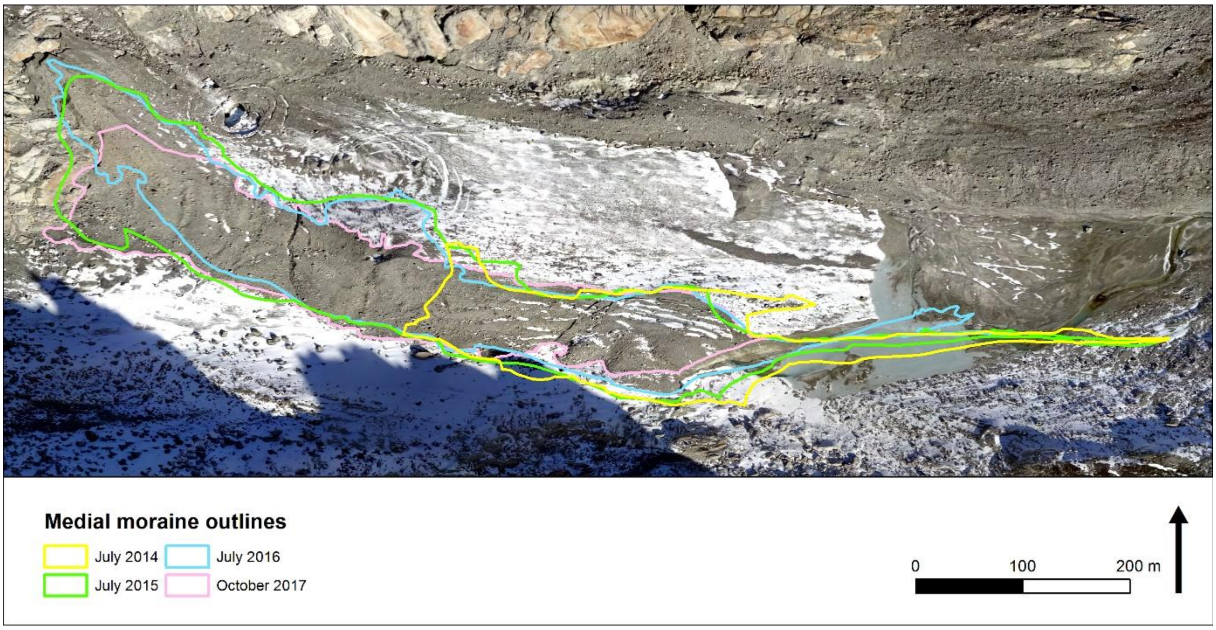

Fig. 69: Outlines of the medial moraine’s extents between July 2014 and October 2017.

The outlines of the upper medial moraine are, again, a rather subjective approximation due to clouds and snow covers visible in the orthophotos. Nevertheless, it can be stated that its extent did not change considerably.

The longitudinal crevasses on the orographically left side of the lower moraine became more prominent over time and are clearly visible in October 2017. Usually, longitudinal crevasses form in areas where the glacier becomes wider due to tensile stress acting on the ice and tend to be directed in flow direction towards the glacier's side (van der Veen 1999). In the newest orthophoto of October 2017, no widening of the glacier in this area can be observed. In July 2014, however, the tongue's width slightly increased further downstream, suggesting that the crevasses might have formed before, when the increase was more prominent.

The improved visibility of those crevasses in the newest orthophoto can be attributed to the formation of crevasse-fill ridges (Friello and Hanson 2015). The initial crevasses, which had narrow openings and were barely visible, were slowly filled with debris falling inside from the ice surface. As the ice surface surrounding those crevasses experiences downwasting and sinks in, the accumulated heaps of debris inside the crevasses stay slightly elevated compared to the surface surrounding them due to their insulating properties and form debris ridges (Fig. 74). By overlaying orthophotos from July 2014 and October 2017, it becomes clear how the crevasses become ridges and vice versa (Fig. 75).

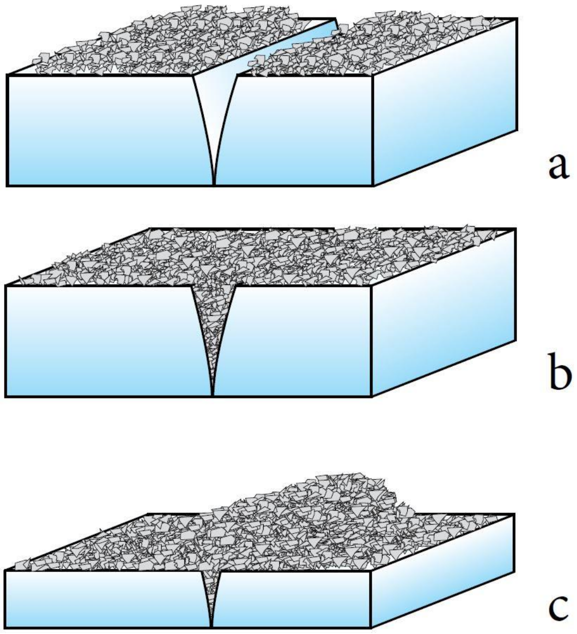

Fig. 70: Conceptual representation of crevasse-fill ridges forming. (a) A crevasse forms in debris-covered ice. (b) Debris falls into the crevasse, filling it completely. (c) As the surrounding ice surface experiences downwasting, the heap of debris, which was inside the crevasse, stays elevated.

Fig. 71: Overlay of orthophotos from October 2017 (left) and July 2014 (right). The narrow crevasses visible in 2014 (black stripes) become crevasse-fill ridges in 2017 (brown stripes).

Surrounding these crevasse-fill ridges, there is a deep crevasse in the shape of a semicircle. The area inside this semicircle has sunken slightly in, which is also visible in the difference image. This phenomenon is similar to the one observed at the depression surrounded by the concentric crevasses on the upper glacier tongue, suggesting that there are one or more air-filled cavities beneath the lower medial moraine. The fact that large amounts of melt water exit the glacier beneath the ice cliff and the lower medial moraine supports this assumption, as the water would melt the ice inside the moraine and thereby creating a cavity. Usually, the ice flow as well as lithostatic stress close cracks and crevasses in the ice before they can grow into such cavities (Nath and Vaughan 2003). However, since virtually no ice flow is present, and the lithostatic stress keeps decreasing due to the decreasing mass of the moraine, crevasses inside the ice are able to continuously grow. The stream of melt water inside the medial moraine might lead it to eventually collapse in the future.

Slightly downstream of the moraine's peak there is a band of increased downwasting visible in the difference image. This increased elevation change was already present between July 2014 and July 2015 and has increased since. It is possible that this is caused by an en- or subglacial stream originating from the large stream visible through the collapsed ice surface on the upper glacier tongue. The stream would destabilize the ice surface above, causing it to sink in. The additional sinking of the lower medial moraine caused by those streams could explain why the downwasting along the medial moraine is more evenly distributed than on the lateral moraine, as observed using the point-based elevation differences.

On average, the upper medial moraine has experienced a downwasting of -12.2 m between July 2015 and October 2017, whereas the lower moraine experienced -10.1 m. The elevation change is therefore noticeably more evenly distributed than on the lateral moraine (-15.2 m, -8.9 m). The lower medial moraine shows almost the same amount of elevation change than the lower debris-free tongue (-9.9 m) despite the thick insulating debris cover. This is presumably the result of the cavities within the lower moraine and the resulting subsidence marked by the crevasse in the shape of a semicircle in Fig. 76, which accelerates its disintegration.

Fig. 72: Longitudinal crevasses on the lower medial moraine. A larger, deeper crevasse in the shape of a semi-circle is visible on the left.

6.3.2.3. Influence on glacier geometry

The medial moraine covers the largest area of all studied glacial features and therefore has a significant influence on the tongue. The upper moraine shows noticeably less dynamic activity than the lower moraine: Compared to its lower half, the upper medial moraine seems to be stable with little elevation changes and just a few crevasse formations. The depression of the ice surface to its North has not yet affected its structure in an observable way and is therefore expected to remain this way for a while longer. Like the upper lateral moraine, the thick, insulating debris cover of the upper medial moraine stabilizes its ice core, prolonging its disintegration.

The accelerating sinking in of the lower medial moraine is a sign of its destabilization, which might lead to its collapse. If it does collapse, the rate of the mass loss in this area will be even greater, leading to a faster retreat of the tongue.

6.3.3. Sediment hill

6.3.3.1. Formation

The first visible sign of the sediment hill’s formation is visible in the orthophoto of July 2015, where a small patch of debris appears on the ice. It can be ruled out, therefore, that the hill was formed by debris from the lateral moraine falling onto the ice, as the ice between the hill and the moraine remained debris-free. Further, the sediment forming the hill consists mostly of sand, rounded cobbles and a few angular small boulders, while the sediment of the lateral moraine is noticeably more angular and larger in size. The rounding of the debris suggests that the sediment originates from within the ice or the glacier bed, where abrasion of the debris takes place.

The most probable explanation for this phenomenon is the presence of a sediment layer within the ice of the tongue, which gets uncovered as the surrounding ice melts. Since the ice is almost stagnant, the sediment layer stays still, but the downwasting of the surrounding ice surface gives the illusion of the hill growing taller. GPR measurements of Büchler et al. (2017) support this finding, as they detected a layer within the ice upstream of the hill, which probably consists of sediment, at an angle of about 20–25°.

Moll (2012) as well as two student groups from the excursions found the existence of an overdeepening starting at the lower end of the lower concentric crevasses. The ice flow following an overdeepening is typically emerging, which would explain the angled, emerging nature of the sediment layer. The origin of the sediment layer might be a moraine or a part of one, which submerged in the ice in the accumulation zone and emerged in the ablation zone. Plucking and abrasion at the steep back wall of the overdeepening may have added sediment, which was subsequently rounded by further abrasion.

6.3.3.2. Development

The sediment hill has grown mainly between July 2016 and October 2017 and has roughly maintained its initial shape (Fig. 77). Although Büchler et al. (2017) concluded that the sediment layer in the ice has a thickness of around 10 cm, debris thickness measurements conducted in October 2017 on the western side of the hill showed debris thicknesses of 13 and 40+ cm. These variable thicknesses are likely the result of the debris sliding off steep walls and accumulating at more even surfaces and near the hill’s bottom. The sediment hill’s peak, which has the steepest surfaces, thus shows relatively thin debris covers. Due to the variability of the debris thickness and the constant movement of debris, it is not possible to precisely determine the thickness of the layer in the ice without any further measurements.

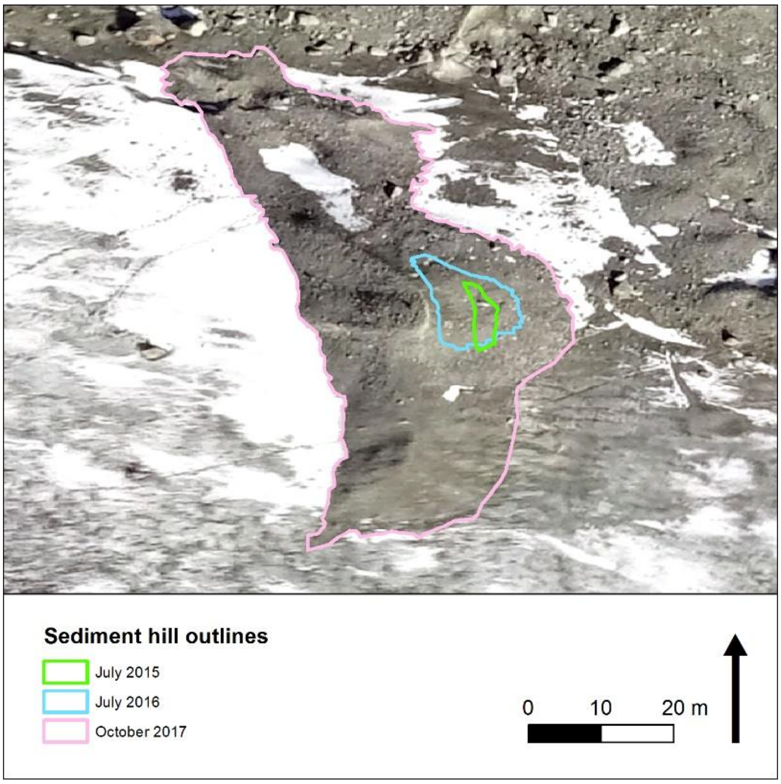

Fig. 73: Outlines of the sediment hill's extents between July 2015 and October 2017.

On the eastern side of the hill's ridges, there are steep surfaces covered by a layer of wet sand (Fig. 78). These surfaces are directly exposed to the sun during mornings, and the wet sand suggests that the ice underneath is melting. As the ice melts, the surface becomes steeper, allowing more debris to slide off, which again exposes more ice and leads to a positive feedback. This surface's behavior is similar to the one observed at the ice cliff at the southern glacier terminus, but with slower melt rates due to the sand still covering them. No debris thickness measurements have been conducted on these surfaces, but it can be assumed that the sandy layer is not thin enough to enhance the ice melt underneath. The resulting

Fig. 74: The eastern side of the sediment hill's peak is covered by wet sand.

retreat of the hill's peak gives the illusion of the peak wandering westwards, which could be observed in the profiles.

6.3.3.3. Influence on glacier geometry

Due to the generally thick debris cover observed on the sediment hill, it likely prolongs the disintegration of the tongue slightly.

According to the GPR measurements of Büchler et al. (2017), the sediment layer in the ice stretches 40 m stream upwards until it meets the glacier bed near the lower end of the overdeepening. Once the entire layer of sediment is uncovered, the ice underneath will probably melt at a slower rate than the debris-free ice, resulting in a moraine-like structure with an icy core.

6.3.4. Ice cliff

6.3.4.1. Formation

The formations of most ice cliffs are caused by three main processes: First, ice can calve into supraglacial lakes, leaving steep slopes of clean ice exposed. Second, collapses of englacial voids may lead to the subsidence of the ice surface. Third, supraglacial debris can slide off angled slopes, exposing the underlying ice (Benn et al. 2012, Sakai et al. 2002).

The large ice cliff at the southern end of the terminus was most likely formed by the latter process. The glacier ice used to cover parts of the steep rock wall to the South of the cliff. The warm adjacent rock and debris may have promoted the formation of the cliff by enhancing the melt of the ice closer to the ground, creating a steeper slope. Once the slope is steep enough, debris begins to slide off, exposing the underlying ice. The southern exposed aspect of the cliff favors high melt rates, further making the cliff steeper, which leads to a positive feedback.

6.3.4.2. Development

The extent of the ice cliff has decreased significantly during the observed time period in both length and width (Fig. 79). The orientation of the cliff turned from W-E in 2014 to WSW-ENE in October 2017. This is the result of the glacier terminus' retreat, which only left the western part of the cliff intact.

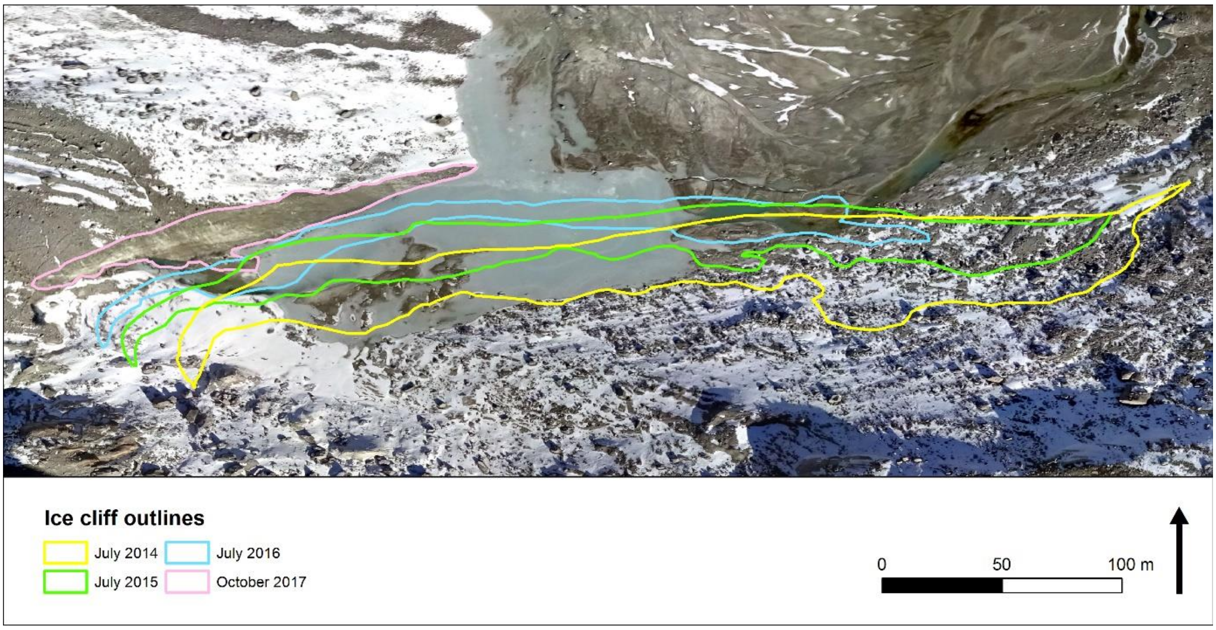

Fig. 75: Outlines of the ice cliff's extents between July 2014 and October 2017.

The extreme elevation changes observed in the difference images are a result of the cliff's horizontal movement. As its surface is directly exposed to the sun, it experiences high losses of ice mass, causing it to melt further into the ice. Since the cliff's surface is rather steep and the difference images show changes in vertical elevation, a small horizontal movement of the surface is enough to create high vertical elevation changes.

In order to compare the backwasting rate of the cliff with the downwasting of the debris-free ice surface on the remaining tongue, the backwasting measured perpendicular to the cliff's surface is the most suitable. For this, the rates measured at Profile 1 of the cliff is used, as it stays intact until the end of the measurement period and therefore best represents the backwasting rate. Between July 2015 and October 2017, the cliff's surface experienced a backwasting between -20.5 – -23 m, which amounts to an average of -9.1 – -10.2 m/a. The average downwasting rate of the debris-free ice surface, on the other hand, is -4.4 m/a on the lower tongue and -7.1 m/a on the upper tongue. These numbers demonstrate how the cliff's direct exposure to the sun significantly increases its melt rate and thereby accelerates the tongue's disintegration.

The maximum backwasting rates occur in different years for different profiles and do not correlate well with the mean annual temperatures (2015 being the warmest year and 2016 the coolest). This underlines the importance of the cliff's aspect and geometry, which appear to affect its melt rates more than the mean temperatures.

In all orthophotos, the cliff is covered by a thin layer of sand. This may increase the already high melt rates, as a thin layer of debris cannot efficiently insulate the underlying ice but enhance the melt due to its low albedo (Oerlemans et al. 2009, Østrem 1959). The bottom of the cliff experiences very high melt rates as well as it reaches into the proglacial lake.

Buri and Pellicciotti (2018) found that southerly facing supraglacial ice cliffs on debris-covered glaciers in the northern hemisphere are usually very short-lived compared to northerly facing ones and contribute very little to the overall ablation. This is due to the large amount of solar radiation they receive, which makes them flatten out and be buried in debris again much faster. This development could be observed at the eastern end of the cliff (Profile 6), where it progressively shrunk until only a small remnant was left before the terminus further retreated. The western end of the cliff, however, still exists and does not seem to see any changes in its gradient. The persistence of this cliff could be explained by the proglacial lake causing high melt rates, which makes sure that the bottom of the cliff retreats at an equally high rate as the top. However, the gradient of the western cliff remained stable even before the formation of the melt water lake. The continuous formation of crevasses on the cliff in the previous years led to the break-off of ice, which left steep flanks of ice behind. Further, the cliff is located at the terminus of the glacier tongue, where its underside touches either bedrock or deposited sediment, rather than glacier ice. This, as well as the fact that the glacier tongue is almost stagnant, gives the cliff a stable ground to move across at a relatively high velocity.

The Profiles 4–6 show an increase of the ground surface elevation at the bottom of the cliff in October 2017. In Profiles 5 and 6, the elevation has already started in July 2014 and continued to the present day. Most of the elevation can be explained by the deposition of sediment by melt water streams in the glacier forefield as well as the formation of the melt water lake, whose surface lies higher than the deposited sediment underneath. The rock wall to the South of the glacier seemed to have experienced a constant increase in elevation as well. This is most likely the result of loose debris falling from steeper walls above, or the presence of snow.

6.3.4.3. Influence on glacier geometry

The glacier tongue has lost substantial amounts of ice due to the cliff’s high melt rates. The resulting retreat has made room for the proglacial lake, which further promotes increased ice loss. Moreover, the fast retreat of the cliff has created a cave-like structure at the western end of the cliff, which might collapse as the continuing mass loss destabilizes it (Fig. 80).

Fig. 76: A cave-like structure was formed on the south-eastern end of the ice cliff.

As long as the cliff keeps a certain steepness for the debris to slide off, it will move towards the North-West, further resulting in relatively high mass losses. Considering the melt water channels and the probable existence of a cavity within the lower medial moraine, the ice cliff might accelerate the collapse of the moraine. The collapse of the roof of englacial voids may lead to the formation of smaller ice cliffs, which further enhances the ice melt (Kirkbride 1993).

6.3.5. Funnel-shaped subsidence

6.3.5.1. Formation

The orthophoto of July 2015 is the first one in which the bundle of crevasses in the upper half of the tongue are visible. By then, only the lower depression was recognizable as such due to the concentric nature of the crevasses. The area in which the upper depression was going to form only showed a few longitudinal crevasses.

The concentric shape of the crevasses is the result of a cavity within the ice, which leads to subsidence of the overlaying ice masses and destabilization of the ice surface. Once a cavity is large enough, the ice surface can no longer support itself and breaks in, which happened to the upper depression between July 2016 and July 2017 (personal communication, A. Vieli, 14.05.2018).

The englacial cavities may have started out as a subglacial lake, whose water level lowered and caused a subsidence of the surface ice (Magnússon et al. 2007). The subglacial lake is a result of englacial and subglacial melt water streams, which efficiently melt the ice from within the glacier tongue (Stocker-Waldhuber et al. 2017). These streams possibly started out as R-channels at the glacier bed, whose size are increased by viscous heating and decreased by internal ice deformation (Röthlisberger 1972). Since the tongue has been almost stagnant for at least three years, there is only little internal ice deformation. Further, the driving stress controlling the ice flow keeps decreasing due to the continuous reduction of ice thickness and surface slope. Without ice deformation limiting the expansion of subglacial channels, they can flow at atmospheric pressure and increase in size, which accelerates the ice melt and can eventually lead to the formation of subglacial lakes.

6.3.5.2. Development

The center of the lower subsidence has moved around 20 m downstream between July 2015 and October 2017, suggesting that the cavity has grown larger (Fig. 81). The relocation of the center could also be the result of the crevasses moving along the ice flow. However, due to the formation of new crevasses and limited visibility of them because of snow and debris, it is not possible to match the crevasses from the older orthophoto with the newer ones with a reasonable degree of certainty. Further, the results from Chapter 6.1. show that the ice flows with a maximum velocity of 2.4 m/a, which would not suffice to explain the observed displacement of the center.

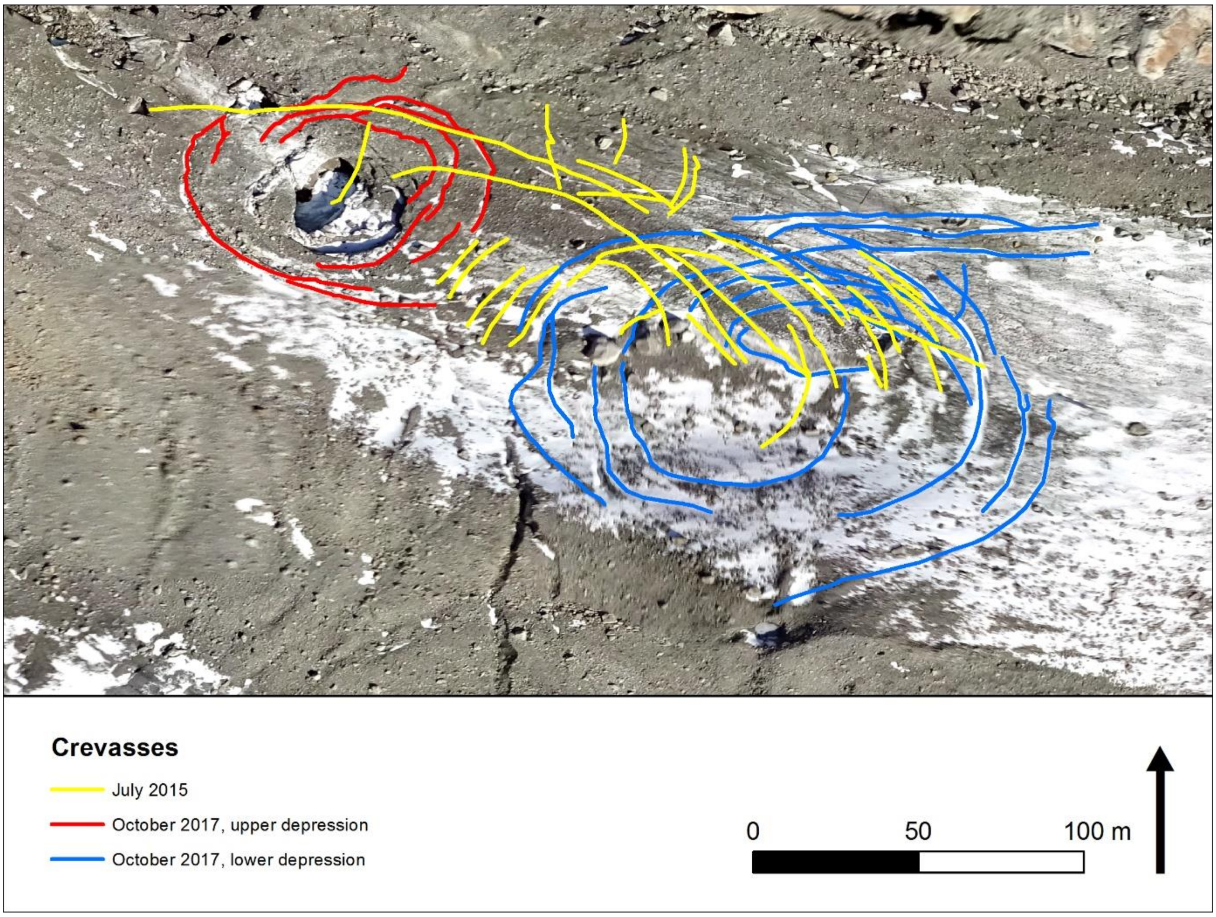

Fig. 77: Mapped crevasses surrounding the funnel-shaped depressions between July 2015 and October 2017. The crevasses observed in October 2017 have been divided into upper and lower depression.

The ice surface surrounding the subsidence generally experienced an average lowering of -9 ± 0.25 m per year. The difference images show that there are spots on the ice surface between the upper and lower depressions that experienced larger downwasting with up to -12 m between the summers of 2016 and 2017. This sudden increase in elevation loss could not be explained by the weather, as the summers of 2016 and 2017 were generally cooler than the year before. This suggests that the cavities became connected, leading to the destabilization of the ice surface and further decreasing its gradient. Moreover, the collapse of the upper depression created steep, debris-free ice surfaces, which act as small ice cliffs and further promote the ice melt.

6.3.5.3. Influence on glacier geometry

The accelerating subsidence and collapse of the ice surface as well as the increasing number of crevasses are signs of the rapid disintegration of the upper glacier tongue. The ice melt caused by englacial and subglacial melt water streams leads to a higher ice surface area within the glacier, which further accelerates melt and destabilization. The crevasses on the ice surfaces may be filled with melt water, which can increase their depths and may even allow them to penetrate to the glacier bed (Weertman 1973).

The comparison of the elevation changes in the upper and lower half of the glacier tongue shows that the former has experienced noticeably more downwasting in recent years than the latter, which can be attributed to the formation of the cavities. This unbalanced elevation change reduced the gradient of the upper tongue, as observed in the profile. As mentioned above, the surface slope of the ice as well as the ice thickness are factors affecting the velocity of the ice flow. As they decrease, so does the ice flow, eventually leading to the stagnation of the tongue. Without any ice flow, cracks and water channels in the ice will not be closed by internal deformation, allowing them to grow, which further accelerates the ice loss. The reduction of the ice flow and its driving stresses forms a positive feedback, in which the glacier tongue loses mass at an accelerating rate.

Funnel-shaped depressions have been observed on various glaciers in the Tyrolean Alps (Haberkorn 2011, Olefs and Fischer 2008, Stocker-Waldhuber et al. 2017). A link has been found between large, active and rapidly receding glaciers and the occurrence of surface ice depressions of this nature, but more research has to be conducted in the context of stagnant glaciers (Stocker-Waldhuber et al. 2017).

7. Conclusion

In this study, the formation and development of glacial features on a rapidly disintegrating glacier tongue in the Swiss Alps was presented and quantified. The large base of existing data, including the field reports, UAV images and ablation measurements, allowed a multi-temporal analysis of the tongue's evolution. Measurement conducted during an additional field visit as well as two more UAV flights further offered insights into the glacier's current state. A detailed study of the glacial features found on the Tiefenglacier's tongue led to the following answers of the previously defined research questions:

What kinds of glacial features can be found on the glacier tongue?

The focus was laid on five large features whose dynamics both depend on and affect the development of the glacier tongue: a lateral moraine, a medial moraine, a sediment hill, an ice cliff and two funnel-shaped depressions.

What are the underlying processes leading to the observed glacial features?

The combination of UAV imagery, on-site measurements and GIS-based calculations revealed a variety of processes leading to the formation of said features.

The moraines are the result of the insulating properties of supraglacial debris, while their disintegration is controlled by surface ablation, en- and subglacial streams as well as the occurrence of subglacial cavities.

The stagnation and rapid downwasting of the lower tongue revealed a sediment layer within the ice, which most likely originated from the upper tongue or the accumulation area. Its emerging angle was caused by the glacier ice's flowing motion before it became stagnant. The thick layer of supraglacial debris covering it prevented the underlying ice from melting, thus forming a sediment hill with an ice core.

The ice cliff was formed by supraglacial debris sliding off the ice surface, whose gradient was previously likely increased by enhanced melt from warm adjacent bedrock and debris. The combination of its direct exposure to the sun as well as the constant break-off of ice and the slide-off of debris led to very high backwasting rates and ensured that id did not flatten and disappear during the observation period.

The funnel-shaped depressions and the surrounding crevasses are the result of en- or subglacial air-filled cavities, which may have been formed by a lake whose water level lowered. As the cavities grow larger and the overlying ice surface thins down, it reaches a critical point where it can no longer support itself and collapses, as it happened to the upper depression.

In general, the supraglacial debris as well as the stagnation of the tongue play a central role in the formation of the discussed features, highlighting their influence on disintegrating glacier tongues.

In what way do the glacial features influence the development and geometric shape of the glacier tongue?

The duration and extent of the effects the features have on the overall glacier tongue vary greatly due to their individual dynamics.

Both moraines and the sediment hill delay the tongue's disintegration on a long-term scale by preserving the underlying ice from surface ablation. As the debris-free tongue experiences rapid downwasting, these debris-covered features grow taller relative to the surrounding ice surface due to their lower ablation rates. However, processes on a smaller scale, such as the subsidence of the lower medial moraine and its possible collapse in the near future, can again accelerate the tongue's disintegration.

The funnel-shaped depressions are direct signs of the upper tongue's destabilization due to its growingly hollowed out structure. The decreasing ice masses as well as the reduction of the surface gradient caused by the cavities are factors contributing to the tongue's stagnation.

The extremely high melt rates observed on the ice cliff caused the entire lower extension of the medial moraine to disappear within just three years. The fast horizontal movement of the cliff is expected to continue, but it will affect less ice mass due to its reduced surface area.

How do the glacial features develop in quantitative terms?

The lateral and medial moraines show larger elevation changes in their upper halves than in their lower halves. Between July 2015 and October 2017, the upper and lower lateral moraine showed an average downwasting of -15.2 m and -8.9 m, respectively. The medial moraine experienced a more evenly distributed elevation change, with -12.2 m and -10.1 m. The comparison with the downwasting rate on debris-free ice (-16 m, -9.9 m) shows how the debris-cover reduces surface ablation on the moraines. The fact that the debris-covered lower medial moraine shows elevation changes similar to the ones observed on debris-free ice, however, highlights the impact of other processes, such as englacial streams and cavities.

The sediment hill's formation is solely controlled by the downwasting of the surrounding ice surface. Between July 2014 and October 2017, this amounts to -13.5 – -14 m, or -4.2 – -4.3 m/a. By the end of the observation period the hill was approx. 5 m tall and 25 m long and is expected to increase in size as the tongue melts.

The highest backwasting rates observed on the ice cliff between July 2014 and October 2017 amount to -33.5 – -37 m, or -10.3 – -11.4 m/a. These rates are significantly higher than the ones found on the debris-free upper and lower tongue (8 m/a, 4.5 m/a) and thus underline the effect of surface aspect.

The rate at which the ice surface surrounding the two depressions sinks in stayed constant at an average of -9 ± 0.25 m/a between 2015 and 2017. Between July 2016 and October 2017, however, a few spots appeared visible in the difference images between the two depressions that showed downwasting rates of up to -12 m, suggesting that the cavities became connected. The hole that formed from the collapse of the ice surface was observed to be roughly 10 m deep and 31 m long.

The combination of UAV-derived imagery and in-situ measurements presents a very economical way to analyze a glacier tongue's development over the span of multiple years. Although the measurements are limited to the glacier surface, statements could be made to a certain degree about the tongue's internal structure.

This study helps to understand the development of rapidly retreating glacier tongues in a warming climate and exemplifies methods to expand research in this area. Glacial features and elevation changes on glacier tongues have already been covered well in glaciological research (Paul and Haeberli 2008, Reid and Brock 2014, Schomacker and Kjær 2008). What is new in this study, however, is the examination of all prominent features on a single glacier tongue and their impact on its disintegration as well as the quantification of their developments.

Further work in this research area could be interesting in the context of glacier reconstruction. In most parts of the world, glacial landforms could only be studied long after they have been formed, leaving their formation open to speculation. The accelerating retreat of glaciers nowadays, however, offers the opportunity to examine the formation of these landforms. A better understanding of the origin of glacial landforms allows to reconstruct past states of glaciers with increased certainty.

8. Outlook

This paper aids process understanding of intricate glacial structures as they appear on rapidly retreating glacier tongues. The quantification of those features reveals the complexity of the tongue's disintegration and emphasizes the irregularity of its retreat. It has been shown that a reasonable amount of information about the tongue's structure could be gained with economical measurements solely conducted on its surface. The results are partially subject to an unknown degree of uncertainty, however, due to the large number of students participating in the measurements with varying methods.

This study can be expanded by examining other disintegrating glacier tongues in more detail. Possible improvements include more uniform measurement techniques as well as the use of the same UAV model over multiple years. Further, the longer the observation period is, the more accurate statements can be made about the tongue's development. Glacial features could then be observed from the point of their formation until their disintegration, or even to the formation of glacial landforms. Additionally, glacio-speleological studies could be conducted to study the internal structures in more detail. Hydrological experiments with dye tracers would further allow to map en- and subglacial streams, which helps understanding the processes of glacial surface features, such as the funnel-shaped depressions found on the Tiefenglacier.

In conclusion, this study has shown simple methods to examine the disintegration and retreat of a glacier tongue in a warming environment and how glacial features affect each other. It serves as a base for further research in the area of glacier retreat and morphology.

9. References

Achermann, C., Böhler, K., Juvalta, M. and Kuenz, C. 2015. Effect of glacial debris cover on glacier melt rate: A case study at the Tiefenglacier, Switzerland. GEO 411 field report, Department of Geography Zurich, University of Zurich.

Agisoft user manual. Available at: http://www.agisoft.com/downloads/user-manuals/ (Last access: 14.06.2018).

ALPECOLe 2011. Flow and temperature. Available at: http://www.geo.uzh.ch/microsite/alpecole/static/course/lessons/04/04d.htm (Last access: 14.06.2018).

ArcGIS Pro. Tool reference: Resampling. Available at: http://pro.arcgis.com/en/pro-app/tool-reference/data-management/resample.htm (Last access: 14.06.2018).

Aus der Au, R., Graf, M., Schärer, C. and Wermelinger, S. 2016. Project Report. GEO 411 field report, Department of Geography Zurich, University of Zurich.

Barry, R.G. 2006. The status of research on glaciers and global glacier recession: a review. Progress in Physical Geography 30, 3, 285–306.

Benn, D.I. and Evans, D.J.A. 2010. Glaciers and Glaciation. Second Edition, London: Hodder Education.

Benn, D.I, Bolch, T., Hands, K., Gulley, J., Luckman, A., Nicholson, L.I., Quincey, D., Thompson, S., Toumi, R. and Wiseman, S. 2012. Response of debris-covered glaciers in the Mount Everest region to recent warming, and implications for outburst flood hazards. Earth-Science Reviews 114, 156–174.

Bhardwaj, A., Sam, L., Akanksha, Martín-Torres, F.J. and Kumar, R. 2016. UAVs as remote sensing platform in glaciology: Present applications and future prospects. Remote Sensing of Environment 175, 196–204.

Bolch, T., Pieczonka, T. and Benn, D.I. 2011. Multi-decadal mass loss of glaciers in the Everest area (Nepal Himalaya) derived from stereo imagery. The Cryosphere 5, 349–358.

Buri, P. and Pellicciotti, F. 2018. Aspect controls the survival of ice cliffs on debris-covered glaciers. Proceedings of the National Academy of Sciences 115, 17, 4369–4374.

Burkhalter, S., Denzinger, F. and Holzbecher, A. 2015. Morphology and processes related to the disintegration and downwasting of the tongue of Tiefengletscher. GEO 411 field report, Department of Geography Zurich, University of Zurich.

Büchler, L., Gassmann, C., Schmid, O., Steinert, T. and Sutter, L. 2017. Subglacial Overdeepenings: Is the Bikini a Must-have for visiting the Albert Heim Hut in the Future? GEO 411 field report, Department of Geography Zurich, University of Zurich.

Dąbski, M., Zmarz, A., Pabjanek, P., Korczak-Abshire, M., Karsznia, I. and Chwedorzewska, K.J. 2017. UAV-based detection and spatial analyses of periglacial landforms on Demay Point (King George Island, South Shetland Islands, Antarctica). Geomorphology 290, 29–38.

Davis, J.L. and Annan, A.P. 1989 Ground-penetrating radar for high-resolution mapping of soil and rock stratigraphy. Geophysical Prospection 37, 531-551.

Di Mauro, B., Fava, F., Ferrero, L., Garzonio, R., Baccolo, G., Delmonte, B. and Colombo, R. 2015. Mineral dust impact on snow radiative properties in the European Alps combining round, UAV, and satellite observations. Journal of Geophysical Research: Atmospheres 120, 6080–6097.

Engeler, M., Hanimann, D., Hug, B. and Hunziker, O. 2016. Effect of glacial debris cover on glacial tongue geometry and melt rates. GEO 411 field report, Department of Geography Zurich, University of Zurich.

Fountain, A. 2011. Temperate Glaciers. In: Singh, V.P., Singh, P. and Haritashya, U.K. (eds): Encyclopedia of Snow, Ice and Glaciers. Encyclopedia of Earth Sciences Series, Dordrecht: Springer.

Friello, C. and Hanson, G. 2015. Anatomy of a Crevasse Fill Ridge in Clara’s Woods, Stony Brook, New York. Department of Geosciences, Stony Brook University, SUNY, Stony Brook, NY.

Fugazza, D., Senese, A., Azzoni, R.S., Smiraglia, C., Cernuschi, M., Severi, D. and Diolaiuti, G.A. 2015. High-resolution mapping of glacier surface features. The UAV survey of the Forni glacier (Stelvio National Park, Italy). Geografia Fisica e Dinamica Quaternaria 38, 25–33.

Griffin, S. and Pippett, T. 2002. Ground penetrating radar. Papp, É. (ed): Geophysical and Remote Sensing Methods for Regolith Exploration 144, 80–89.

Haberkorn, A. 2011. Assessing the Contribution of Basal Melt Processes to the Local Mass Balance at the Tongue of Hintereisferner, Ötztal, Austria. Diploma Thesis, Faculty of Geo- and Atmospheric Sciences, University of Innsbruck.

Habib, A.F., Kim, E.-M. and Kim, C.-J. 2007. New Methodologies for True Orthophoto Generation. Photogrammetric Engineering & Remote Sensing 73, 1, 25–36.

Hafner, S., Huber, J., Ruppli, A. and Stäubli, A. 2014. Investigation of the actual and former glacier bed of the Tiefenglacier. GEO 411 field report, Department of Geography Zurich, University of Zurich.

Hasler, M., Kaelin, K., Mazenauer, C., Meyer, M. and Pfister, R. 2014. The effect of supraglacial debris on surface melt and terminus evolution. GEO 411 field report, Department of Geography Zurich, University of Zurich.

Höhle, J. and Höhle M. 2009. Accuracy assessment of digital elevation models by means of robust statistical methods. Journal of Photogrammetry and Remote Sensing 64, 398–406.

Jiskoot, H. 2011. Dynamics of Glaciers. In: Singh, V.P., Singh, P. and Haritashya U.K. (eds): Encyclopedia of Snow, Ice and Glaciers. Encyclopedia of Earth Sciences Series, Dordrecht: Springer.

Jóhannesson, T., Raymond, C. and Waddington, E. 1989. Time-scale for adjustment of glaciers to changes in mass balance. Journal of Glaciology 35, 355–369.

Kirkbride, M.P. 1993. The temporal significance of transitions from melting to calving termini at glaciers in the central Southern Alps of New Zealand. The Holocene 3, 3, 232–240.

Kirkbride, M.P. and Winkler, S. 2012. Correlation of Late Quaternary moraines: impact of climate variability, glacier response, and chronological resolution. Quaternary Science Reviews 46, 1–29.

Knight, P. 1999. Glaciers. Cheltenham: Stanley Thornes.

Li, Z., Zhu, Q. and Gold, C. 2005. Digital terrain modeling: principles and methodology. Boca Raton: CRC Press.

Magnússon, E., Rott, H., Björnsson, H. and Pálsson, F. 2007. The impact of jökulhlaups on basal sliding observed by SAR interferometry on Vatnajökull, Iceland. Journal of Glaciology 53, 181, 232–240.

MeteoSwiss. Federal Office of Meteorology and Climatology MeteoSwiss. Available at: http://www.meteoswiss.admin.ch (Last access: 14.06.2018).

Moll 2012. Tiefengletscher, Uri. Vergangenheits- und Gegenwartsanalyse, Eisradarmessungen zum Stand 2011 sowie Modellierungen einer zukünftigen möglichen Gletscherentwicklung. Master's thesis, Department of Geography Zurich, University of Zurich.

Mösch, S., Peneder, M., Ramp, A. and Walter, A. 2015. Project Report Field Seminar Tiefengletscher. GEO 411 field report, Department of Geography Zurich, University of Zurich.

Müller, J., Gärtner-Roer, I., Thee, P. and Ginzler, C. 2014. Accuracy assessment of airborne photogrammetrically derived high-resolution digital elevation models in a high mountain environment. Journal of Photogrammetry and Remote Sensing 98, 58–69.

Nakawo, M. and Rana, B. 1999. Estimate of ablation rate of glacier ice under a supraglacial debris layer. Geografiska Annaler 81 A, 4, 695–701.

Nath, P.C. and Vaughan, D.G. 2003. Subsurface crevasse formation in glaciers and ice sheets. Journal of Geophysical Research 108, B1, 1–12.

Neal, A. 2004. Ground-penetrating radar and its use in sedimentology: principles, problems and progress. Earth-Science Reviews 66, 261–330.

Nicholson, L. and Benn, D.I. 2013. Properties of natural supraglacial debris in relation to modelling sub-debris ice ablation. Earth Surface Processes and Landforms 38, 490–501.

Nishimura, D., Sugiyama, S., Bauder, A. and Funk, M. 2013. Changes in Ice-Flow Velocity and Surface Elevation from 1874 to 2006 in Rhonegletscher, Switzerland. Arctic, Antarctic, and Alpine Research 45, 4, 552–562.

Nuth, C. and Kääb, A. 2011. Co-registration and bias corrections of satellite elevation data sets for quantifying glacier thickness change. The Cryosphere 5, 271–290.

Oberli, S. 2017. SwissGlaciers. Available at: http://swissglaciers.org (Last access: 14.06.2018).

Oerlemans, J., Giesen, R.H. and Van den Broeke, M.R. 2009. Retreating alpine glaciers: increased melt rates due to accumulation of dust (Vadret da Morteratsch, Switzerland). Journal of Glaciology, 55, 192, 729–736.

Olefs, M. and Fischer, A. 2008. Comparative study of technical measures to reduce snow and ice ablation in Alpine glacier ski resorts. Col Regions Science and Technology 52, 371–384.

Østrem, G. 1959. Ice Melting under a Thin Layer of Moraine, and the Existence of Ice Cores in Moraine Ridges. Geografiska Annaler 41, 4, 228–230.

Paul, F., Kääb, A., Maisch, M., Kellenberger, T. and Haeberli, W. 2004. Rapid disintegration of Alpine glaciers observed with satellite data. Geophysical Research Letters 31.

Rastner, P. 2015. Co-registration tutorial. Department of Geography Zurich, University of Zurich.

Röthlisberger, H. 1972. Water Pressure in Intra- and Subglacial Channels. Journal of Glaciology 11, 62, 177–203.

Sakai, A., Nakawo, M. and Fujita, K. 2002. Distribution Characteristics and Energy Balance of Ice Cliffs on Debris-Covered Glaciers, Nepal Himalaya. Arctic, Antarctic, and Alpine Research 34, 1, 12–19.

Schweizerisches Gletschermessnetz. Available at: http://swiss-glaciers.glaciology.ethz.ch/ (Last access: 14.06.2018).

Schwendener, L. 2017. Wandernde Blöcke – Ein Vergleich von Gletschertischbewegungen in den Schweizer Alpen. Master's Thesis, Department of Geography Zurich, University of Zurich.

senseFly. eMotion software. Available at: https://www.sensefly.com/software/ (Last access: 14.06.2018).

Shahbazi, M., Sohn, G., Théau, J. and Menard, P. 2015. Development and Evaluation of a UAV-Photogrammetry System for Precise 3D Environmental Modeling. Sensors 15, 27493–27524.

Stocker-Waldhuber, M., Fischer, A., Keller, L., Morche, D. and Kuhn, M. 2017. Funnel-shaped surface depressions – Indicator or accelerant of rapid glacier disintegration? A case study in the Tyrolean Alps. Geomorphology 287, 58–72.

Stocker-Waldhuber, M., Fischer, A., Helfricht, K. and Kuhn, M. 2018. Ice flow velocity as a sensitive indicator of glacier state. The Cryosphere Discussions.

SwissImage. swissimage Produktinformation. Available at: https://www.swisstopo.admin.ch/de/home/products/images/ortho/swissimage.html (Last access: 14.06.2018).

swisstopo (a). Geoportal Schweizerische Eidgenossenschaft. Available at: http://map.geo.admin.ch (Last access: 14.06.2018).

swisstopo (b). AGNES. Available at: http://pnac.swisstopo.admin.ch/pages/en/agnes.html# (Last access: 14.06.2018).

Thompson, S., Benn, D.I., Mertes, J. and Luckman, A. 2016. Stagnation and mass loss on a Himalayan debris-covered glacier: processes, patterns and rates. Journal of Glaciology 62, 233, 467–485.

Tonkin, T.N., Midgley, N.G., Cook, S.J. and Graham, D.J. 2016. Ice-cored moraine degradation mapped and quantified using an unmanned aerial vehicle: A case study from a polythermal glacier in Svalbard. Geomorphology 258, 1–10.

van der Veen, C.J. 1999. Crevasses on glaciers. Polar Geography 23, 3, 213–245.

Vieli, A. 2016. GEO 411 Field course: High mountain processes. Department of Geography Zurich, University of Zurich.

Weertman, J. 1973. Can a water-filled crevasse reach the bottom surface of a glacier? International Association of Hydrological Sciences 95, 139–145.

Wentworth, C.K. 1922. A Scale of Grade and Class Terms for Clastic Sediments. The Journal of Geology 30, 5, 377–392.

WGMS World Glacier Monitoring Service. Available at: https://wgms.ch (Last access: 14.05.2018).

Zekollari, H., Huybrechts, P., Fürst, J.J., Rybak, O. and Eisen, O. 2013. Calibration of a higher-order 3-D ice-flow model of the Morteratsch glacier complex, Engadin, Switzerland. Annals of Glaciology 54, 63, 343–351.

Zemp, M., Hoelzle, M. and Haeberli, W. 2009. Six decades of glacier mass-balance observations: a review of the worldwide monitoring network. Annals of Glaciology 50, 50, 101–111.

10. Appendix

10.1. Ground control points

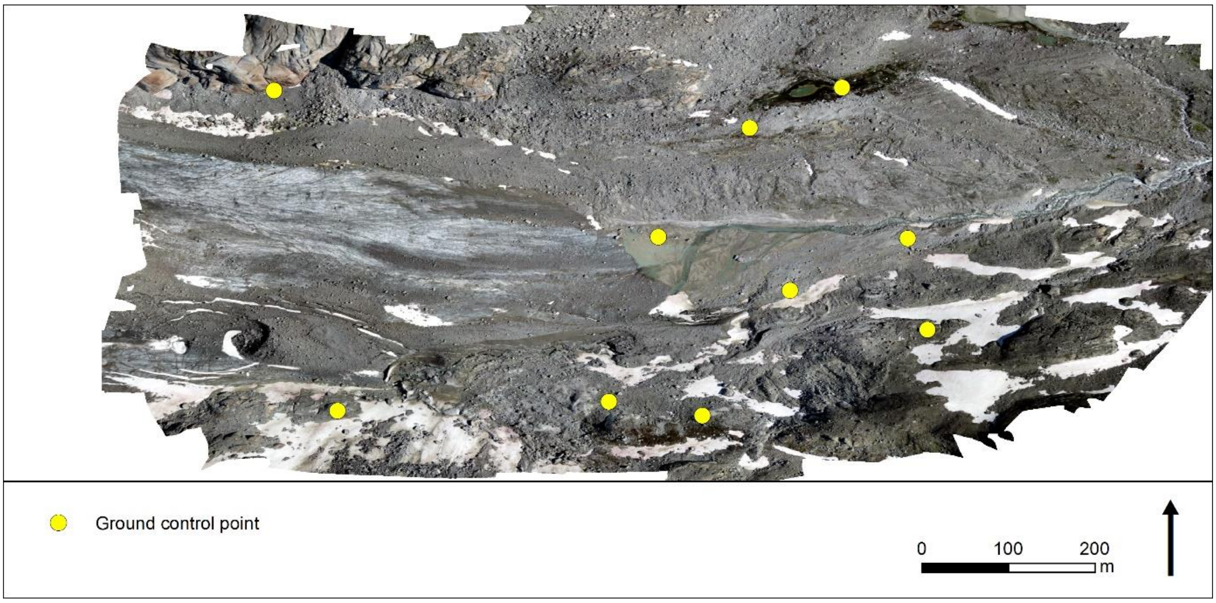

Fig. A 1: Locations of the GCPs for July 2014.

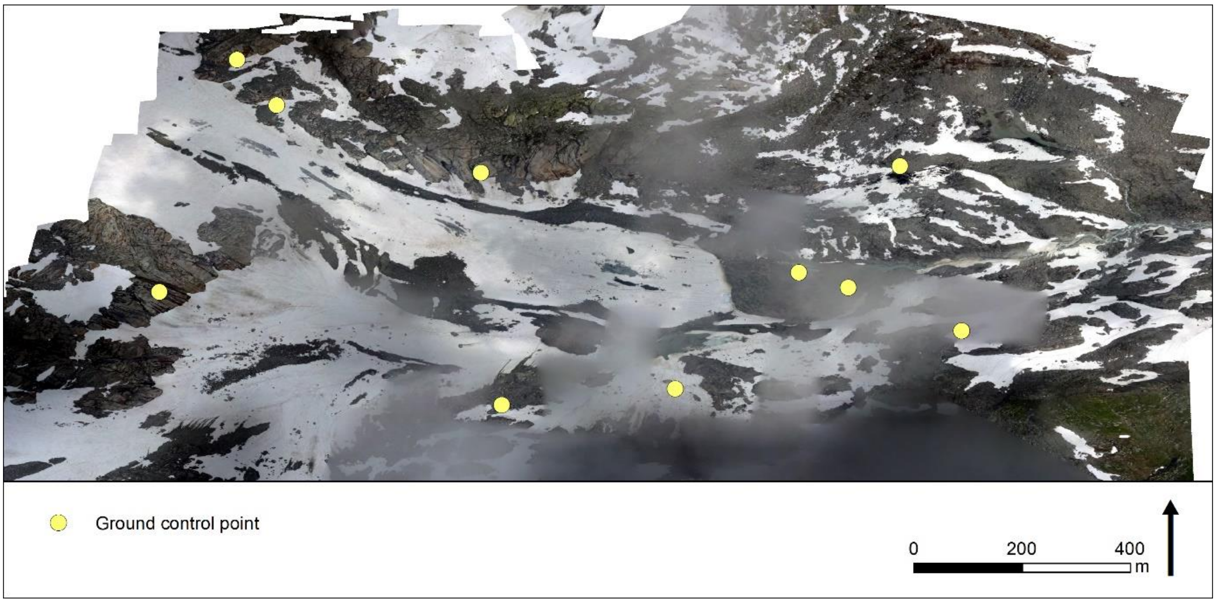

Fig. A 2: Locations of the GCPs for July 2016.

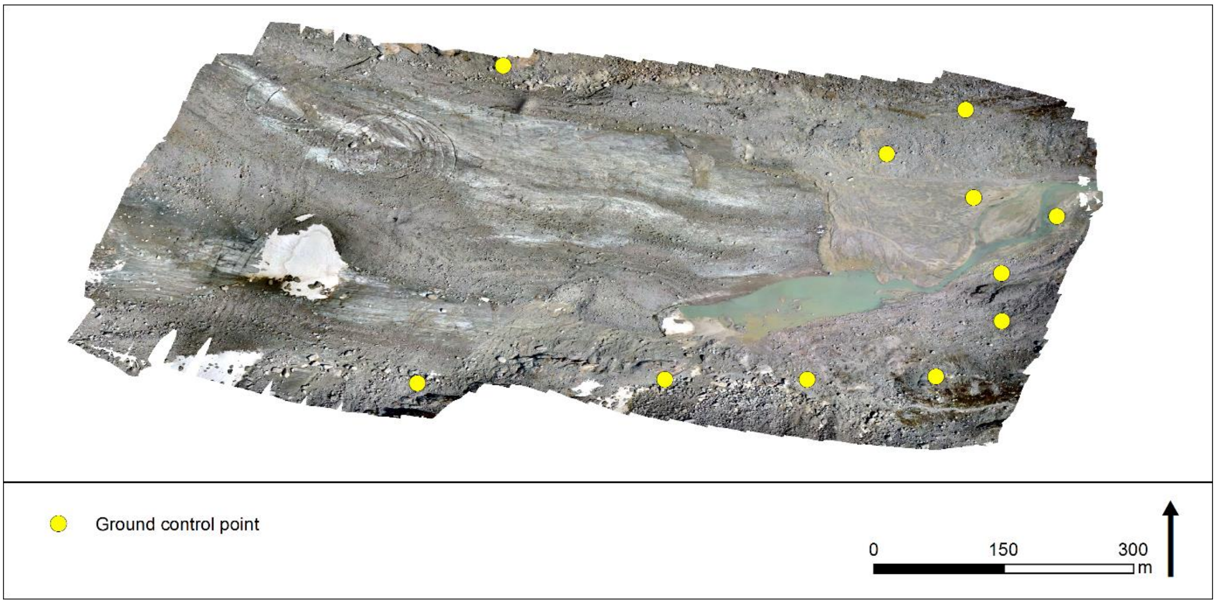

Fig. A 3: Locations of the GCPs for July 2017.

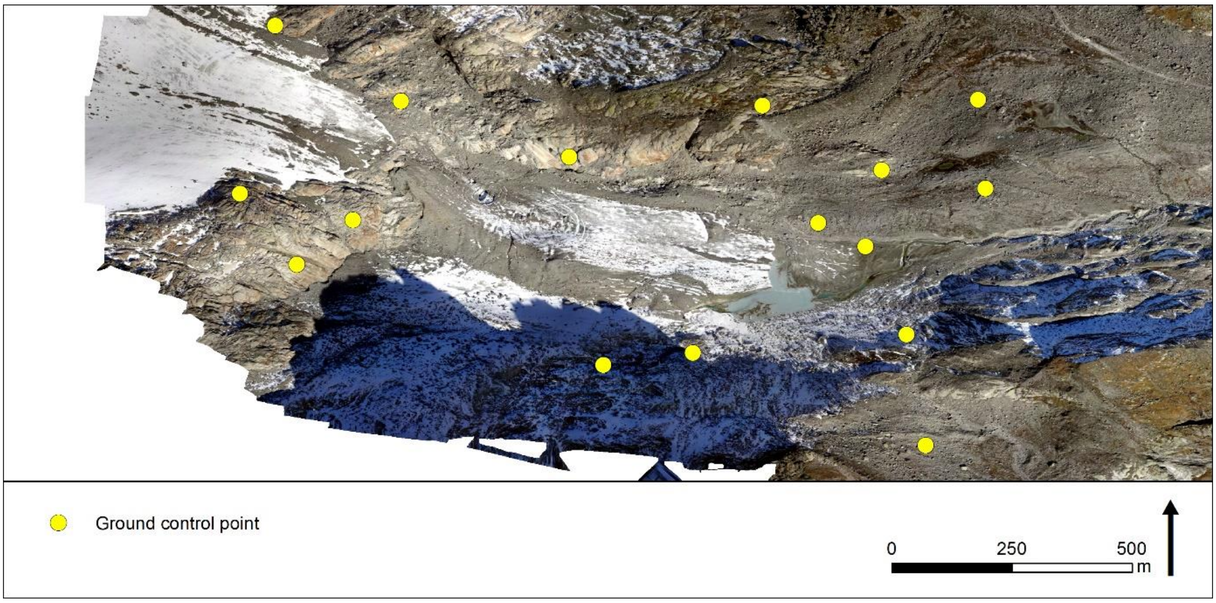

Fig. A 4: Locations of the GCPs for October 2017.

10.2. Digital surface models

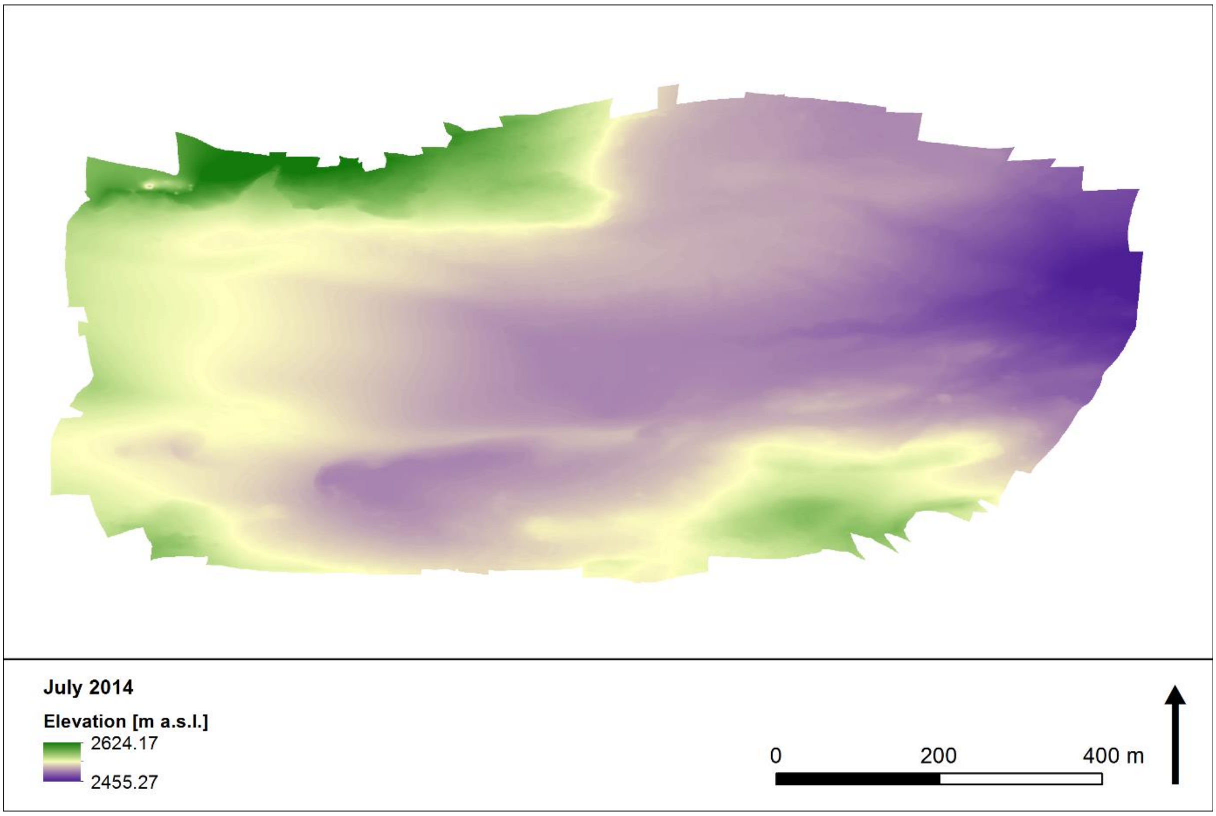

Fig. A 5: DSM for July 2014.

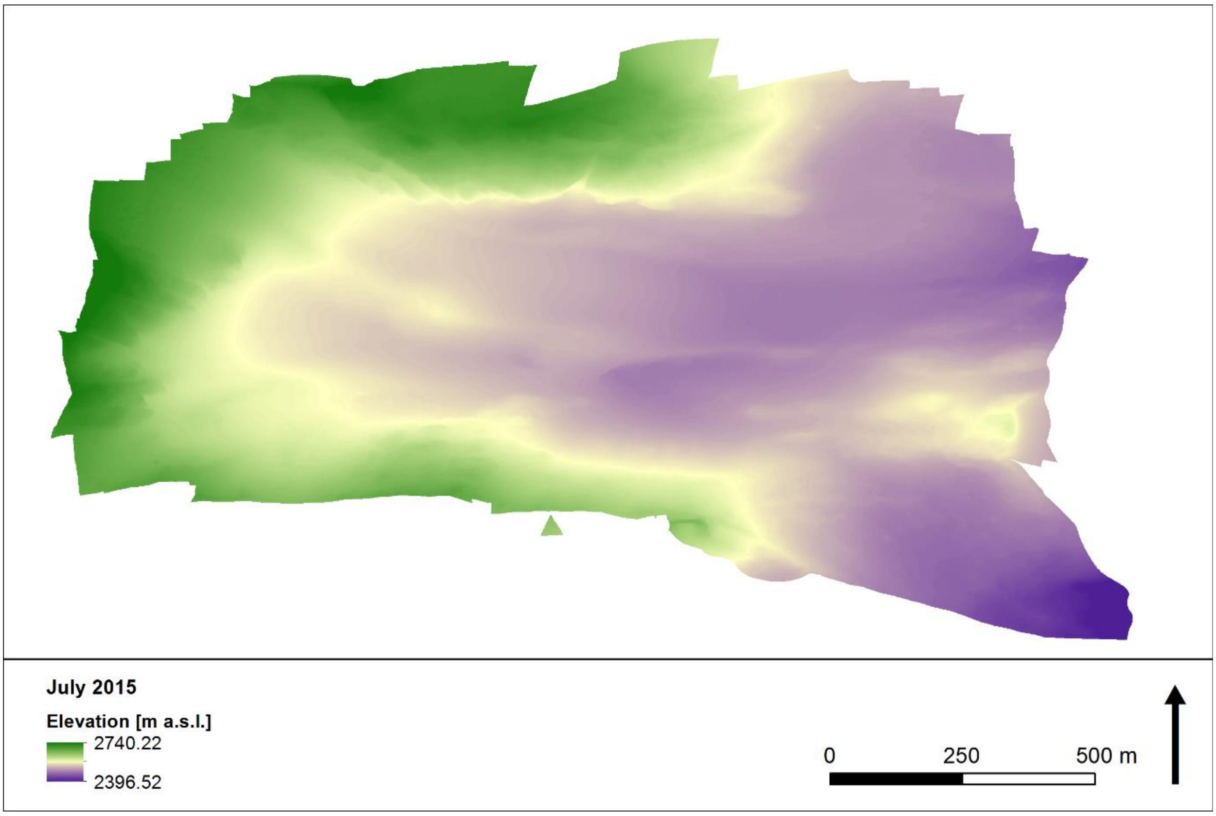

Fig. A 6: DSM for July 2015.

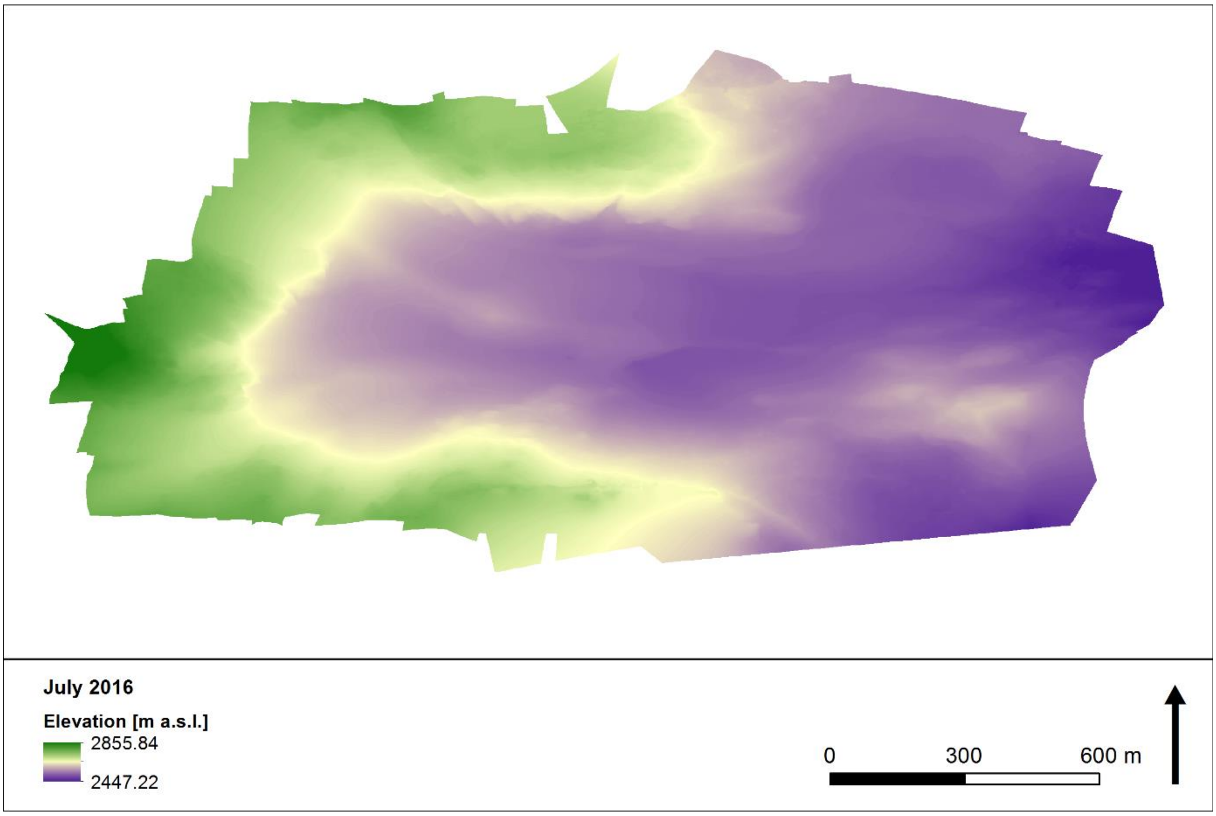

Fig. A 7: DSM for July 2016.

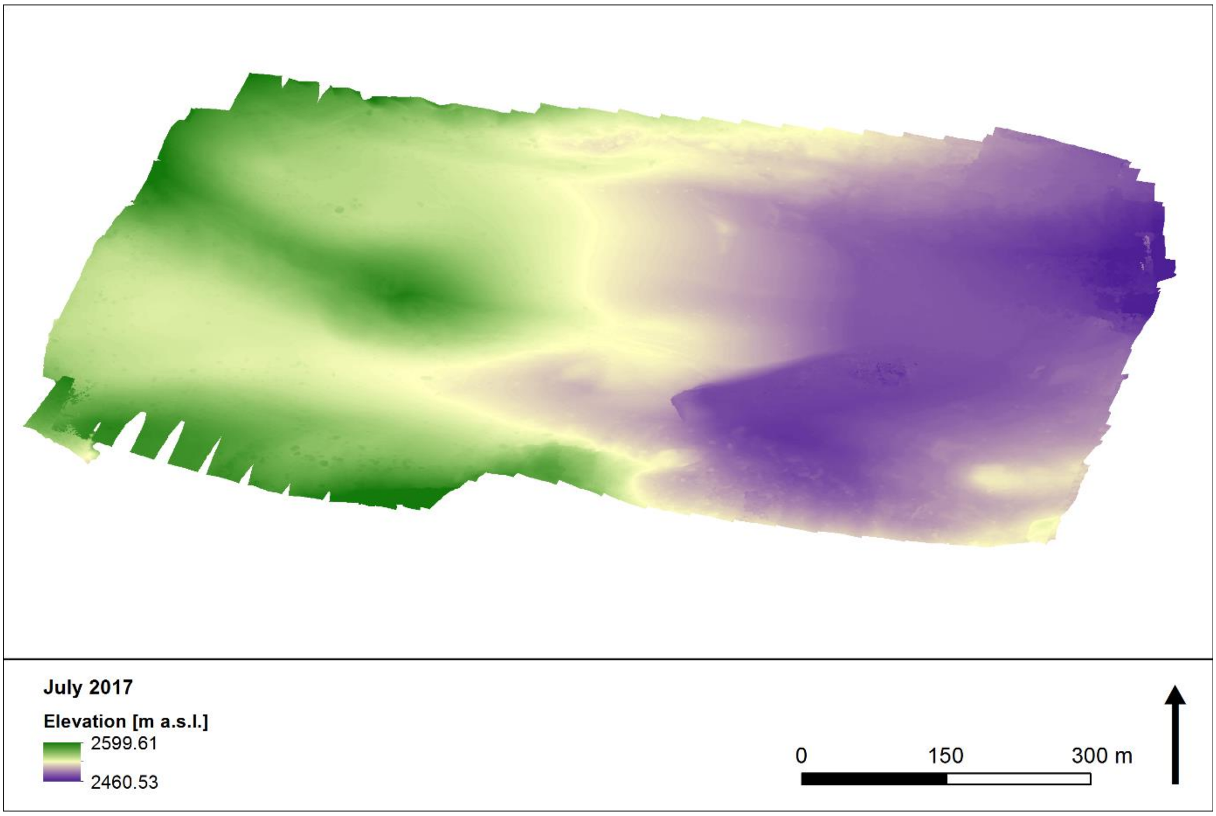

Fig. A 8: DSM for July 2017.

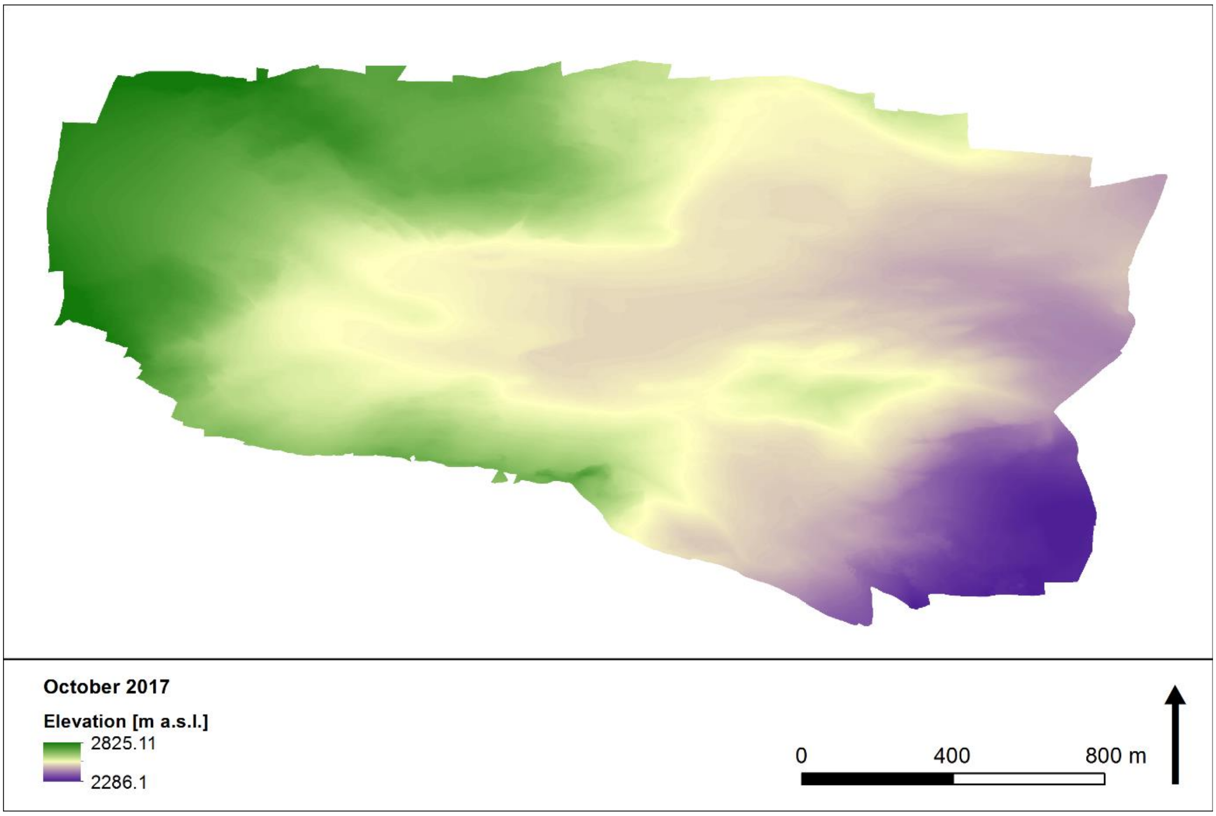

Fig. A 9: DSM for October 2017.

10.3. Orthophotos

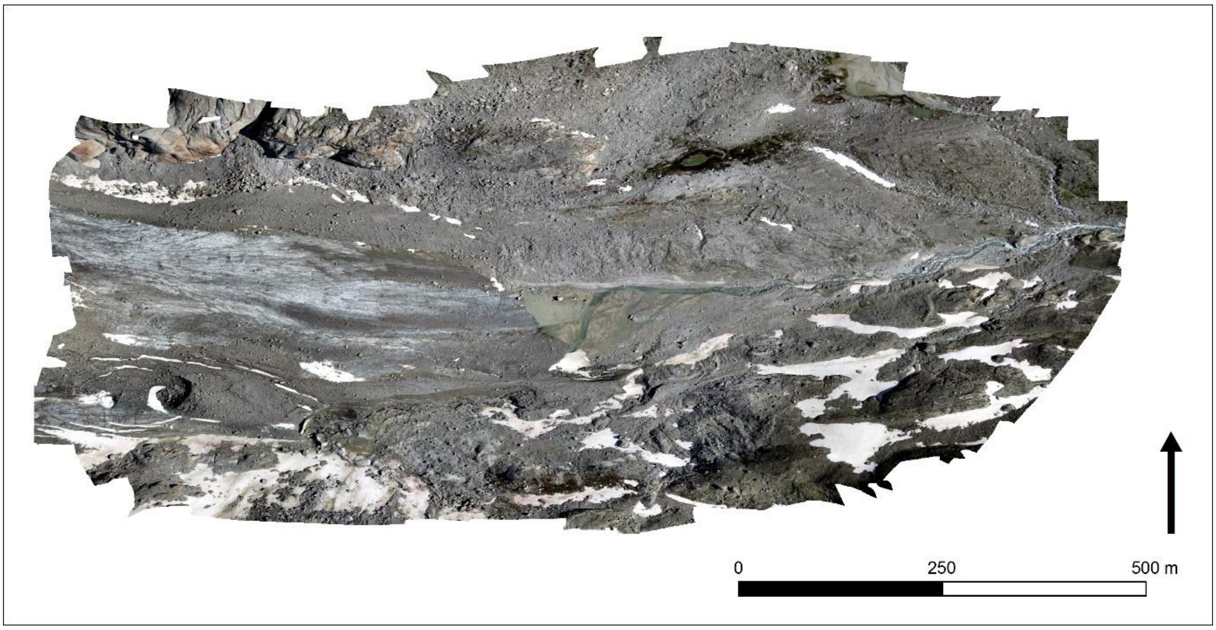

Fig. A 10: Orthophoto for July 2014.

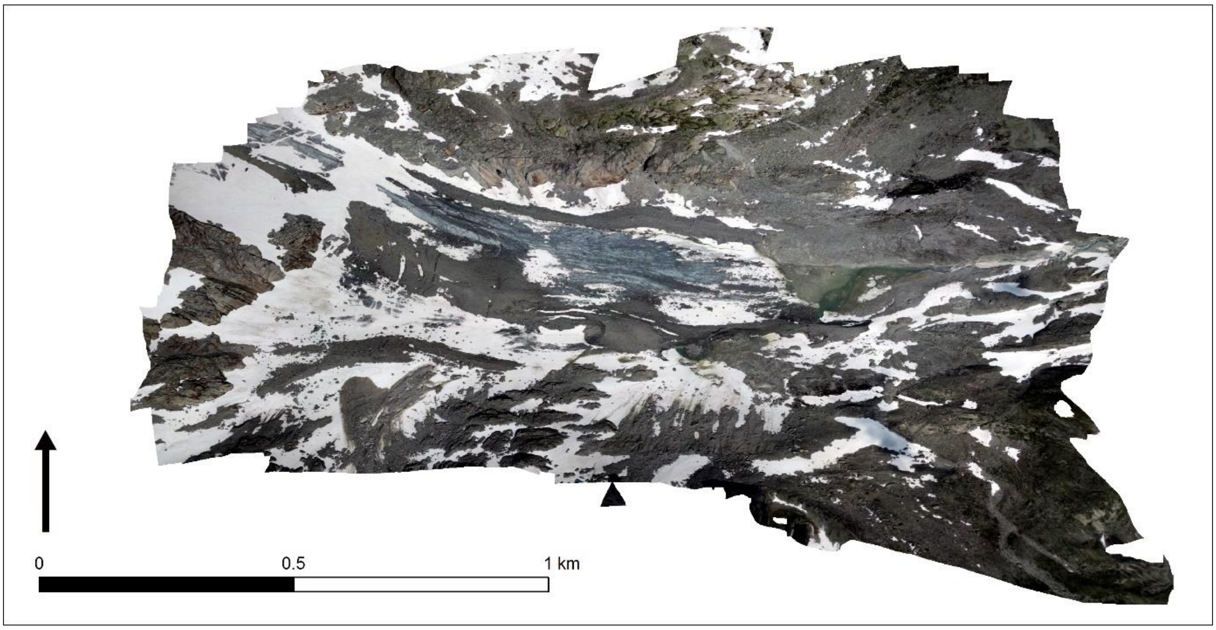

Fig. A 11: Orthophoto for July 2015.

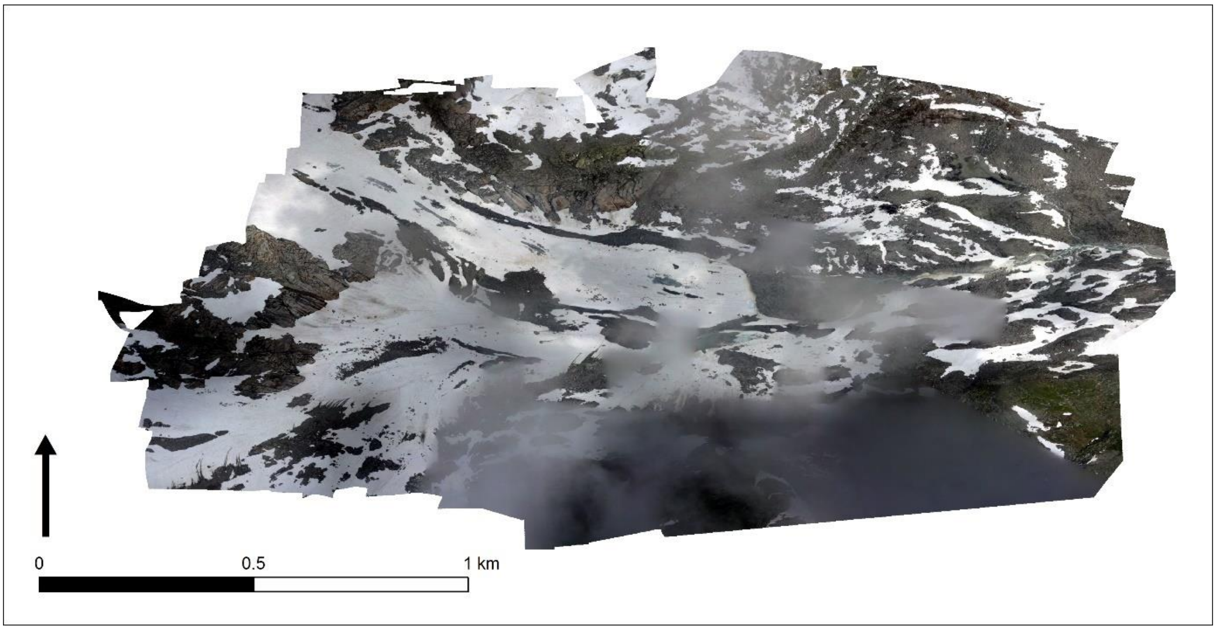

Fig. A 12: Orthophoto for July 2016.

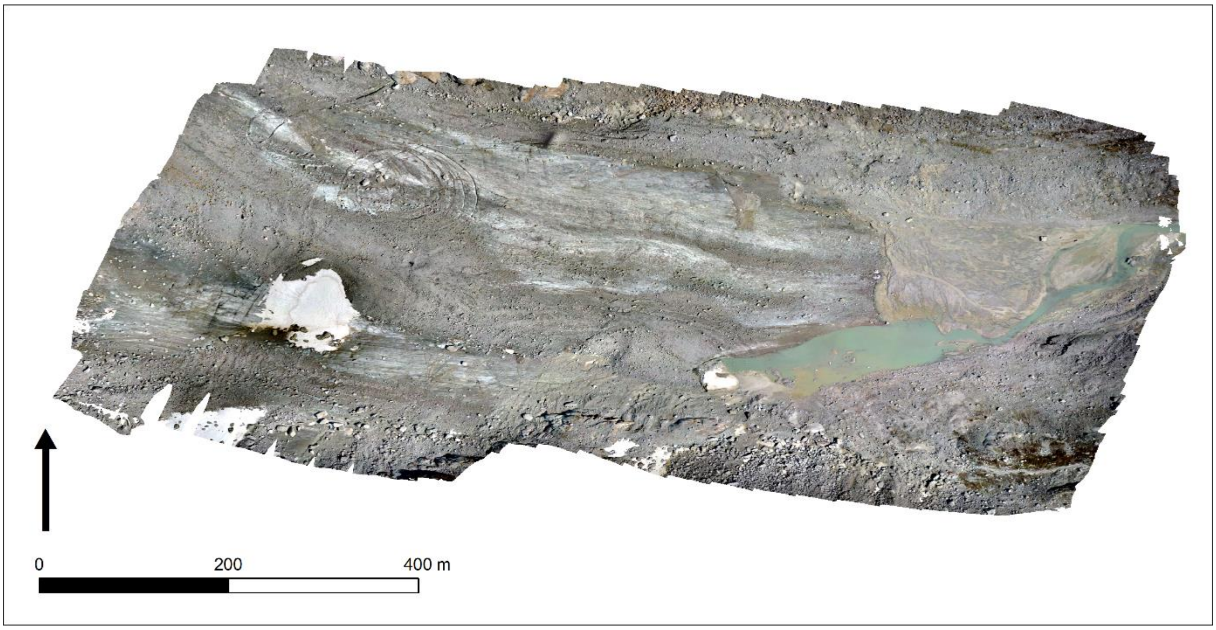

Fig. A 13: Orthophoto for July 2017.

10.4. Hillshades

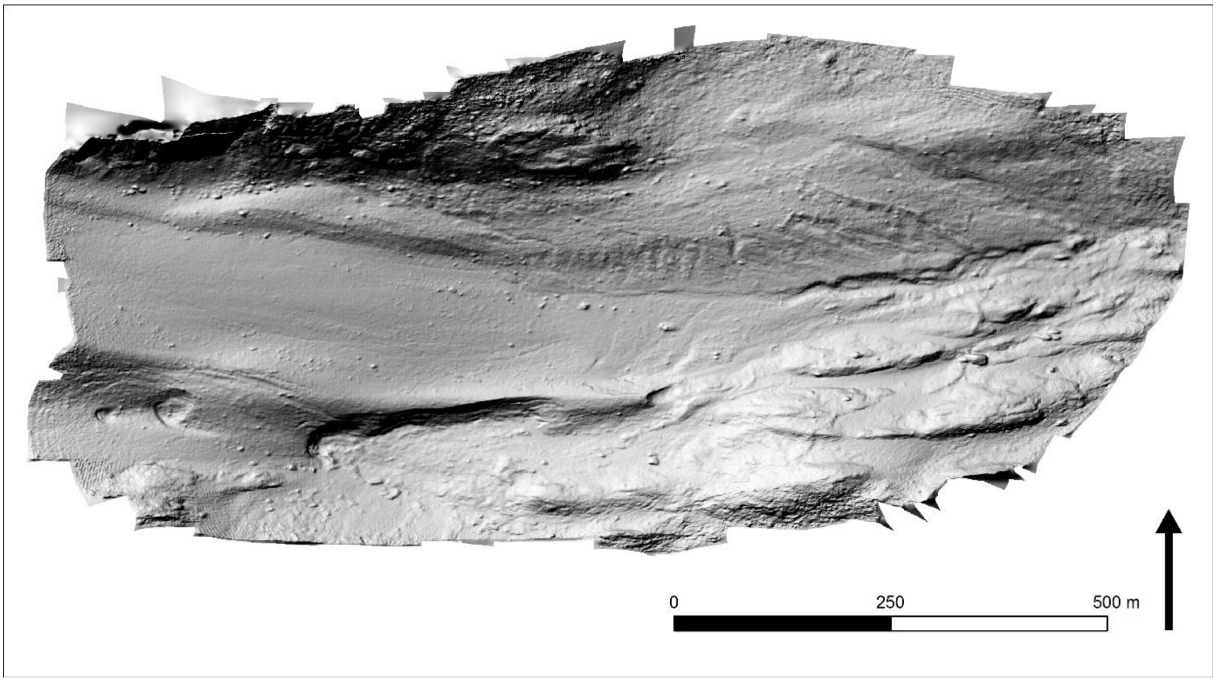

Fig. A 14: Hillshade for July 2014.

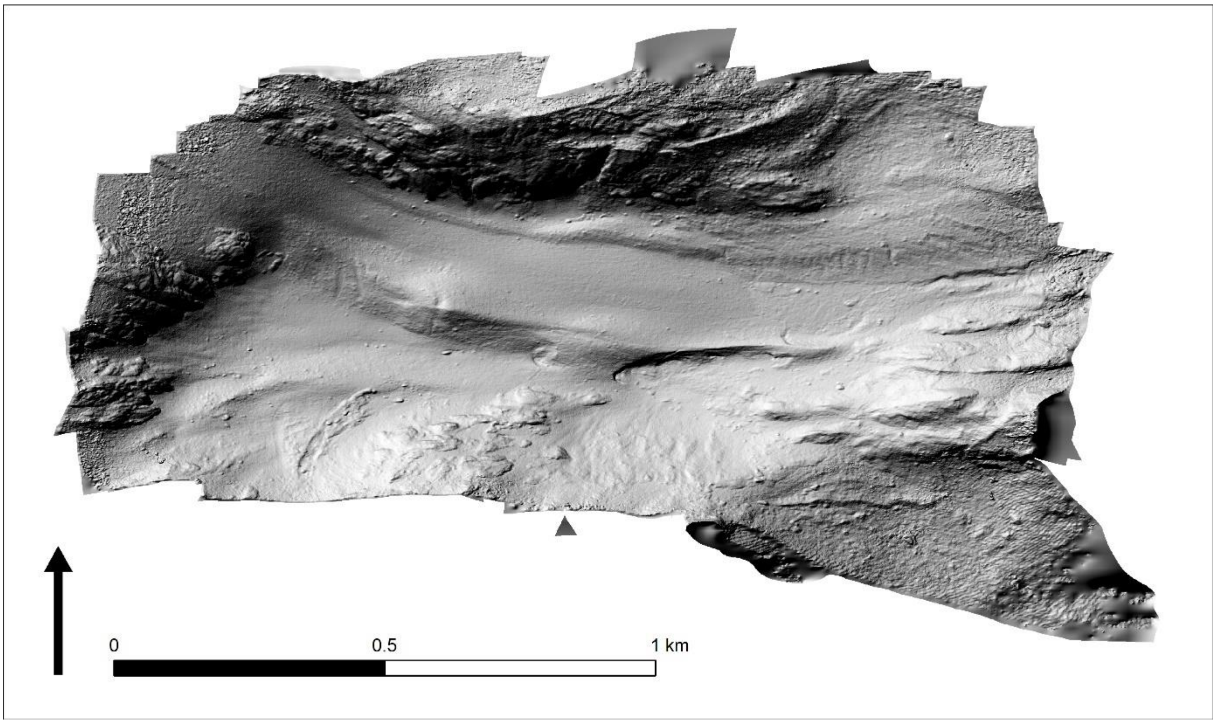

Fig. A 15: Hillshade for July 2015.

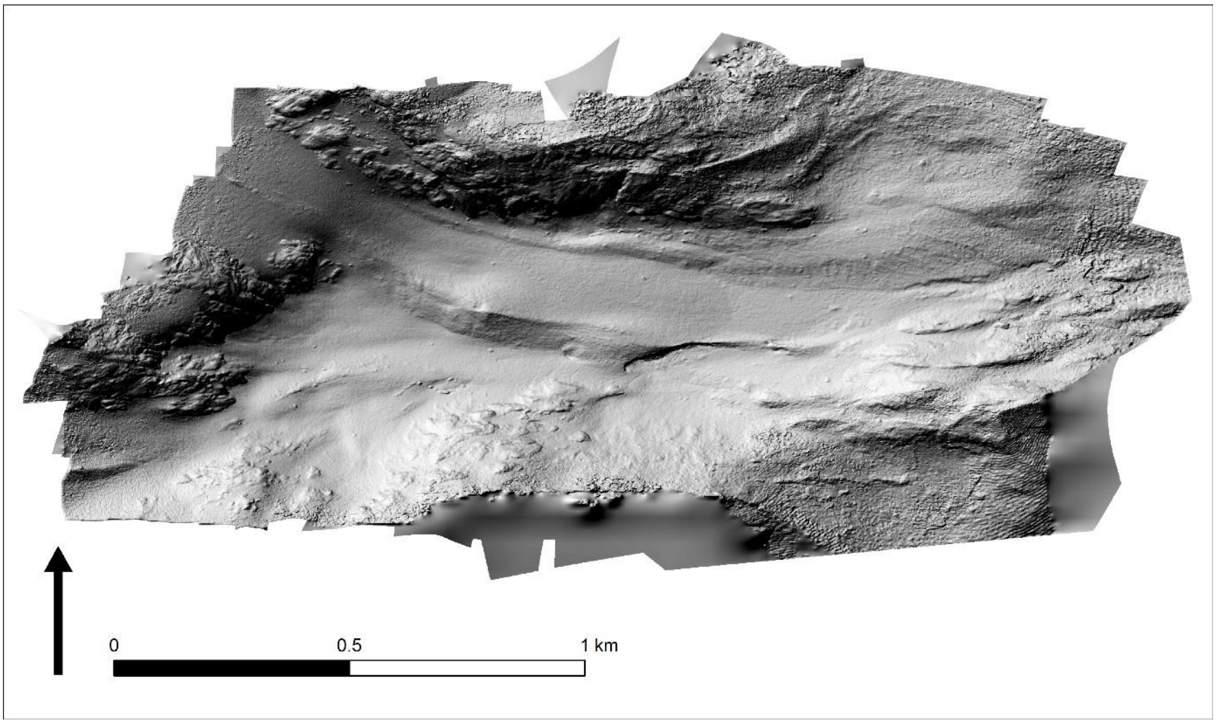

Fig. A 16: Hillshade for July 2016.

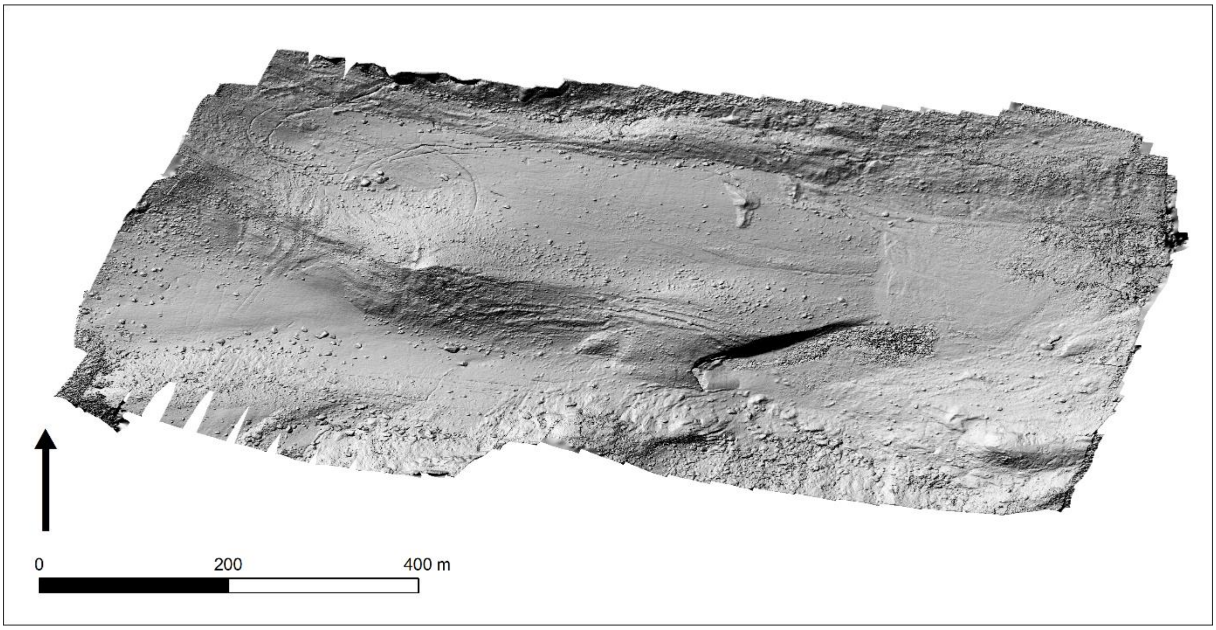

Fig. A 17: Hillshade for July 2017.

10.5. Difference images

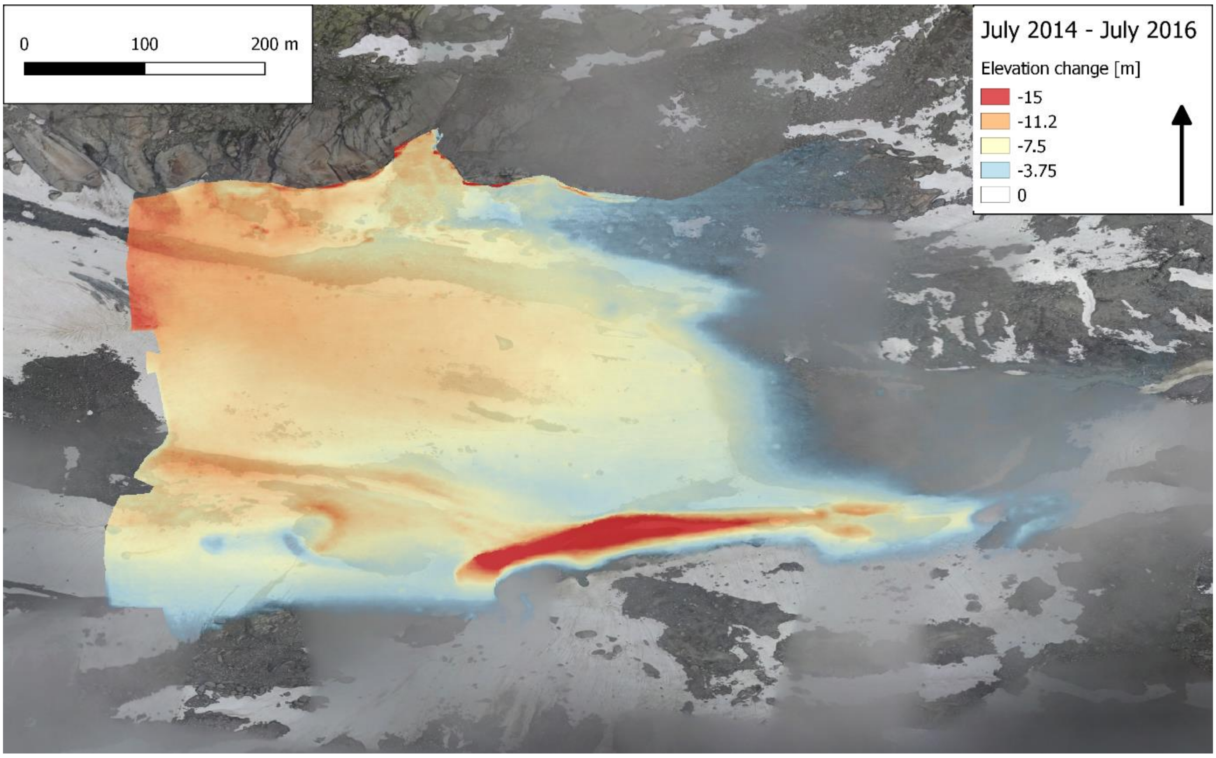

Fig. A 18: Elevation differences between July 2014 and July 2016.

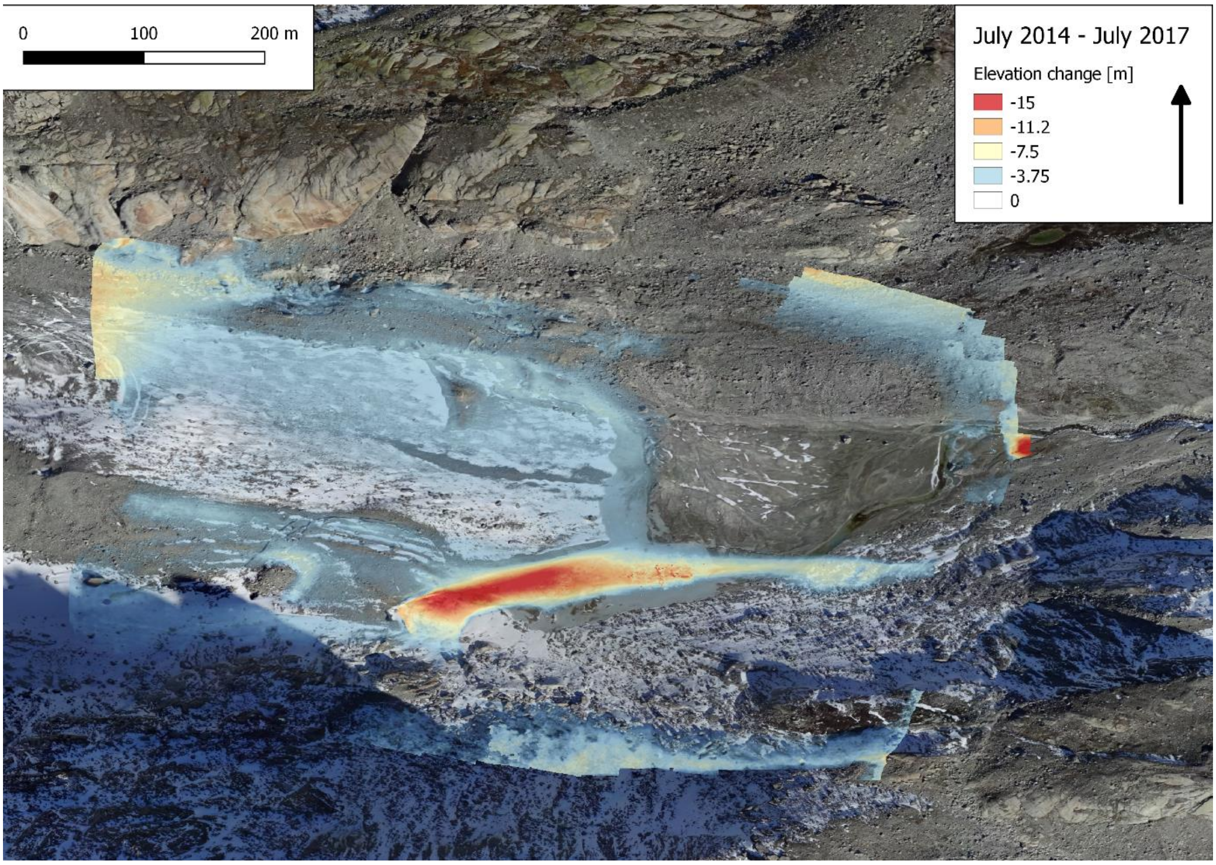

Fig. A 19: Elevation differences between July 2014 and July 2017. Note that these are unrealistic values because of the convex shape of the DSM of July 2017.

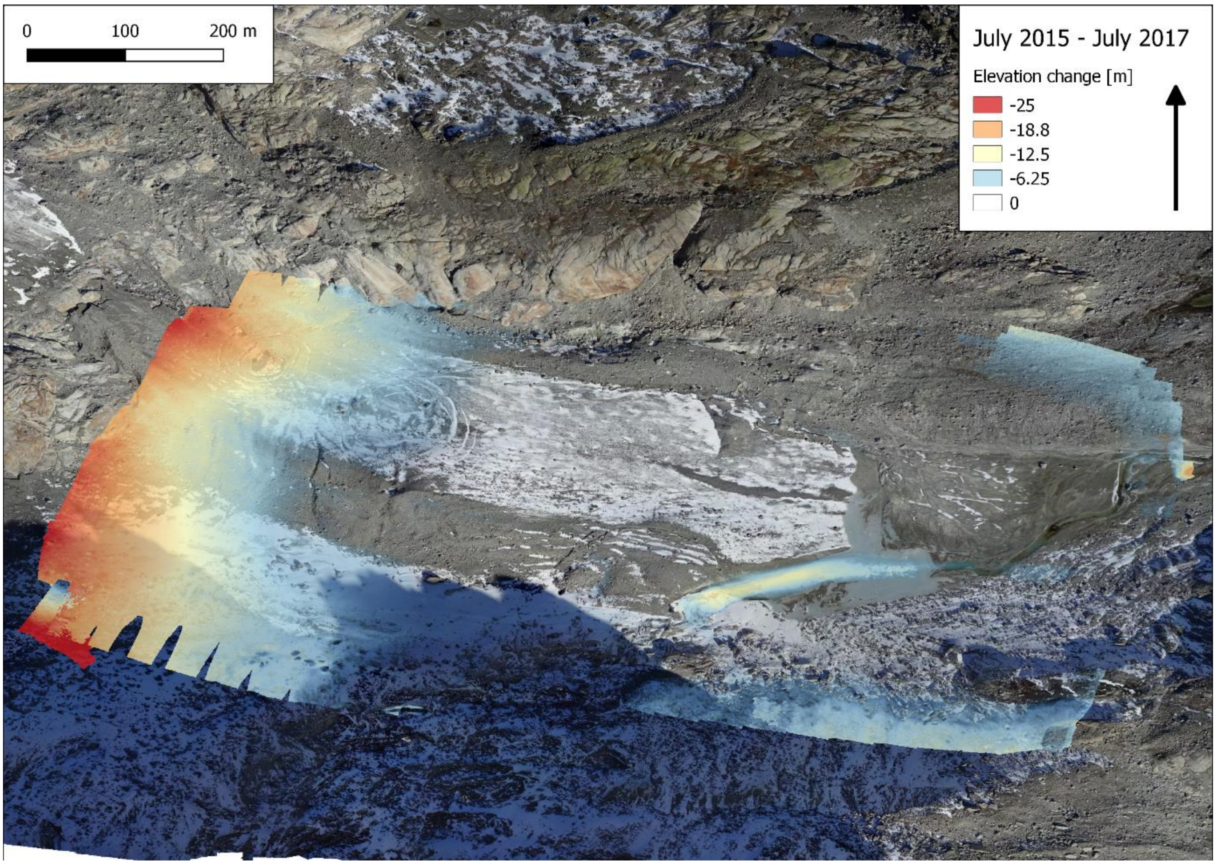

Fig. A 20: Elevation differences between July 2015 and July 2017. Note that these are unrealistic values because of the convex shape of the DSM of July 2017.

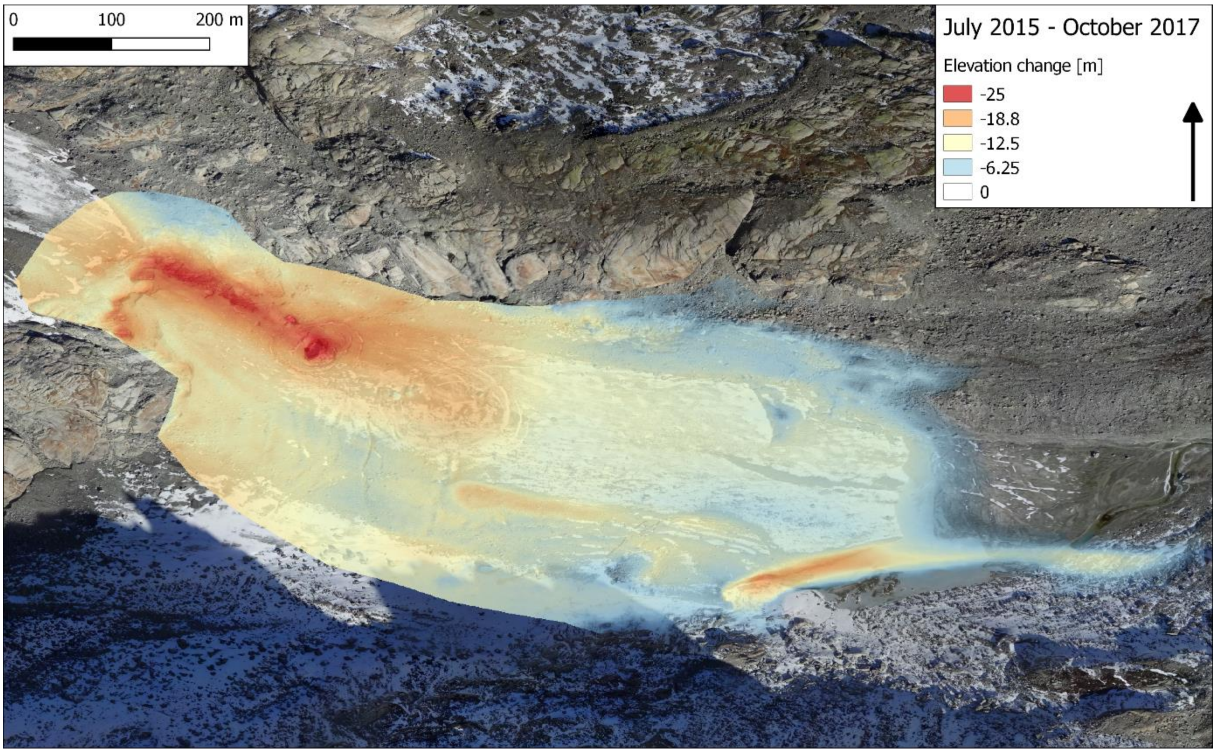

Fig. A 21: Elevation differences between July 2015 and October 2017.

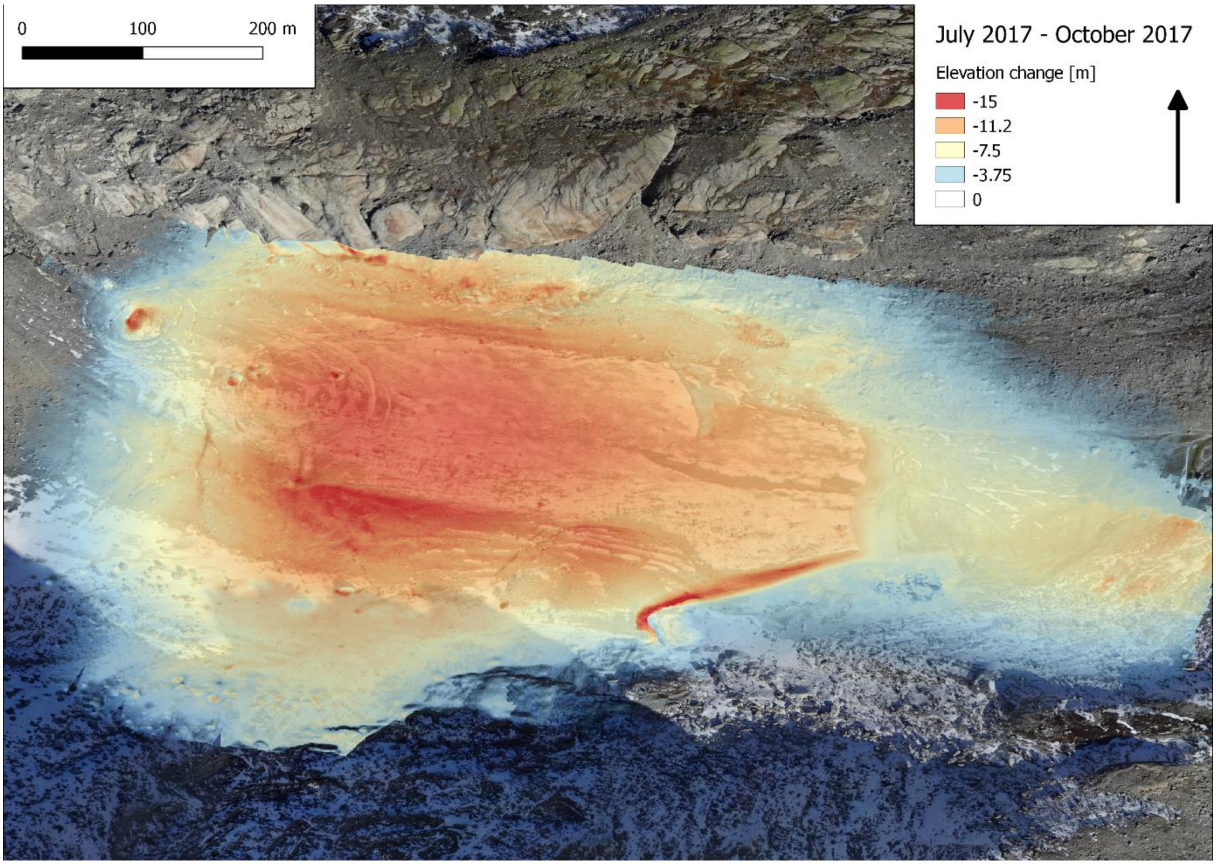

Fig. A 22: Elevation differences between July 2017 and October 2017. Note that these are unrealistic values because of the convex shape of the DSM of July 2017.

10.6. Ablation raw data

Table A 1: Measured ablation at Stakes 10, 11 and 12 between July 2014 and October 2017.

	Ablation [cm]		
Date	**Stake 10**	**Stake 11**	**Stake 12**
09.07.2014	0	0	0
14.07.2014	-6,1	-6,4	-7,7
15.07.2014	-10,7	-10,4	-12,6
16.07.2014	-18,2	-19,4	-21,6
17.07.2014	-19,9	-21,8	-24,9
17.07.2014	-25,3	-25,7	-28,1
19.10.2014	-386,5	-311,5	-320
14.07.2015	-458,2	-369	-413,5
15.07.2015	-471,2	-382,4	-430
16.07.2015	-475,7	-387	-436,1
11.10.2015	-813,1	-730,6	-771,3
11.07.2016	-847,8	-745,8	-776,1
04.11.2016			-1047,8
17.07.2017			-1252,8
20.07.2017			-1274,5

10.7. Debris thickness measurements

Table A 2: Debris thickness measurements including average debris thickness, descriptions of the measurement sites, and elevation changes extracted from the difference images by Achermann et al. 2015, Engeler et al. 2016 and Hasler et al. 2014. Missing descriptions and elevation change values are due to a lack of information about the measurement sites in the field reports.

			Elevation change [m]			
Measure-ment	**Av. Debris thickness [cm]**	**Description**	**Jul 14 – Jul 15**	**Jul 15 – Jul 16**	**Jul 16 – Oct 17**	**Jul 14 – Oct 17**
A1	7	-	-	-8.83	-6.95	-15.78
A2	7	-	-	-8.97	-7.81	-16.78
A3	8	-	-	-8.56	-6.29	-14.85
A4	8	-	-4.56	-8.10	-6.38	-19.04
A5	4	-	-4.49	-7.58	-6.23	-18.30
A6	4	-	-4.32	-6.97	-5.10	-16.39
A7	4.5	-	-4.28	-6.62	-4.33	-15.23
A8	7	-	-3.71	-6.10	-2.81	-12.62
A9	11	-	-2.75	-4.66	-4.62	-12.03
A10	11	-	-2.75	-4.81	-3.08	-10.64
A11	12	-	-3.15	-4.62	-2.76	-10.53
A12	6	-	-3.65	-4.23	-2.91	-10.79
A13	8	-	-3.1	-4.30	-3.57	-10.97
A14	12	-	-3.13	-3.81	-1.92	-8.86
A15	6	-	-2.62	-3.15	-1.19	-6.96
A16	13.5	-	-2.61	-3.13	-2.23	-7.97
A17	20	-	-1.91	-2.87	-0.48	-5.26
A18	15	-	-2.39	-3.64	-1.94	-7.97
A19	5.5	-	-1.9	-2.24	-2.08	-6.22
A20	6.5	-	-1.64	-1.80	-1.67	-5.11
A21	18	-	-1.25	-1.64	-1.66	-4.55
A22	0	-	-3.66	-7.13	-5.42	-16.21
A23	6	-	-3.58	-4.64	-2.33	-10.55
A24	0	-	-3.92	-5.29	-5.11	-14.32
A25	0.2	-	-3.64	-4.54	-4.54	-12.72
A26	13	-	-	-7.53	-3.54	-11.07
A27	8	-	-	-8.31	-4.68	-12.99
A28	13	-	-	-7.92	-3.55	-11.47
A29	3	-	-	-7.18	-5.56	-12.74
A30	16	-	-	-7.24	-7.74	-14.98
A31	6.5	-	-	-6.72	-3.85	-10.57
A32	0	-	-3.15	-5.89	-6.39	-15.43
A33	0	-	-2.39	-4.96	-5.27	-12.62
A34	6	-	-2.81	-5.95	-5.65	-14.41
A35	0	-	-1.52	-3.81	-2.63	-7.96
A36	4	-	-2.58	-5.51	-6.48	-14.57
A37	9	-	-2.85	-5.49	-3.15	-11.49
A38	4	-	-3.71	-5.41	-5.27	-14.39
A39	3.5	-	-2.42	-3.91	-4.42	-10.75
A40	1	-	-2.23	-4.17	-3.31	-9.71
A41	4	-	-2.93	-4.27	-4.41	-11.61
A42	5	-	-3.08	-4.14	-12.27	-19.49
A43	3	-	-2.48	-15.42	-0.97	-18.87
A44	6	-	-2.11	-11.65	-0.29	-14.05
A45	3	-	-2.49	-4.63	-3.16	-10.28
A46	6	-	-3.43	-3.93	-6.47	-13.83
A47	4	-	-3.65	-3.00	-5.54	-12.19
A48	56	-	-0.9	-0.83	-0.60	-2.33
A49	35	-	-0.84	-0.32	-0.52	-1.68

E1	8	Lower lateral moraine	-	-	-	-
E2	9	Lower lateral moraine	-	-	-	-
E3	0	Ice	-	-	-	-
E4	0	Ice	-	-	-	-
E5	0	Ice	-	-	-	-
E6	0	Ice	-	-	-	-
E7	5	Schist	-	-	-	-
E8	5	Schist	-	-	-	-
E9	3	Lower medial moraine	-	-	-	-
E10	3	Lower medial moraine	-	-	-	-
E11	4	Lower medial moraine	-	-	-	-
H1	0	Ice	-	-	-	-
H2	0.1	Ice	-	-	-	-
H3	1.5	Slightly covered ice	-	-	-	-
H4	3	Lower lateral moraine	-	-	-	-
H5	5	Lower lateral moraine	-	-	-	-
H6	15	Lower lateral moraine	-	-	-	-
H7	20	Lower medial moraine; Not a solid debris cover; pile of boulders which allow circulation of air	-	-	-	-

10.8. Calculated daily ablation rates

Table A 3: Measured surface ablation, duration of measurements and calculated average ablation per day. Only measurement sites with sufficient information about the ablation and the duration of the measurements were taken into account.

Measurement	**Surface ablation [cm]**	**Duration of measurement [h]**	**Av. ablation per day [cm/d]**
A7	-7	60	-2,8
A13	-5,1	60	-2,0
A22	-9,5	60	-3,8
A23	-3,5	60	-1,4
A24	-8,6	60	-3,4
A25	-10,1	60	-4,0
A30	-3,9	60	-1,6
A31	-5,2	60	-2,1
A39	-6,3	60	-2,5
A40	-9,5	60	-3,8
E1	-8	55,3	-3,5
E2	-5	55,3	-2,2
E3	-9	55,3	-3,9
E4	-9,2	55,3	-4,0
E5	-9,7	55,3	-4,2
E6	-11,3	55,3	-4,9
E7	-11	55,3	-4,8
E8	-11,2	55,3	-4,9
E9	-8,3	55,3	-3,6
E10	-10,4	55,3	-4,5
E11	-10,5	55,3	-4,6
H1	-16	55	-7,0
H2	-21	55	-9,2
H3	-13,5	55	-5,9
H4	-12,5	55	-5,5
H5	-8,5	55	-3,7
H6	-4	55	-1,7

Personal declaration

I hereby declare that the submitted thesis is the result of my own, independent work. All external sources are explicitly acknowledged in the thesis.

Oliver Hunziker

Zürich, 29.06.2018